365

# Three- and four-dimensional variational assimilation with a general circulation model of the tropical Pacific Ocean

A. T. Weaver[1], J. Vialard[2,3], D. L. T. Anderson[2] and P. Delecluse[3]

## Research Department

[1] *Centre Européen de Recherche et de Formation Avancée en Calcul Scientifique (CERFACS/CNRS, URA 1875 - SUC), Toulouse, France.*
[2] *European Centre for Medium-range Weather Forecasts, Reading, U. K.*
[3] *Laboratoire d'Océanographie Dynamique et de Climatologie (UMR CNRS/IRD/UPMC), Paris, France.*

*March 2002*

European Centre for Medium-Range Weather Forecasts
Europäisches Zentrum für mittelfristige Wettervorhersage
Centre européen pour les prévisions météorologiques à moyen terme

**Abstract**

Three- and four-dimensional variational assimilation (3D- and 4D-Var) systems have been developed for the OPA ocean general circulation model (OGCM) of the Laboratoire d'Océanographie Dynamique et de Climatologie. An iterative incremental approach is used to minimize a cost function that measures the statistically-weighted squared differences between the observational information and their model equivalent. The control variable of the minimization problem is an increment to the background estimate of the model initial conditions available at the beginning of each assimilation window. In 3D-Var, the increment is transported between observation times within the window using a persistence model, while in 4D-Var a dynamical model derived from the tangent-linear (TL) of the OGCM is used. Both the persistence and TL models are shown to provide reasonably good descriptions of the evolution of typical errors over the 10- and 30-day widths of the assimilation windows used in our 3D- and 4D-Var experiments, respectively. Intermittent updating of the linearization state of the TL model is shown to be an important feature of the 4D-Var minimization algorithm.

The present system relies on a univariate formulation of the background-error covariance matrix. In practice, the background-error covariances are specified implicitly within a change of control variable designed to improve the conditioning of the minimization problem. Horizontal and vertical correlation functions are modelled using a filter based on a numerical integration of a diffusion equation. The filter is computationally efficient, and flexible to capture key statistically-observed features, such as longer zonal than meridional length scales in the temperature field in the tropics. The background-error variances are geographically dependent and specified from the model climatology. Single observation experiments are presented to illustrate how the TL dynamics act to modify these variances in a flow-dependent way by diminishing their values in the mixed layer and by displacing the maximum value of the variance to the level of the background thermocline.

The 3D- and 4D-Var systems have been applied to the tropical Pacific and cycled over the period 1993-98 using *in situ* temperature observations from the Global Temperature and Salinity Pilot Programme. The overall effect of the data assimilation is to reduce a large bias in the thermal field which was present in the control. The fit to the data in 4D-Var is better than in 3D-Var, and within the specified observation-error variance. The fit is also very good at time-scales of the same order or shorter than the assimilation window (e.g., at the time-scale of tropical instability waves), which demonstrates the effectiveness of 4D-Var in carrying information through time using the linearized ocean dynamics. Both the mean state and the inter-annual variability of the thermal field are improved by the assimilation. For other fields, the improvement is less evident. Some fields are even degraded (for example the surface currents in 3D-Var). These deficiences suggest that other constraints are needed to control the analysis of the nonassimilated variables. Improvements in the analysis can be expected in the future with the inclusion of a multivariate background-error covariance matrix.

# 1  Introduction

The *El-Niño* Southern Oscillation (ENSO) phenomenon is one of the main contributors to predictability on seasonal to interannual time-scales (Barnett *et al.* 1993; Palmer and Anderson 1994). Accurate ENSO forecasts are thus a prerequisite to the development of a reliable dynamical seasonal forecasting system with a coupled ocean-atmosphere model (CGCM). Early studies (Cane *et al.* 1986; Latif and Flügel 1991; Balmaseda *et al.* 1994) showed that some ENSO forecasting skill could be obtained using only observed surface wind-stress to initialize the ocean component of the forecasting system. More recent studies have shown that assimilating ocean observations to initialize CGCMs resulted in significantly better ENSO forecasts (Ji and Leetma 1997; Rosati *et al.* 1997; Alves *et al.* 1998; Segschneider *et al.* 2000a; 2002). Subsurface temperature observations from Expendable BathyThermographs (XBTs) and the Tropical Atmosphere-Ocean (TAO) array (McPhaden 1993) were shown to be especially beneficial to forecast skill (Ji and Leetma 1997; Alves *et al.* 1998; Segschneider *et al.* 2002). Combining available observations and an ocean model into a dynamically consistent picture of the ocean state can also help to provide better insight into the processes determining ocean variability at various time scales.

The ocean data assimilation system currently used for operational seasonal forecasting at the European Centre for Medium-Range Weather Forecasts (ECMWF) is based on a statistical univariate scheme that uses temperature information only (Alves *et al.* 1998; Segschneider *et al.* 2002). Analyses are produced sequentially by combining observations distributed over a pre-specified time window, with a background temperature estimate from the model. Statistical (covariance) information about the background and observation errors is used to determine the structure and amplitude of the temperature corrections to be applied to the background state. The analysis problem is solved using optimal interpolation (OI) (Smith *et al.* 1991). In order to avoid exciting unrealistic gravity waves, the temperature corrections generated by the OI are merged slowly into the model until the next analysis time ten days later.

The ECMWF OI system has a number of limitations. First, as time-distributed observations are assimilated simultaneously, the analysis is unable to capture any variability in the observations occurring at time-scales less than the window width. This could occur, for example, for a first baroclinic mode equatorial Kelvin wave which can travel nearly 2500 kilometres in the 10-day window width currently used in the ECMWF operational system. Second, the system has been adapted from an existing two-dimensional analysis scheme (Smith *et al.* 1991) in which an analysis is performed separately at each model level. This requires that observations first be interpolated to model levels, a procedure that can ultimately degrade the information content of the observations particularly when their vertical distribution is sparse. Third, the scheme is univariate so that corrections are made only to the temperature field. Recent studies have shown that introducing dynamically unbalanced increments into the model can lead to serious model biases (Bell *et al.* 2001; Burgers *et al.* 2002). Correcting temperature while leaving salinity unchanged can upset the static stability of the water column and lead to spurious convection (Segschneider *et al.* 2000b; Troccoli *et al.* 2002). This particular problem has been largely solved in the ECMWF system by imposing a local temperature-salinity (T-S) conservation on the analysed temperature field (Troccoli *et al.* 2002). Ideally, however, such a constraint should, if possible, be integrated into the analysis step itself to allow for a more consistent use of all available observational information. Some success has been achieved in assimilating altimeter data with the OI system (Segschneider *et al.* 2000a; 2002) using a procedure that relies on converting the altimeter data into pseudo-temperature observations prior to the analysis step (Cooper and Haines 1996). This leads to the delicate problem, however, of how to weight the pseudo-temperature observations in the OI, in particular relative to assimilated *in situ* temperature observations. Some of these problems are not fundamental deficiencies of OI and could in principle be corrected. However, the development of the ECMWF OI is limited and so we explore here the possibility of developing more advanced data assimilation methods.

In meteorology, OI was the standard technique used for many years for producing initial conditions for Numerical Weather Prediction (NWP) (Lorenc 1981). More recently, however, most of the major NWP centres have

replaced their OI systems by variational assimilation systems (Parrish and Derber 1992; Courtier *et al.* 1998; Gauthier *et al.* 1999; Rabier *et al.* 2000; Lorenc *et al.* 2000). In variational assimilation, the analysis problem is defined by the minimization of a cost function that measures the statistically-weighted squared differences between observations (including a model background state) and their model counterpart. The cost function is minimized with respect to selected control variables and this is done iteratively using a gradient descent method. Variational assimilation overcomes many of the limitations of OI: it allows for greater flexibility for assimilating different observation types (possibly nonlinearly related to the model state); it eliminates the need for data selection so that all observations can in principle influence the analysis at every model grid-point; it provides a more general framework for using more sophisticated background-error covariance models; and it provides a clearer development path towards advanced, four-dimensional assimilation techniques. These advantages are equally relevant for oceanographic data assimilation.

In this paper, we describe three- and four-dimensional variational assimilation (3D- and 4D-Var) systems that have been developed for the rigid-lid version of the OPA Ocean General Circulation Model (OGCM) of the Laboratoire d'Océanographie DYnamique et de Climatologie (LODYC) (Madec *et al.* 1998). One of the main motivations for developing the system is to produce ocean analyses for seasonal climate forecasting. In the present study, the 3D- and 4D-Var systems are used to generate an extended set of analyses, covering the period 1993-98, for the tropical Pacific Ocean. Here, we evaluate the analyses by focussing on their climatological properties and comparison with independent data-sets, rather than their impact on climate forecasts.

Both the 3D- and 4D-Var systems have been designed following the incremental approach (Courtier *et al.* 1994). The control variable of the minimization problem is taken to be an increment to the background estimate of the model initial conditions at the beginning of a given assimilation window. In the cost function, the observations are compared to the sum of the background counterpart of the observations and an increment computed in observation space using a linear model. The fundamental difference between the 3D- and 4D-Var formulations lies in the level of sophistication of the linear model used to transport the state increment between observation times. In 3D-Var, a simple persistence model is used, whereas in 4D-Var a dynamical model based on the tangent-linear (TL) of the OPA OGCM is used. 4D-Var involves substantially more development than 3D-Var since an adjoint model must be derived for the linearized version of the OGCM in order to compute the gradient of the cost function with respect to the increment at initial time.

This particular incremental version of 3D-Var can be viewed as a limiting case of incremental 4D-Var in which the TL operator is replaced by the identity matrix. Observations can be assimilated at their appropriate measurement times since they are compared directly to the background state which is propagated in time using the OGCM. For this reason, the scheme has been coined 3D-FGAT for First-Guess at Appropriate Time (Fisher and Andersson 2001)[1] In this respect, 3D-Var partly overcomes the first limitation of the OI mentioned above. Another important difference with the OI is that the observations are assimilated at their appropriate depths. The increments at the observation points are smoothed onto model levels in the variational analysis using the adjoint of an interpolation operator and the vertical background-error covariances. As with the OI, our current 3D-Var system is univariate and assimilates temperature information only.

In incremental 4D-Var, the dynamical model used to propagate the increment provides a time-dependent multivariate constraint on the analysis. Incremental 4D-Var is derived as an approximation to the complete 4D-Var problem in which the full nonlinear model (here an OGCM) is imposed as a constraint in the cost function with the model initial conditions taken as the control variables (Lewis and Derber 1985; Le Dimet and Talagrand 1986; Talagrand and Courtier 1987). In oceanography, most 4D-Var-related applications to date with OGCMs have concentrated on solving the complete problem directly, and in some cases using different or additional control variables (e.g., surface forcing fields) (Tzipermann *et al.* 1992a,b; Tzipermann and Sirkes 1997; Yu and Malanotte-Rizzoli 1998; Maroztke and Wunsch 1993; Lee and Maroztke 1997, 1998; Greiner *et al.* 1998a,b, 2000; Bonekamp *et al.* 2001). The incremental formulation was introduced in meteorol-

---

[1] The 40-year atmospheric reanalysis project (ERA-40) at ECMWF employs an FGAT version of 3D-Var.

ogy to overcome some important practical difficulties with solving the complete 4D-Var problem directly. In the latter, nonlinearities in the model constraint can significantly complicate the structure of the cost function and prevent its minimization at a reasonable computational cost using a gradient descent method. Furthermore, in order to compute a numerically accurate gradient, the adjoint of the *exact* TL of the full nonlinear model is required. When the nonlinear model contains discontinuous parametrisations or numerics, an accurate derivation of these models can be particularly difficult (Xu 1996).

The incremental algorithm should be viewed as a practical algorithm for solving the complete problem. As constraints are linear, the cost function is quadratic and minimization with a gradient descent method is generally much more efficient. In the present study, our main objective is to reconstruct the large-scale, low-frequency component of the tropical ocean circulation which is well known to be largely governed by linear wave dynamics (e.g., see Philander 1989). Therefore, *a priori* the linearity assumption in incremental 4D-Var would not appear to be a very restrictive one. More generally, however, nonlinear effects can be partly accounted for by introducing a feedback (outer) loop in the algorithm to update the basic state of the linear model with increments generated during minimization (the inner loop) (Courtier *et al.* 1994; Laroche and Gauthier 1998). In terms of reducing the amount of technical development, the incremental formulation has a distinct advantage over the complete formulation as the linear and adjoint models can be greatly simplified by smoothing or neglecting discontinuous parametrisations (Mahfouf 1999). For example, this latter point has been exploited in the present study to neglect changes in vertical diffusion coefficients associated with perturbations in temperature, salinity and velocity. Finally, the computational cost of 4D-Var may also be significantly reduced by computing the increments at lower resolution than that of the full model (Rabier *et al.* 2000), although this is not an issue in our present system which employs a relatively low resolution version of the OGCM.

The purpose of this paper is twofold: first, to give a thorough description of the current 3D- and 4D-Var systems; and second, to provide a detailed evaluation and intercomparison of tropical Pacific Ocean analyses generated by the two systems. Some comparisons with the ECMWF OI, which has also been implemented in our tropical Pacific version of OPA, will also be carried out. The organisation of the paper is as follows. Section 2 describes the general formulation of the incremental 3D- and 4D-Var problems. In section 3, the different system components are described. In section 4, several diagnostics are presented to highlight some of the important properties of the two systems. In section 5, the analyses are presented, and evaluated by examining their climatological properties (mean and variability) and by comparing them to independent observations. A summary and discussion are given in section 6. Appendices provide some mathematical details on the incremental algorithm and the implications of the rigid-lid constraint in 4D-Var.

## 2 Formulation of the 3D- and 4D-Var problems

### 2.1 Incremental formulation

The notation used in this paper closely follows the recommendations of Ide *et al.* (1997). Let $\mathbf{w}$ denote the ocean state vector. The components of $\mathbf{w}$ consist of those model variables that are to be estimated from observations to produce the analysis $\mathbf{w}^a$. A model forecast, initiated from a previous analysis, provides a prior or background estimate, $\mathbf{w}^b$, of $\mathbf{w}$. Since $\mathbf{w}^b$ will already be close in some sense to the "true" state we wish to estimate, it is convenient to formulate the estimation problem in terms of an increment, $\delta\mathbf{w}$, where

$$\mathbf{w} = \mathbf{w}^b + \delta\mathbf{w}. \tag{1}$$

The state vector is propagated in time by the ocean model

$$\mathbf{w}(t_i) = M(t_i, t_{i-1})(\mathbf{w}(t_{i-1})) \tag{2}$$

where $M = M(t_i, t_{i-1})$ represents the nonlinear model operator acting on $\mathbf{w}(t_{i-1})$ between times $t_{i-1}$ and $t_i$. Substituting (1) into (2) and expanding (2) about $\mathbf{w}^b(t_{i-1})$ gives, to first order,

$$\mathbf{w}(t_i) \approx M(t_i, t_{i-1})(\mathbf{w}^b(t_{i-1})) + \mathbf{M}(t_i, t_{i-1})\delta\mathbf{w}(t_{i-1}) \tag{3}$$

where $\mathbf{M} = \mathbf{M}(t_i, t_{i-1})$ denotes a linear operator that acts on $\delta\mathbf{w}(t_{i-1})$ between times $t_{i-1}$ and $t_i$. If $\mathbf{M}$ is taken to be an exact linearization of $M$ about $\mathbf{w}^b(t_i)$ then $\mathbf{M} \equiv (\partial M/\partial\mathbf{w})|_{\mathbf{w}=\mathbf{w}^b}$ is the tangent-linear (TL) operator, and

$$\delta\mathbf{w}(t_i) = \mathbf{M}(t_i, t_{i-1})\delta\mathbf{w}(t_{i-1}) \tag{4}$$

is the corresponding TL model. More generally, $\mathbf{M}$ may be taken to be any linear operator that verifies the approximation (3). Indeed, the fundamental difference between the 3D- and 4D-Var formulations used in this study lies in the choice of $\mathbf{M}$, as detailed in section 2.2.

Now, let $\mathbf{y}_i^o$ denote the observation vector at time $t_i$. The model equivalent of $\mathbf{y}_i^o$ is

$$H_i(\mathbf{w}(t_i)) \approx H_i(\mathbf{w}^b(t_i)) + \mathbf{H}_i\delta\mathbf{w}(t_i) \tag{5}$$

where $H_i$ is the observation operator at $t_i$, and $\mathbf{H}_i$ is a linear approximation to $H_i$. Assuming that a time-sequence of observation vectors is available over an interval $t_0 \le t_i \le t_n$, then the model estimates of the observations within this interval can be directly related to the model initial conditions since $\mathbf{w}(t) = M(t_i, t_0)(\mathbf{w}(t_0))$ where $M(t_i, t_0) \equiv M(t_i, t_{i-1})\cdots M(t_1, t_0)$. Thus,

$$H_i(\mathbf{w}(t_i)) = G_i(\mathbf{w}(t_0)) \approx G_i(\mathbf{w}^b(t_0)) + \mathbf{G}_i\delta\mathbf{w}(t_0) \tag{6}$$

where the combined operator $G_i = H_i M(t_i, t_0)$ is a generalized observation operator and $\mathbf{G}_i = \mathbf{H}_i\mathbf{M}(t_i, t_0)$ is its linearized counterpart with $\mathbf{M}(t_i, t_0) \equiv \mathbf{M}(t_i, t_{i-1})\cdots\mathbf{M}(t_1, t_0)$.

In variational assimilation, the analysis is defined as the state vector $\mathbf{w}^a = \mathbf{w}^a(t_0)$ that simultaneously minimizes the "distance" to the background state $\mathbf{w}^b = \mathbf{w}^b(t_0)$ and to the time-sequence of observations $\mathbf{y}_i^o$ on $t_0 \le t_i \le t_n$. Distance is defined by an inner product (a cost function $J^F$) whose weighting metric takes into account the statistical accuracy of the background and observational information. Expressed as a function of the increment $\delta\mathbf{w} = \delta\mathbf{w}(t_0)$, which constitutes the control vector of the minimization problem, $J^F$ may be written as

$$J^F(\delta\mathbf{w}) = \underbrace{\frac{1}{2}\delta\mathbf{w}^T\mathbf{B}^{-1}\delta\mathbf{w}}_{J_b} + \underbrace{\frac{1}{2}\sum_{i=0}^{n}\left[G_i(\mathbf{w}^b + \delta\mathbf{w}) - \mathbf{y}_i^o\right]^T\mathbf{R}_i^{-1}\left[G_i(\mathbf{w}^b + \delta\mathbf{w}) - \mathbf{y}_i^o\right]}_{J_o^F} \tag{7}$$

where the matrices $\mathbf{B}$ and $\mathbf{R}_i$ contain estimates of the covariances of background and observation error, respectively. In (7) the observation errors are assumed to be uncorrelated in time and uncorrelated with the background error. The observation term $(J_o^F)$ measures the fit between the observations and their model equivalent. The background term $(J_b)$ penalizes the size of the increment (i.e., measures the fit to the background state). The analysis is given by $\mathbf{w}^a = \mathbf{w}^b + \delta\mathbf{w}^a$ where $\delta\mathbf{w}^a$ is the increment that minimizes $J^F$.

In the *incremental* formulation of variational assimilation (Courtier *et al.* 1994), (7) is approximated by a *quadratic* cost function $J$ in $\delta\mathbf{w}$ by replacing $G_i(\mathbf{w}^b + \delta\mathbf{w})$ with its linearized counterpart (6). This results in an important practical simplification to the minimization problem, from one with potentially many minima due to the nonlinearity in $G_i$, to one with a unique minimum as guaranteed by the linearity of $\mathbf{G}_i$. The simplified cost function reads

$$J(\delta\mathbf{w}) = \underbrace{\frac{1}{2}\delta\mathbf{w}^T \mathbf{B}^{-1}\delta\mathbf{w}}_{J_b} + \underbrace{\frac{1}{2}\sum_{i=0}^{n}\left[\mathbf{G}_i\delta\mathbf{w} - \mathbf{d}_i\right]^T \mathbf{R}_i^{-1}\left[\mathbf{G}_i\delta\mathbf{w} - \mathbf{d}_i\right]}_{J_o} \tag{8}$$

where the innovation vector

$$\mathbf{d}_i = \mathbf{y}_i^o - G_i(\mathbf{w}^b) = \mathbf{y}_i^o - H_i(\mathbf{w}^b(t_i)) \tag{9}$$

plays the role of an *effective* observation vector. For convenience of notation, the time summation in (8) may be eliminated by defining $\mathbf{d} = (...,\mathbf{d}_i^T,...)^T$, $\mathbf{G} = (...,\mathbf{G}_i^T,...)^T$, and $\mathbf{R} = \mathrm{diag}(...,\mathbf{R}_i,...)$, a block-diagonal matrix, to yield

$$J(\delta\mathbf{w}) = \frac{1}{2}\delta\mathbf{w}^T \mathbf{B}^{-1}\delta\mathbf{w} + \frac{1}{2}\left[\mathbf{G}\,\delta\mathbf{w} - \mathbf{d}\right]^T \mathbf{R}^{-1}\left[\mathbf{G}\,\delta\mathbf{w} - \mathbf{d}\right]. \tag{10}$$

The minimizing solution (analysis increment) is now readily obtained by setting the gradient of (10) to zero and solving for $\delta\mathbf{w}$ (Lorenc 1986; Tarantola 1987):

$$\delta\mathbf{w}^a = \left(\mathbf{B}^{-1} + \mathbf{G}^T\mathbf{R}^{-1}\mathbf{G}\right)^{-1}\mathbf{G}^T\mathbf{R}^{-1}\mathbf{d} \tag{11}$$

$$= \mathbf{B}\mathbf{G}^T\left(\mathbf{G}\mathbf{B}\mathbf{G}^T + \mathbf{R}\right)^{-1}\mathbf{d}. \tag{12}$$

In practice, the cost function (8) is minimized approximately using an iterative gradient descent method. The increment is updated on each iteration using the gradient of the cost function with respect to the increment. As outlined in section 2.3, the gradient of the $J_o$-term with respect to the increment can be obtained efficiently using the adjoint of the linear model (4). A feedback between the linear and nonlinear models can then be introduced by allowing the basic state-trajectory of the linear model to be regularly updated with the most recent estimate of the state trajectory obtained during minimization (Courtier *et al.* 1994). The updates are performed on an *outer* loop of the assimilation algorithm, while the iterations of the actual minimization are performed within an *inner* loop (see Appendix A). With frequent updates, the accuracy of the linear model should improve and the minimum of the incremental cost function should be closer to that of the original (non-incremental) cost function (7) involving the nonlinear model (Laroche and Gauthier 1998). This provides a practical way of accounting for nonlinearities in the assimilation algorithm while retaining the computational advantages of a quadratic minimization problem.

## 2.2 The increment propagator

As pointed out in section 2.1, our 3D- and 4D-Var formulations differ principally in the choice of the linear increment-operator $\mathbf{M}$. In the 3D-Var, the increment is evolved by a simple persistence model which corresponds to setting $\mathbf{M}$ to the identity matrix ($\mathbf{M}_{3\mathrm{DVar}} \equiv \mathbf{I}$). In the 4D-Var, the increment is propagated by an approximation to the TL model ($\mathbf{M}_{4\mathrm{DVar}} \approx (\partial M/\partial\mathbf{w})|_{\mathbf{w}=\mathbf{w}^b}$), the main approximation being introduced in the parametrization of vertical mixing as described in more detail in section 3.2.

An important feature of this formulation of 3D-Var is that the observations are compared with the model background at their *correct* measurement times. This differs from the more traditional implementation of 3D-Var in which the observations are assimilated concurrently, usually at the centre of the assimilation interval, which is tantamount to assuming that *all* observations are valid at the same time. In the FGAT formulation, observations that are already close to the model background will produce a small innovation (Eq. (9)) and will not have a large impact on the analysis. This may not be the case in the classical approach in which artificially large innovations may be generated simply because of a temporal inconsistency. As discussed by Fisher and Andersson (2001), this may lead to a potentially large mean analysis error. For example, this could easily arise for a Kelvin wave which in 10-days[2] can travel more than 2000 km. Moreover, from a technical point of view, the incremental approach provides a much cleaner development path from 3D- to 4D-Var.

## 2.3 Preconditioning

In order to improve the convergence properties of the minimization, a preconditioning is employed by which the cost function is redefined in terms of a nondimensional variable

$$\mathbf{v} = \mathbf{U}^{-I}\delta\mathbf{w} \tag{13}$$

where $\mathbf{U}$ is a rectangular matrix defined such that $\mathbf{B} = \mathbf{U}\mathbf{U}^T$ and $\mathbf{B}^{-1} = (\mathbf{U}^{-I})^T\mathbf{U}^{-I}$. The superscript $-I$ denotes generalized (right) inverse. Introducing the transformation (13) directly into (10) leads to the preconditioned problem of minimizing

$$J(\mathbf{v}) = \frac{1}{2}\mathbf{v}^T\mathbf{v} + \frac{1}{2}\left[\mathbf{G}\,\delta\mathbf{w} - \mathbf{d}\right]^T\mathbf{R}^{-1}\left[\mathbf{G}\,\delta\mathbf{w} - \mathbf{d}\right] \tag{14}$$

where

$$\delta\mathbf{w} = \mathbf{U}\mathbf{v}. \tag{15}$$

The variational analysis problem is solved directly in $\mathbf{v}$-space, and then transformed back to model space using (15). The conditioning of the $J_b$ term in $\mathbf{v}$-space is optimal in the sense that the Hessian of $J_b$ (the matrix of second-derivatives of $J_b$) is the identity matrix. For the special case of a single observation, the convergence of the minimization in $\mathbf{v}$-space is achieved in a single iteration using a gradient descent method with an exact line search.

On each iteration of the minimization, the gradient of $J$ with respect to $\mathbf{v}$ is required. The gradient computation proceeds as follows. First, the gradient of the $J_o$ term with respect to $\delta\mathbf{w}$ is evaluated through a single backward integration, from $t_{n+1}$ to $t_0$, of the forced adjoint model (Lewis and Derber 1985; Le Dimet and Talagrand 1986; Talagrand and Courtier 1987; Thacker and Long 1988)

$$\mathbf{p}(t_i) = \mathbf{M}(t_{i+1}, t_i)^T\mathbf{p}(t_{i+1}) + \mathbf{H}_i^T\mathbf{R}_i^{-1}\left[\mathbf{H}_i\delta\mathbf{w}(t_i) - \mathbf{d}_i\right] \tag{16}$$

where $\mathbf{p}(t_i)$ is the adjoint state vector with $\mathbf{p}(t_{n+1}) = 0$ and $\mathbf{p} = \mathbf{p}(t_0) = \nabla_{\delta\mathbf{w}}J_o$. For the FGAT version of 3D-Var, (16) simply implies a summation of the forcing terms within the interval. Then, applying the adjoint of the transformation (15) to $\mathbf{p}$ gives the gradient of $J_o$ with respect to $\mathbf{v}$. Finally, the sum of the gradients of $J_o$ and $J_b$ gives the total gradient;

$$\nabla_{\mathbf{v}}J = \nabla_{\mathbf{v}}J_b + \nabla_{\mathbf{v}}J_o = \mathbf{v} + \mathbf{U}^T\mathbf{p}. \tag{17}$$

Besides acting as an efficient preconditioner, another practical advantage of this formulation is that the inverse transformation (13) from $\delta\mathbf{w}$ to $\mathbf{v}$ (involving $\mathbf{U}^{-I}$) is never actually needed, providing the initial guess for minimization is taken to be $\mathbf{w} = \mathbf{w}^b$ (Courtier 1997; Derber and Bouttier 1999). In this case, $\delta\mathbf{w} = \mathbf{v} = 0$

---

[2]Ten days is a typical window width used in OI-type ocean analysis systems such as the operational system at ECMWF (Alves *et al.* 1998). It is also the window width used for the 3D-Var experiments presented here.

and the $J_b$ term has no influence on the minimization on the first iteration. The minimization then proceeds in **v**-space, with each new estimate of **v** passing through the transformation (15) to provide a new estimate of $\delta\mathbf{w}$ which is needed to compute the increment-minus-innovation residual in (14) and (16). The definition of **B** through this transformation is an important design feature of the assimilation algorithm and is discussed in more detail in section 3.3.

The minimization routine used in this study is the limited memory quasi-Newton algorithm M1QN3 of Gilbert and Lemaréchal (1989). An exact line search has been employed with M1QN3 in order to improve the efficiency of the algorithm for quadratic minimization problems. The so-called "warm" start facility of M1QN3 is also employed when more than one outer loop is performed in order to precondition the minimization using the information accumulated on the Hessian matrix during the preceding minimization.

## 2.4 The nonlinear analysis trajectory

The minimizing solution of the quadratic cost function (8) is a trajectory of increments $\delta\mathbf{w}^a(t_i)$ which satisfies exactly the equations of the linear model (4). The corresponding model trajectory $\mathbf{w}^b(t_i) + \delta\mathbf{w}^a(t_i)$ is used in the $J_o$ term to compare with the observations (Eq. 8). It will be convenient to refer to this trajectory as the *linear* analysis in order to distinguish it from the *nonlinear* "analysis" trajectory $\mathbf{w}^a(t_i)$ defined below. We will return to this point in sections 4.6 and 5.2.

There are several ways the analysis increment $\delta\mathbf{w}^a$ may be used to correct the trajectory of the nonlinear model. Two different approaches have been adopted in our 3D-Var and 4D-Var systems. Since our current assimilation system incorporates only temperature observations and relies on a univariate formulation of the background-error covariance matrix (section 3.3), the 3D-Var produces an analysis increment for the temperature field only. A practical way of adjusting the nonanalysed model fields while minimizing spurious adjustment processes, is to apply the analysis increment gradually through a forcing term in the prognostic model equations:

$$\mathbf{w}^a(t_i) = M(t_i, t_{i-1})(\mathbf{w}^a(t_{i-1})) + F(t_i)\delta\mathbf{w}^a \tag{18}$$

where $\mathbf{w}^a(t_0) = \mathbf{w}^b$, and $F(t_i)$ is a weighting function defined such that $\sum_{i=0}^{n} F(t_i) = 1$ so as to conserve the time-integrated value of the analysis increment $\delta\mathbf{w}^a$. The forcing term can be shown to behave as a low-pass time filter (Bloom *et al.* 1996). In this study, the temperature increment is applied uniformly over the time-window via a constant forcing $F = 1/n$. A similar procedure has been adopted in the ECMWF ocean analysis system (Alves *et al.* 1998), and is illustrated schematically in Fig. 1a.

In contrast to the 3D-Var, the 4D-Var produces a multivariate analysis increment by virtue of the TL model dynamics which act to couple the different increment variables. To a large extent, this dynamical coupling serves as a balance constraint on the analysis. As such, in producing the analysis trajectory, we choose to initialize the nonlinear model directly using the analysis at $t_0$;

$$\mathbf{w}^a(t_i) = M(t_i, t_0)(\mathbf{w}^a(t_0)) \tag{19}$$

where $\mathbf{w}^a(t_0) = \mathbf{w}^b + \delta\mathbf{w}^a$ (Fig. 1b). Finally, when cycling the 3D- or 4D-Var over an extended period, the analysis obtained from the trajectory at the end of the interval is taken to be the background state for a variational analysis performed on the following interval (Fig. 1).

# a) Cycling of 3D-Var
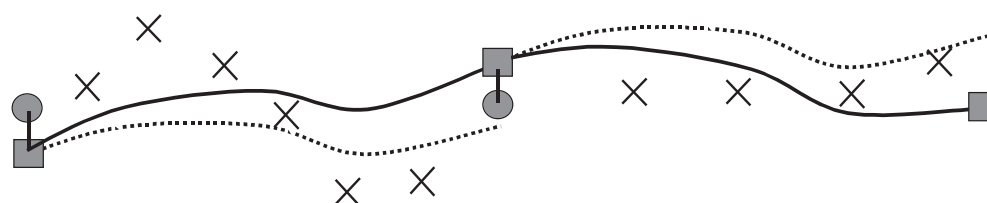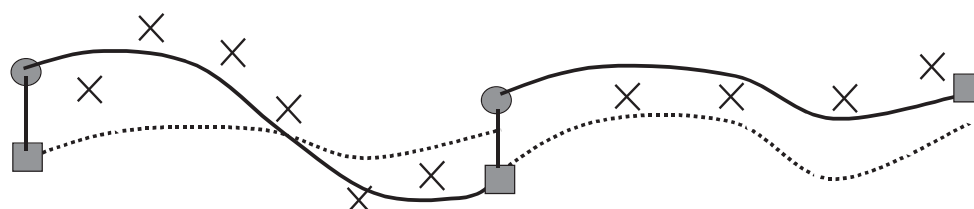


# b) Cycling of 4D-Var



*Figure 1: Schematic representation of the cycling procedures used for a) 3D-Var and b) 4D-Var. Two cycles are illustrated in each sketch. The dotted (solid) curves correspond to the background (analysis) trajectory; the cross symbols denote observations. The shaded square (circle) at the beginning of each cycle denotes the background (analysed) initial state. Note that in 4D-Var the analysis increment (represented by the difference between the shaded square and circle) is applied directly to the background initial state to produce the analysis trajectory, whereas in 3D-Var it is applied gradually as a forcing to the model equations. This explains why in 3D-Var the analysis and background start from the same point at the beginning of each cycle.*

# 3 Components of the assimilation system

## 3.1 The ocean model

The ocean model used in this study is the OPA OGCM of the Laboratoire d'Océanographie Dynamique et de Climatologie (Madec *et al.* 1998). The model solves the primitive equations for horizontal currents $\mathbf{u} = (u, v)$, potential temperature $T_\theta$ and salinity $S$. The equations are formulated in orthogonal curvilinear $z$-coordinates and discretized using finite differences on an Arakawa C-grid. The basic configuration of the model is described in Vialard *et al.* (2001). It covers the tropical Pacific Ocean from $120^\circ$E to $70^\circ$W, and $30^\circ$N to $30^\circ$S. The zonal resolution is $1^\circ$ and the meridional resolution varies from $0.5^\circ$ at the equator to $2^\circ$ at the northern and southern boundaries. The model has 25 levels, with a resolution of 10m in the upper 130m, increasing to 1000m in the bottom level. The vertical distribution of temperature grid points has been chosen to match as closely as possible the location of temperature sensors on the TAO moorings. Realistic bathymetry is included using the Levitus (1982) land-sea mask.

The equation of state for seawater is defined by the Jackett and McDougall (1995) formula. The effects of unresolved small-scale processes on the flow are parametrized using a Laplacian-type mixing along and perpendicular to the geopotential surfaces. The horizontal mixing coefficients are set to $2000\,\mathrm{m^2\,s^{-1}}$ in the equatorial strip, with somewhat larger values in off-equatorial regions and near the boundaries. The vertical mixing coefficients are computed from a 1.5 turbulent closure scheme. The scheme involves the solution of a prognostic equation for turbulent kinetic energy (TKE) (Blanke and Delecluse 1993). Convective adjustment is parametrized using an enhanced vertical diffusion; i.e., when a static instability is detected, the local vertical diffusion coefficients for momentum and tracers are set to a large value ($0.5\,\mathrm{m^2\,s^{-1}}$). The vertical diffusion terms are solved using an implicit time-discretization scheme. The time step is 1.5 hrs.

At solid boundaries, conditions of no-slip and no-normal flux are applied on the velocity and tracer fields, respectively. At the ocean surface ($z = 0$), a rigid-lid and no-volume flux condition is applied (Roullet and Madec 2000). An obvious consequence of the rigid-lid condition is that, unlike in a free-surface model, there is no prognostic equation for sea-surface height ($\eta = 0$). The no-volume flux condition is an additional requirement that the vertical velocity identically vanish at the surface ($w = 0$ at $z = 0$), and hence from the continuity equation, that the horizontal velocity field $(u, v)$ is nondivergent (Bryan 1969). The latter condition is satisfied by defining the $(u, v)$-field through a barotropic streamfunction $\psi$ and a set of independent baroclinic velocities $(\hat{u}, \hat{v})$. This leads to some important technical difficulties in formulating the 4D-Var as detailed in Appendix B.

Surface fluxes of momentum, heat and fresh water are prescribed at the ocean-atmosphere interface. The momentum flux is specified through weekly wind-stress products from the ERS scatterometer (Grima *et al.* 1999). The heat and fresh water fluxes are specified as a daily climatology computed from the European Centre for Medium-range Weather Forecasts (ECMWF) reanalysis (Gibson *et al.* 1996). The solar and nonsolar components of the heat flux are specified separately in order to allow penetration of the shortwave radiation in the upper ocean. A relaxation to weekly analyses of sea surface temperature (SST) (Reynolds and Smith 1994) is applied through a Newtonian damping term added to the surface (nonsolar) heat flux. The relaxation coefficient is set to $-40\,\mathrm{W\,m^{-2}\,K^{-1}}$, which for a depth-scale of 50m corresponds to a restoring time-scale of one month. No relaxation is applied to sea surface salinity. In the control integration in which no data are assimilated, a damping to Levitus climatological temperature and salinity is applied outside the $10^\circ$S to $10^\circ$N band, below the surface mixed-layer.

## 3.2 The tangent-linear and adjoint models

The numerical codes of the TL and adjoint models have been derived directly from the numerical code of the nonlinear model by applying standard (hand-coding) techniques (Talagrand 1991; Giering and Kaminski 1998).

The task is straightforward but requires rigorous testing at various levels of the code. Standard tests are available (Thépaut and Courtier 1991) for checking both the numerical accuracy of the linearization and the numerical consistency of the TL and adjoint codes. These tests have been integrated into a comprehensive validation module which is called routinely each time the codes are modified.

Some approximations have been introduced in the TL and adjoint models. The most important one is in the parametrization of vertical diffusion, as described in more detail below. Another one relies on an intermittent storage of the basic state trajectory to reduce computer memory requirements. In our experiments, the basic state has been stored once per day (every 16 time steps) and defined at intermediate times through linear interpolation. The impact of this approximation on the accuracy of the TL model was minor. Finally, to reduce the CPU cost of the adjoint integration, an approximation has been introduced in the adjoint of the elliptic solver which is applied on each time step to enforce the nondivergence constraint on the vertically integrated velocity. Details can be found in Appendix B.3.

*Simplified vertical diffusion*

Let $\alpha$ denote one of the prognostic state variables $u$, $v$, $T_\theta$ or $S$. In the complete TL model, the tendency of a perturbation $\delta\alpha$ produced by vertical diffusion is described by the two-term partial differential equation

$$\frac{\partial\delta\alpha}{\partial t} = \frac{\partial}{\partial z}\left(A_v\frac{\partial\delta\alpha}{\partial z}\right) + \frac{\partial}{\partial z}\left(\delta A_v\frac{\partial\alpha}{\partial z}\right) \tag{20}$$

where $A_v = A_v(u, v, T_\theta, S)$ is the vertical diffusion coefficient and $\delta A_v = (\partial A_v/\partial u)\,\delta u + (\partial A_v/\partial v)\,\delta v + (\partial A_v/\partial S)\,\delta S + (\partial A_v/\partial T_\theta)\,\delta T_\theta$ is the perturbation of $A_v$ resulting from perturbations of $u$, $v$, $T_\theta$ and $S$. The first term on the right hand side of (20) is a standard diffusion operator with coefficient $A_v$. In the incremental algorithm, $A_v$ is updated on each outer iteration and held constant only during the inner iterations. The second term on the right hand side of (20) is more problematic because of both theoretical and practical difficulties in computing the perturbation $\delta A_v$. First, a direct computation of $\delta A_v$ would involve linearizing the TKE and enhanced vertical diffusion schemes. These parametrization schemes are highly nonlinear and discontinuous so any attempt to linearize them directly would have to be done with considerable caution (Xu 1996; Zou 1997). Discontinuities are a well-known source of numerical noise in the TL model. One possibility for reducing such noise is to derive $\delta A_v$ from a suitably smooth approximation to the original nonlinear scheme (Janiskova *et al.* 1999). Generally speaking, however, the problem is more complex than that of simply smoothing isolated discontinuities as the second term in (20) contains other generating mechanisms of spurious noise, which are present even in smoothed parametrization schemes (Mahfouf 1999; Zhu and Kamachi 2000). The simplest way of avoiding these potential noise problems is to neglect the second term altogether by setting $\delta A_v \equiv 0$. This simplification, which has been used extensively in meteorology (e.g., Mahfouf 1999), is adopted here. Implementing a more elaborate linear physics parametrization was considered premature at this stage without first evaluating the assimilation results using the simplified scheme.

## 3.3   The background-error covariance matrix

The background-error covariance matrix (**B**) plays an important role in determining the spatial structure of the analysis increment in both 3D- and 4D-Var. There are two basic difficulties in specifying **B**. First, given the sparsity of ocean observations, it is difficult, if not impossible, to obtain complete and accurate estimates of the covariances, even in the tropical Pacific which is one of the best-observed ocean basins. Second, even if there were sufficient observations, the sheer size of **B** (roughly $5 \times 10^{1}$ elements in our application) means that this matrix cannot be stored explicitly and so must be simplified. In practice, this is done by *modelling* the covariances using analytical functions or filters which depend on a limited number of tunable parameters and which are numerically efficient for large-scale problems.

In our current system, $\mathbf{B}$ is univariate (three-block diagonal with respect to horizontal velocity, temperature and salinity) and includes a relatively simple correlation model. $\mathbf{B}$ is constructed as a symmetric product of several operators:

$$\mathbf{B} = \mathbf{S}\boldsymbol{\Sigma}\underbrace{\boldsymbol{\Lambda}\mathbf{L}^{1/2}\mathbf{W}^{-1}\mathbf{L}^{T/2}\boldsymbol{\Lambda}}_{\mathbf{C}}\boldsymbol{\Sigma}\mathbf{S}^T \tag{21}$$

$$= \underbrace{\left(\mathbf{S}\boldsymbol{\Sigma}\boldsymbol{\Lambda}\mathbf{L}^{1/2}\mathbf{W}^{-1/2}\right)}_{\mathbf{U}}\underbrace{\left(\mathbf{W}^{-1/2}\mathbf{L}^{T/2}\boldsymbol{\Lambda}\boldsymbol{\Sigma}\mathbf{S}^T\right)}_{\mathbf{U}^T} \tag{22}$$

where $\mathbf{L}$ is a 3D filtering operator which is *self-adjoint* with respect to the scalar product whose metric is the diagonal matrix $\mathbf{W}$ of volume elements; $\boldsymbol{\Lambda}$ and $\boldsymbol{\Sigma}$ are diagonal matrices of normalization factors and background-error standard deviations, respectively; and $\mathbf{S}$ is a simplification operator that maps the horizontal components of total velocity $(u, v)$ into *independent* components $(\psi, \widehat{u}, \widehat{v})$ (see Appendix B.1 and B.2).

The underbraces in (22) highlight the preconditioning matrix in (15) and its adjoint in (17), which written explicitly in operator form are

$$\delta\mathbf{w} = \mathbf{S}\boldsymbol{\Sigma}\boldsymbol{\Lambda}\mathbf{L}^{1/2}\mathbf{W}^{-1/2}\mathbf{v} \tag{23}$$

and

$$\nabla_{\mathbf{v}}J_o = \mathbf{W}^{-1/2}\mathbf{L}^{T/2}\boldsymbol{\Lambda}\boldsymbol{\Sigma}\mathbf{S}^T\nabla_{\delta\mathbf{w}}J_o. \tag{24}$$

The underbrace in (21) highlights that part of $\mathbf{B}$ corresponding to the correlation matrix $\mathbf{C}$. The univariate correlations in $\mathbf{C}$ are modelled implicitly with the filter $\mathbf{L}$. The vertical ($v$) and horizontal ($h$) correlations are modelled separately using a 1D filter $\mathbf{L}_v$ and 2D filter $\mathbf{L}_h$. The 3D correlation model is then constructed from the product $\mathbf{L} = \mathbf{L}_v\mathbf{L}_h$. Premultiplication of $\mathbf{L}$ by $\mathbf{W}^{-1}$ is needed to convert $\mathbf{L}$, which is self-adjoint (i.e., $\mathbf{L} = \mathbf{W}^{-1}\mathbf{L}^T\mathbf{W}$), into a *symmetric* (covariance) matrix $\mathbf{L}\mathbf{W}^{-1}$. Assuming that a factorization of the form $\mathbf{L} = \mathbf{L}^{1/2}\mathbf{L}^{1/2}$ can be found then it is straightforward to show that the factor $\mathbf{L}^{1/2}$ is also self-adjoint and hence that $\mathbf{L}\mathbf{W}^{-1} = \mathbf{L}^{1/2}\mathbf{W}^{-1}\mathbf{L}^{T/2}$. This is the practical form of the filter covariance matrix used for deriving the preconditioning factorization in (22). The diagonal normalization matrix $\boldsymbol{\Lambda}$ is needed to ensure that the variances (diagonal elements) of $\mathbf{C}$ are equal to unity. This is achieved by setting the diagonal elements of $\boldsymbol{\Lambda}$ to be the inverse of the square root of the corresponding diagonal elements of $\mathbf{L}\mathbf{W}^{-1}$. Procedures for computing these diagonal elements are discussed in Weaver and Courtier (2001).

Various filters exist for modelling correlation functions but some are better suited than others depending on the application. The complex boundaries associated with coastlines imposes a particular constraint for oceanographic applications. For such applications, Laplacian- or diffusion-based filters are particularly well suited (Derber and Rosati 1989; Egbert *et al.* 1994; Weaver and Courtier 2001). Here, a diffusion-based filter has been used to model both the vertical and horizontal correlations. $\mathbf{L}_v$ is defined by an explicit time-step integration of a 1D diffusion equation in the vertical direction, while $\mathbf{L}_h$ is defined by an explicit time-step integration a 2D diffusion equation over the sphere. The boundary conditions are chosen to be of Neumann-type and are imposed directly within the finite-difference expression for the Laplacian using a land-ocean mask (Madec *et al.* 1998).

Consider a 3D scalar input field $\widehat{\alpha} = \widehat{\alpha}(\lambda, \phi, z)$ where $\lambda$ is longitude, $\phi$ is latitude and $z$ is depth. For the special case when the diffusion coefficients are constant, horizontal boundaries are ignored, and $\widehat{\alpha}$ is assumed to vanish in the vicinity of the surface ($z = 0$) and bottom ($z = -D(\lambda, \phi)$) boundaries, then time-stepping the diffusion-based correlation model, with $\widehat{\alpha}$ as initial condition, is a numerically efficient way of solving the integral equation

$$\alpha(\lambda, \phi, z) = \int_{z'=-D}^{0}\int_{\lambda'=0}^{2\pi}\int_{\phi'=-\pi/2}^{\pi/2}\rho(\theta, z-z'; L_h, L_v)\widehat{\alpha}(\lambda', \phi', z')\cos\phi' \, d\phi' \, d\lambda' \, dz' \tag{25}$$
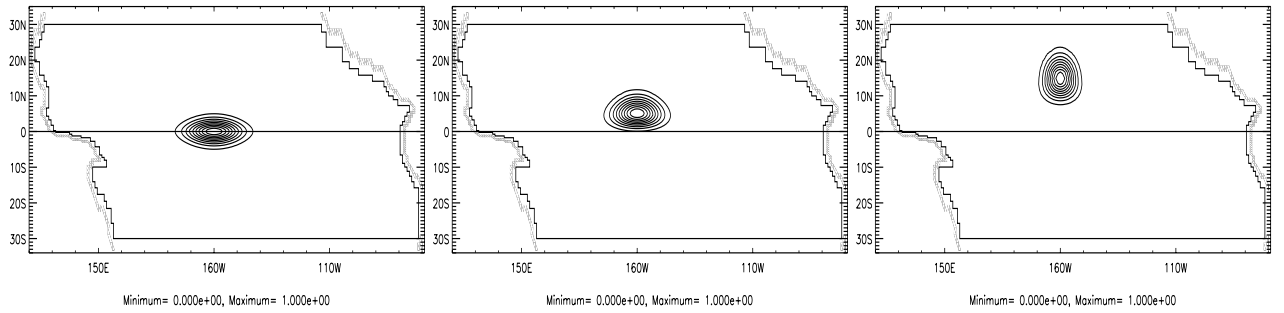
*Figure 2: The horizontal correlation functions for the tracer fields at latitudes a) 0°; b) 5°N; and c) 15°N. The contour interval is 0.1.*

where the kernel $\rho(\theta, z - z'; L_h, L_v)$ is a 3D correlation function, $\theta$ is the angular separation between points $(\lambda, \phi)$ and $(\lambda', \phi')$ on the sphere, and the parameters $L_h$ and $L_v$ are horizontal and vertical length scales. The 3D correlation function is separable in that it can be expressed as a product of a horizontal correlation function $\rho_h(\theta; L_h)$ and vertical correlation function $\rho_v(z - z'; L_v)$, which depend only on angular and vertical separation, respectively: $\rho(\theta, z - z'; L_h, L_v) = \rho_h(\theta; L_h)\rho_v(z - z'; L_v)$. The horizontal correlation function is isotropic and, for $L_h$ small compared to the Earth's radius $a$, well approximated by a Gaussian function of chordal distance $r = 2a\sin(\theta/2)$:

$$\rho_h(\theta(r); L_h) \approx \exp\left(-r^2/2L_h^2\right) \tag{26}$$

where $L_h \approx \sqrt{2\kappa_h T_h}$, $\kappa_h$ is the horizontal diffusion coefficient, and $T_h$ is the total integration "time" of the 2D diffusion equation. The vertical correlation function is homogeneous and isotropic, and exactly Gaussian:

$$\rho_v(z; L_v) = \exp\left(-z^2/2L_v^2\right) \tag{27}$$

where $L_v = \sqrt{2\kappa_v T_v}$ is the vertical length scale, $\kappa_v$ is the vertical diffusion coefficient, and $T_v$ is the total integration "time" of the 1D diffusion equation. A factor $\mathbf{L}^{1/2} = \mathbf{L}_v^{1/2}\mathbf{L}_h^{1/2}$, which is required in (22), can easily be deduced by defining it to be an integration of the diffusion model over half the "time" interval (respectively $T_v/2 = L_v^2/4\kappa_v$ and $T_h/2 = L_h^2/4\kappa_h$ for the 1D and 2D diffusion equations). It is also straightforward to generalize the diffusion model to account for non-Gaussian correlation functions although this possibility has not been explored in this study. Further details can be found in Weaver and Courtier (2001).

Equation (25) provides a useful interpretation of the diffusion-based correlation model in its simplest form. In practice, however, the correlation functions can be made anisotropic and can have their length scales varied geographically by introducing a tensor in the Laplacian operator (Weaver and Courtier 2001). For example, the diagonal elements of the tensor can be adjusted to allow for a local stretching and/or shrinking of the coordinates of the correlation model relative to those of the computational domain. This enables the correlation model to represent, for example, the well-observed feature that correlation length scales near the equator are longer in the zonal direction than in the meridional direction (Meyers *et al.* 1991; Kessler *et al.* 1996). Here, the horizontal length scales are taken to be a function of latitude and symmetric about the equator. The zonal and meridional length scales for the tracer fields have been defined to be $8°$ and $2°$, respectively, at the equator, and $4°$ in both directions poleward of $20°$N/S, with a linear transition between these values within the equatorial strip. The anisotropic ratio at the equator is consistent with the climatological observation statistics of Meyers *et al.* (1991), although the values of the actual length scales are somewhat smaller in our study. The values chosen here are broadly similar to those used in previous ocean data assimilation studies of the tropical Pacific (Smith *et al.* 1991; Behringer *et al.* 1998; Segschneider *et al.* 2002). The horizontal correlation functions for the tracer fields are illustrated in Fig. 2.

The horizontal correlations of the velocity field are modelled using a diffusion equation formed from the *vector* Laplacian rather than the scalar Laplacian used in the tracer diffusion model. The vector Laplacian has the
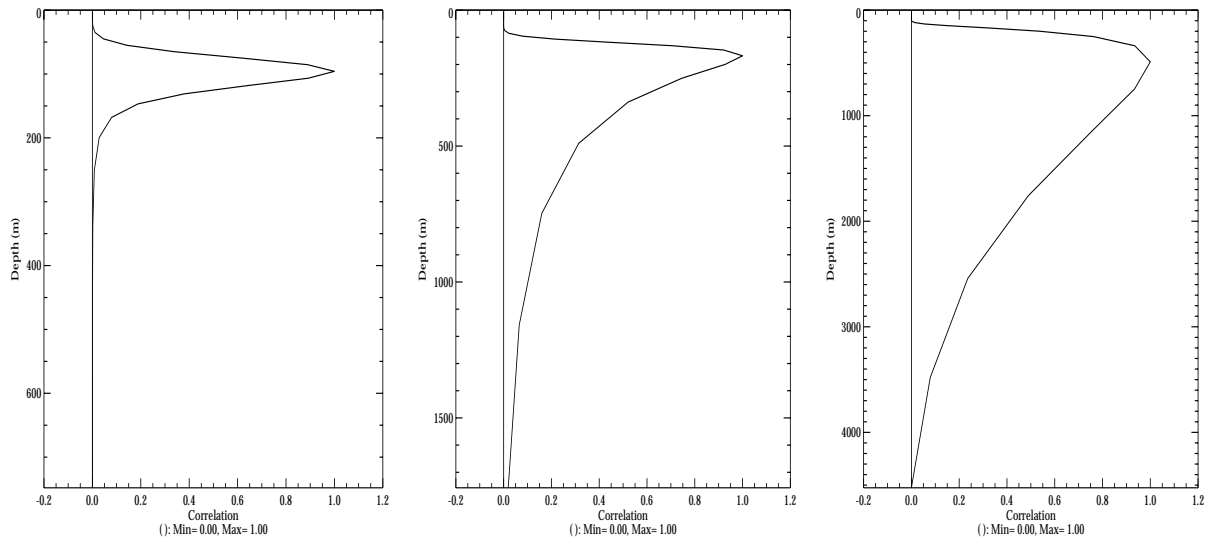
*Figure 3: The vertical correlation functions for the tracer fields at depths a) 96m (level 10); b) 168m (level 15); and c) 490m (level 19). Note the different scales on the vertical axes.*

desirable property of ensuring that the smoothing by the correlation function acts separately on the horizontal divergence and vorticity components of the velocity field (Madec *et al.* 1998). With the introduction of the anisotropic tensor, this is no longer strictly guaranteed. Geostrophy provides a natural constraint which allows us to estimate the length scale ($L_h^\zeta$) of the vorticity correlation functions ($\rho_h^\zeta$) based on the length scale ($L_h$) of the tracer correlation functions ($\rho_h$). For the special case of a homogeneous and isotropic field (see section 5.3 in Daley (1991)), an exact geostrophic coupling of the density and velocity fields implies that the correlation function for horizontal streamfunction $\widetilde{\psi}$ should be equal to that of density.[3] In terms of vorticity $\zeta = \nabla^2\widetilde{\psi}$, where $\nabla^2$ is the scalar Laplacian operator, the above condition becomes $\rho_h^\zeta = \nabla^4\rho_h$ (see section 5.2 in Daley (1991)). The length scale of $\rho_h^\zeta$ may be defined from (pg. 110, Daley 1991) $L_h^\zeta = \sqrt{-2\rho_h^\zeta/\nabla^2\rho_h^\zeta|_{r=0}} = \sqrt{-2\nabla^4\rho_h/\nabla^6\rho_h|_{r=0}}$. This leads to $L_h^\zeta \approx 0.6L_h$ where $L_h = \sqrt{-2\rho_h/\nabla^2\rho_h|_{r=0}}$ is the length scale in (26). Based on this simple analysis, the length scales for the vorticity correlations have been reduced by a factor of 0.6 relative to those for the tracer correlations. These smaller length scales have also been used for the divergence correlations. It is worth remarking that, while geostrophy has been used as a constraint for defining the length scales of the tracer and velocity correlation functions, our covariance model does not at present include a geostrophic balance constraint on the covariances themselves. Note also that the correlation model for the velocity background errors is not required in our univariate 3D-Var which assimilates temperature information only.

The vertical correlations of the velocity field are modelled using a diffusion equation that acts separately on the components $u$ and $v$. The vertical length scales for both the tracers and the velocity components are taken to be a function of depth with a dependence on the model's vertical resolution to provide adequate smoothing between model levels. At each model level, the vertical length scale is set to twice the depth of that level. This results in rather sharp correlations above the thermocline where the resolution is highest and much broader correlations below the thermocline where the resolution is coarsest (Fig.3).

The background-error standard deviations are allowed to vary with each grid-point and have been computed with respect to the climatological model mean obtained from a control run without data assimilation. This specification is based on the assumption that background errors are likely to be largest in regions of strong ocean variability (e.g., in the thermocline). The same background-error standard deviations are used at the

---

[3]Here $\widetilde{\psi}$ refers to the classical streamfunction defined from Helmoltz's theorem and is not to be confused with $\psi$, the barotropic streamfunction, defined in Appendix B.

beginning of each assimilation cycle.

## 3.4 Observations

The assimilation data-set consists of *in situ* temperature observations from the Global Temperature and Salinity Pilot Project (GTSPP) of the National Oceanographic Data Centre (NODC). This includes data from mainly TAO moorings and XBTs, and from a limited number of Conductivity-Temperature-Depth (CTD) casts and drifting buoys. A manual quality control procedure was used to remove suspicious data (Alves *et al.* 1998). Observations falling within the surface level of the model (between 0 and 10m) were also discarded to avoid potential redundancy with the observed SST (Reynolds and Smith 1994) used in the Newtonian damping term during outer iterations. The *in situ* temperatures retained for assimilation were then converted into potential temperature (the prognostic model variable) using the Bryden (1973) conversion formula (Eq. (A3.13) in Gill (1982)) with a reference salinity of 35.0 psu.

The observation-error covariances are assumed to be uncorrelated in space and time. The error variances are set to $(0.5^{\circ}\text{C})^2$ for TAO data and $(1.0^{\circ}\text{C})^2$ for all other data to ensure that the generally higher quality TAO data have more weight in the analysis. The observation operator $H$ consists of horizontal bilinear interpolation and vertical linear interpolation. For TAO data, $H$ also includes a time averaging since these data are available as daily averages.

# 4 Evaluation of 3D- and 4D-Var: internal diagnostics and consistency checks

The purpose of this section is to evaluate certain algorithmic and statistical properties of the 3D- and 4D-Var systems. The analyses themselves will be discussed in detail in section 5. First, in section 4.1, the assimilation experiments are introduced. In section 4.2, the validity of the linear assumption which underlies the incremental formulation is investigated. Convergence and optimality properties of the assimilation systems are then examined in sections 4.3 and 4.4. In section 4.5, some of the flow-dependent characteristics of the background-error statistics used implicitly in 4D-Var are examined in a simplified framework with single observations. Finally, in section 4.6, the statistics of the innovation and residual vectors are examined to assess the fit of the background and of the analysis to the assimilated observations.

## 4.1 Experimental set-up

Both the 3D- and 4D-Var have been cycled over the period 01 January 1993 to 30 December 1998 using a 10-day and 30-day assimilation interval, respectively. A total of 60 (inner) iterations of the minimization were performed per cycle, with an outer iteration performed every 10 inner iterations in 4D-Var. No outer iterations were performed in 3D-Var since $H_i$ is linear.[4] Two additional experiments were performed to provide a reference for evaluating 3D- and 4D-Var: a control experiment in which no data were assimilated, and an assimilation experiment using a univariate OI scheme (Smith *et al.* 1991) which is also employed in the operational seasonal forecasting system at ECMWF (Alves *et al.* 1998). For the OI, the background- and observation-error statistics have been chosen to match as closely as possible those used in 3D-Var. In all experiments (hereafter referred to as EX3D, EX4D, EXCL and EXOI), the initial conditions on 01 January 1993 were generated from a four-year spin-up of the model starting from rest and from Levitus (1982) climatological temperature and salinity. The wind-stress forcing used for the first three years of the spin-up was a climatology computed from the ERS wind-stress products. The final year of the spin-up was a transition year between ERS climatological and year 1992 products.

## 4.2 Validity of the linear increment models

Incremental variational assimilation is founded on the linear approximation (6). In this section, we wish to examine the validity of this approximation by checking the accuracy of both the persistence model used in 3D-Var on a 10-day window and the TL model used in 4D-Var on a 30-day window. The accuracy of each model can be assessed by comparing the time-evolution of an initial perturbation $\delta\mathbf{w}$ in the nonlinear (*NL*) model with its evolution in the linear (*L*) model. The nonlinear perturbation can be computed from the finite difference

$$\delta\mathbf{w}^{NL}(t_i) = M(t_i,t_0)(\mathbf{w}^b + \delta\mathbf{w}) - M(t_i,t_0)(\mathbf{w}^b), \tag{28}$$

while the linear perturbation is given by

$$\delta\mathbf{w}^{L}(t_i) = \mathbf{M}(t_i,t_0)\,\delta\mathbf{w}. \tag{29}$$

Ideally, the initial perturbation $\delta\mathbf{w}$ should have structure and amplitude typical of background errors. The actual background errors are not known, however, so in order to apply this test a suitable proxy must be defined. In meteorology, it is commonly assumed that the background errors can be roughly approximated from differences in model forecasts initiated at different time lags (Rabier *et al.* 1998). The forecasts will differ because the shorter term forecast will be initiated from an analysis containing data assimilated between lags. Here we

---

[4]It is worth remarking that the FGAT version of 3D-Var is not independent of outer loops even when $H_i$ is linear since updating the reference state trajectory would lead to a modified effective observation vector (the second term in (40)). Introducing these outer loops, however, lead to a divergence of the cost function, for reasons which at present remain unclear.

consider a similar approach in which an initial perturbation is derived from the difference between two model states obtained from free integrations of the model having different initial states. One of the initial states is taken to be the *analysis* state ($\mathbf{w}^a$) at the *end* of a 4D-Var assimilation interval (as defined by (19)), while the other initial state is taken to be the background state ($\mathbf{w}^b$) valid at the same time (see Fig. 1b). In the first example presented below, $\mathbf{w}^a$ and $\mathbf{w}^b$ are taken from the end of the second 30-day cycle (on 01 March 1993) of EX4D, with $\delta\mathbf{w} = \mathbf{w}^a - \mathbf{w}^b$ defining the initial perturbation in (28) and (29). The validity of the linear model was also investigated for other types of perturbations (analysis increments, differences between analysed states at two different dates) and for other starting dates, and the results were qualitatively similar to those discussed below.

A meridional-vertical section of the perturbation temperature at $110°$W is shown in Fig. 4a. The field is characterized by large perturbations of up to $4°$C, appearing as a result of the temperature observations which are assimilated during the second cycle. The perturbations after 10 and 30 days (the widths of the 3D- and 4D-Var windows) of integration in the nonlinear model are shown in Figs. 4b and c, respectively. Figure 4b allows us to check the assumption in 3D-Var that perturbations evolve slowly over 10 days. The large-amplitude positive anomaly near $12°$N and the smaller amplitude negative anomalies near $7°$S and $16°$N are indeed well approximated by the 10-day persistence model (cf. Figs. 4a and b). The persistence assumption breaks down nearer the equator where the oceanic dynamical response is much more rapid. In the persistence model, the positive anomaly at $4°$N is largely overestimated, while the negative anomaly at $7°$N is largely underestimated. In contrast, Figs. 4c and d illustrate that the TL model is able to provide a good description of the perturbation in the equatorial waveguide at least 30 days ahead. The similarity of Figs. 4c and d may come as little surprise since it is well known that the large spatial scale, low frequency response of the tropical oceans involves predominantly linear wave dynamics (Philander 1989).

At smaller spatial and temporal scales ($< 1000$km, $< 1$ month), energetic motions in the central and eastern equatorial Pacific are dominated by tropical instability waves (TIWs) (Legeckis 1977). Because of the importance of nonlinear processes in ultimately limiting the growth of unstable waves, it is interesting to see if some of the differences between perturbations in the TL and nonlinear models can be linked to TIWs. TIWs are most energetic during the autumn months. If TIW activity is indeed a limiting factor of the TL approximation then one would expect this approximation to be less valid during this time. To check this, the above experiment was repeated using a starting date of 27 September 1993 and a temperature perturbation defined as the difference between the 4D-Var analysis and background state at that time (i.e., at the end of the ninth 30-day cycle of EX4D). A zonal-vertical section of the initial temperature perturbation at $4°$N is shown in Fig. 5a. Figures 5b and c show the nonlinear and TL model-predicted temperature perturbations after 30 days, while Fig. 5d shows their difference. West of $160°$W, the TL approximation holds quite well. Most of the nonlinear behaviour is located in the upper thermocline in the eastern and central Pacific, which is the area of largest thermal signal from TIWs. The differences between the nonlinear and linear perturbations are mostly associated with larger amplitudes of the linear perturbation. This confirms that nonlinear mechanisms play an important role in limiting the amplitude of the TIWs, and that the TL approximation is limited at their spatial scale. Over longer integration periods, the TIWs show up clearly as the dominant error signal (not shown), with the amplitude of the perturbations tending to be greatly overestimated in the TL model. This limitation is, however, only present at spatial scales of order 1000km and during the active TIW season.

Strongly nonlinear processes associated with vertical mixing and convection are another factor contributing to the limitation of the TL approximation, particularly in the small vertical scales. For example, when a perturbation leads to a statically unstable water column in the nonlinear model, the water column will be mixed instantaneously as a result of enhanced vertical diffusion. This process will effectively reduce the amplitude of the perturbation in the nonlinear model. In the TL model, on the other hand, there is no linearized counterpart of this process and the perturbation will remain unchanged. This could explain why the perturbations in the mixed-layer, where vertical mixing is strongest, are larger in the TL model (Fig. 5c) than in the nonlinear model (Fig 5b).

Further illustration of the previous points is provided in Fig. 6 which displays the time evolution of the correlation and root-mean-square (rms) difference between the temperature perturbations in the nonlinear and TL models. The correlation is above 0.8 during the first three months in both experiments with different starting dates (Fig. 6a), which indicates that the spatial patterns are in broad agreement. In contrast, in both experiments, the rms difference experiences a rather quick growth during the first 20 days (Fig. 6b) and then tapers off during the next three months. This initial error growth is associated with small-scale processes. For the experiment starting in March, this growth is primarily associated with vertical mixing processes, whereas for the experiment starting in October, it is caused by the combined effects of TIWs and vertical mixing. In particular, it can be noted that the absence of nonlinear effects results in an overestimated amplitude of the perturbation during the TIW-active season.

Figure 6b gives a rather pessimistic view of the validity of the TL approximation. However, if we focus on the large-scale component of the perturbation, the TL model actually provides a very good description of the perturbation evolution over several months. To illustrate this point, the correlation and rms statistics have been recomputed using low-pass filtered versions of the perturbations, $\mathbf{L}\delta\mathbf{w}^{L}(t_i)$ and $\mathbf{L}\delta\mathbf{w}^{NL}(t_i)$, where $\mathbf{L}$ is a close variant of the 3D Laplacian filter used in the correlation model of $\mathbf{B}$ (see section 3.3). The "large-scale" component of the perturbation has been isolated by setting the zonal, meridional and vertical length scales in $\mathbf{L}$ to 400km, 200km and 20m, respectively. Figures 6c and d show that the correlation now remains above 0.85 for the entire six-month period and that the rms difference is small compared to the rms of the nonlinear perturbation over at least four months.

In summary, the results from this section indicate that the 10-day persistence model used in 3D-Var is adequate for describing large-scale perturbations in off-equatorial regions but has some limitations closer to the equator where the dynamical adjustment time scales are shorter. In comparison, the 30-day TL model provides a good description of large-scale perturbations in both off-equatorial and equatorial regions. Smaller scale, regionally-confined structures associated with TIWs, however, are more problematic and our experiments suggest that they are possibly the main source of error in the TL integration. Vertical mixing and convective processes also tend to limit the accuracy of the TL model in the small vertical scales. Further research is required to determine whether the accuracy of the TL model can be improved using a more sophisticated parametrisation of vertical diffusion, in particular one which accounts for (nonzero) perturbations in the vertical mixing coefficients. However, it will be shown in section 5.2 that these limitations on the validity of the TL model are much less severe than appears at first sight and that in fact a very good fit to the data is possible.

## 4.3   Convergence properties

Each 10-day 3D-Var cycle required roughly 25 minutes of CPU time on the Fujitsu VPP700, while each 30-day 4D-Var cycle required roughly 5 hours of CPU time (i.e., a factor four more costly than 3D-Var). Figures 7a and b show an example, taken here from the second cycle of EX3D, of $J$ and the norm of $\nabla_{\mathbf{v}}J$ as a function of the number of minimization iterations. The convergence of the minimization in 3D-Var was relatively quick, requiring on average less than 25 iterations to reach the effective minimum of $J$. Figures 8a and b (solid curves) show the same quantities from the second cycle of EX4D. The convergence of the minimization in 4D-Var was generally slower than in 3D-Var. After the final (60th) iteration, the reduction of the norm of $\nabla_{\mathbf{v}}J$ relative to its initial value was typically between three and four orders of magnitude compared to over six orders of magnitude in 3D-Var.

The jumps in the solid curves in Figs. 8a and b occur after an outer iteration when the reference trajectory is reinitialized (here every 10 iterations). To illustrate the value of these outer iterations, the 4D-Var minimization on this particular cycle has been repeated with only one outer iteration (i.e., 60 minimization iterations with no trajectory updates). The dashed curves in Figs. 8a and b correspond to this sensitivity experiment. Figure 8b illustrates that, relative to the initial gradient norm, convergence is more efficient without than with outer iterations, with a gain of approximately an order of magnitude in the reduction of the gradient norm. On the

other hand, the reduction of the cost function in the experiment performed without outer iterations saturates at a level above the cost function with outer iterations. One has to be careful, however, in making direct comparisons between these two curves since, after the first outer iteration, the cost functions are no longer the same in the two experiments. It is more instructive to compare the final value of the full (nonapproximated) cost function $J^F$ (Eq. (7)) for each experiment. These values are plotted on Fig. 8a with an asterix (plus) symbol for the experiment with (without) outer iterations (for clarity the symbols have been displaced slightly to the left of the right border). This figure provides a clear indication of the positive impact of the outer iterations. The final value of $J^F$ with outer iterations is about half that without outer iterations. Furthermore, it is very close to the final value obtained with the approximated (quadratic) cost function (solid curve) and thus provides a good measure of the consistency of the incremental approach. In the absence of outer iterations, however, this consistency is lost as illustrated by the large discrepancy between the final value of $J^F$ and that of the approximated cost function $J$ (dashed curve).

In 3D-Var, 60 iterations was more than double the number actually needed to reach an acceptable level of convergence. With only 25 iterations, for example, the computational cost of 3D-Var could be reduced by a factor of 1.8 without degrading the quality of the analysis. Despite this potential to economize in 3D-Var, 60 iterations were retained simply to be consistent with the total number of iterations used in 4D-Var. In 4D-Var, convergence was slower but still reasonably efficient. Preconditioning techniques such as those described in Fisher and Andersson (2001) offer considerable scope for further improving the minimization efficiency. The outer iterations were clearly shown to be an essential feature of the algorithm. At present, however, it is not clear how many outer iterations are needed for the solution of the incremental problem to be a good approximation to the solution of the full problem. It is also not clear what combination of outer and inner iterations gives the best convergence rate. These issues are a matter for further research.

## 4.4  Optimality properties

The formulation of the variational assimilation problem relies on a number of hypotheses on the statistics of the background and observation errors. The validity of these hypotheses is an important factor in determining the optimality of the analysis. One particularly simple diagnostic that can be used to check whether the statistics of $\mathbf{B}$ and $\mathbf{R}$ are consistent with the innovation vector is the value of the cost function at its minimum ($J_{min}$) which, for a linear system, should, on statistical average, be equal to $p/2$ where $p$ is the total number of assimilated observations (Tarantola 1987; Talagrand 1999; Bennett *et al.* 2000). This is easily verified by substituting the minimizing solution (12) into (10) to yield an expression for $J_{min}$ in terms of the innovation vector $\mathbf{d}$;

$$J_{min} = \frac{1}{2} \mathbf{d}^T \left( \mathbf{GBG}^T + \mathbf{R} \right)^{-1} \mathbf{d}. \tag{30}$$

Under the linear approximation, the covariance matrix of $\mathbf{d}$ is $E[\mathbf{dd}^T] = \mathbf{GBG}^T + \mathbf{R}$ where $E[\ ]$ denotes mathematical expectation. It then follows from taking the expectation of (30) and using the identity $\mathbf{d}^T \mathbf{Pd} = \text{trace} \left( \mathbf{Pdd}^T \right)$, for any matrix $\mathbf{P}$, that $E[J_{min}] = \frac{1}{2} \text{trace} \left( \mathbf{I}_p \right) = p/2$. If we assume further that the background and observation errors are Gaussian then it can be shown (e.g., see section 4.3.6 in Tarantola 1987) that the expected variance of $J_{min}$ is $\sigma^2_{J_{min}} = E[(J_{min} - E[J_{min}])^2] = p/2$. Therefore, providing $\mathbf{B}$ and $\mathbf{R}$ are correctly specified and that the system is quasi-linear, the value of $J_{min}$ on each assimilation cycle should be $p/2$ within a standard deviation of $\sqrt{p/2}$.

In order to compare the actual values of $J_{min}$ with its expected value, it is more convenient to consider the normalized quantity $\gamma = 2J_{min}/p$ for which $E[\gamma] = 1$ and $\sigma^2_\gamma = E[(\gamma - E[\gamma])^2] = 2/p$. $\sigma^2_\gamma$ scales with the inverse of $p$ so will be small when a large number of observations are assimilated. Figures 9a and b (dotted curves) show the actual values of $\gamma$ as a function of the assimilation cycle in EX3D and EX4D. The expected value of $\gamma = 1$ (solid line) is also plotted together with the expected error bars (dashed lines) at $1 \pm \sigma_\gamma$. The average of the actual values of $\gamma$ over all cycles in EX3D is very close to its expected value of one ($\bar{\gamma} = 0.97$ where the

overbar denotes cycle average) but in EX4D is somewhat too small ($\overline{\gamma} = 0.73$). On average, the actual values of $\gamma$ exceed its expected value by $8\sigma_\gamma$ in EX3D and $29\sigma_\gamma$ in EX4D. The expected error bars are slightly larger in EX3D than in EX4D since there were fewer observations assimilated during a 10-day 3D-Var cycle than during a 30-day 4D-Var cycle (roughly 10000 observations were available every 10 days). Even so, the actual values of $\gamma$ nearly always greatly exceed the expected error bounds in both experiments.

From (30) it is clear that the value of $J_{min}$ (or $\gamma$) may be decreased (increased) if the variances of either **B** or **R** are increased (decreased). The lower than expected value of $\gamma$ in EX4D therefore could be a sign that either the background- or observation-error variances have been overestimated. Our prior estimate of the observation-error variances is very crude and in particular takes no account of possible representativeness error. For example, the value of $0.5^\circ$C used for the standard error of TAO data is only slightly larger than the documented estimate of TAO observation error which accounts only for the instrumental component of that error (McCarty *et al.* 1997). The specified observation-error variances are thus probably underestimated and therefore acting to increase the value of $\gamma$. This effect is clearly demonstrated by the dashed-dotted curve in Fig.9a which shows the actual values of $\gamma$ from a 3D-Var experiment in which the standard error for TAO data was increased to $1.0^\circ$C. This lead to nearly a factor of two decrease in the cycle average of $\gamma$ ($\overline{\gamma} = 0.52$).

It is more likely that the background-error variances, which have been specified from the climatology of a model integration performed without data assimilation, are substantially overestimated. Whereas this specification might yield a reasonable estimate of the background errors for the first cycle, it is probably too large an estimate in later cycles, particularly in well-observed regions, where the data assimilated in previous cycles have acted to reduce the innovation vector. Generally speaking, however, it is safer to overestimate than underestimate the background-error variances to prevent the model from drifting too far from observations. It should be noted that a misspecification of the background- and/or observation-error correlations could also change the value of $\gamma$.

Another interesting feature in Fig. 9 is the rather large variance in $\gamma$ between cycles. This is an indication that, contrary to what has been assumed, the background-error covariances are not stationary, in addition to being largely overestimated as already mentioned. From Fig. 9a, we see that the variability of $\gamma$ is larger in EX3D than in the sensitivity experiment where the standard error used for TAO data was larger. This is understandable since the smaller standard error for TAO in EX3D means that $\gamma$ will be more sensitive to the true variations in the background-error covariances between cycles.

While the $J_{min}$ statistic gives some useful insight into the optimality properties of the system, it is not possible based on this information alone to correct unambiguously any misspecification of the background- and/or observation-error covariances. If the actual value of $J_{min}$ is not equal to $p/2$ then this can be rectified simply by muliplying **B** and **R** by the factor $\gamma = 2J_{min}/p$. This procedure will change the *absolute* values of the background-, observation- and analysis-error variances, but will have no influence on the analysis increment itself (e.g., as evident from the expression for the analysis increment in (12)). What is important then is the *relative* magnitude of the variances in **B** and **R** (the absolute values can be obtained by post-multiplication by $\gamma$). Adaptive procedures can be used to tune the variances in **B** and **R** using information on the mismatch between the expected and actual values of *sub-parts* of the cost function at its minimum (Wahba *et al.* 1995; Desroziers and Ivanov 2001). To compute the expected minimum value of sub-parts of the cost function is more complicated but practical methods do exist (Bennett *et al.* 2000; Desroziers and Ivanov 2001). We have not attempted to apply any of these methods in the present study but they do offer an interesting possibility for improving the variance estimates in the future.

## 4.5 Flow-dependent background-error variances

It is well known that, in the limit of a perfect, linear model, variational assimilation is equivalent to the Kalman filter in that, given identical input parameters, they produce the same analysis at the end of the assimilation

window (e.g., see Courtier *et al.* 1994). Consider an assimilation window $t_0 \le t_i \le t_n$ in which a background state $\mathbf{w}^b$, with error-covariance matrix $\mathbf{B}$, is available at the beginning of the assimilation window and an observation vector $\mathbf{y}_n^o$, with error-covariance matrix $\mathbf{R}_n$, is available at the *end* of the window. Within the linear approximation, the error-covariance matrix $\mathbf{P}^b(t_n)$ for the background state $\mathbf{w}^b(t_n) = M(t_n, t_0)(\mathbf{w}^b)$ is obtained by evolving $\mathbf{B}$ using the linear model and its adjoint:

$$\mathbf{P}^b(t_n) = \mathbf{M}(t_n, t_0)\,\mathbf{B}\,\mathbf{M}(t_n, t_0)^T \tag{31}$$

where $\mathbf{P}^b(t_0) = \mathbf{B}$. In an extended Kalman filter, (31) would be used explicitly to transport the covariances forward in time. In incremental variational assimilation, on the other hand, this propagation is implicit in the global minimization process. For the example above, the variational analysis increment at $t_0$ is given by (12) with $\mathbf{G} = \mathbf{H}_n \mathbf{M}(t_n, t_0)$, $\mathbf{d} = \mathbf{y}_n^o - H_n(\mathbf{w}^b(t_n))$, and $\mathbf{R} = \mathbf{R}_n$:

$$\delta\mathbf{w}^a = \mathbf{B}\,\mathbf{M}(t_n, t_0)^T\,\mathbf{H}_n^T \left(\mathbf{H}_n\,\mathbf{M}(t_n, t_0)\,\mathbf{B}\,\mathbf{M}(t_n, t_0)^T\,\mathbf{H}_n^T + \mathbf{R}\right)^{-1}\mathbf{d}. \tag{32}$$

The analysis increment at $t_n$ can be obtained by applying $\mathbf{M}(t_n, t_0)$ to both sides of (32) to yield, after inserting (31),

$$\delta\mathbf{w}^a(t_n) = \mathbf{P}^b(t_n)\mathbf{H}_n^T \left(\mathbf{H}_n\mathbf{P}^b(t_n)\mathbf{H}_n^T + \mathbf{R}\right)^{-1}\mathbf{d} \tag{33}$$

where $\delta\mathbf{w}^a(t_n) = \mathbf{M}(t_n, t_0)\delta\mathbf{w}^a$. Equation (33) is the standard analysis step of an extended Kalman filter, which weights the background state at $t_n$ using an error-covariance matrix predicted by (31).

The FGAT version of 3D-Var can be viewed as a limiting case in which $\mathbf{M}$ is taken to be the identity matrix. This implies that $\mathbf{P}^b(t_n) = \mathbf{B}$; i.e., that the background-error covariances at the end of the window (and at all intermediate times) are identical to those specified at initial time. In incremental 4D-Var, on the other hand, $\mathbf{M}$ is the TL operator so that $\mathbf{P}^b(t_n)$ will be modified by dynamical processes acting within the window. In this section, we focus on how the TL dynamics act to modify the prior estimates of the background-error *variances* (the diagonal elements of $\mathbf{P}^b(t_n)$). The TL dynamics will also modify the background-error correlations but a discussion of this feature is beyond the scope of the present paper.

Single observation experiments provide a practical way of computing the effective background-error variances used implicitly in 4D-Var (Thépaut *et al.* 1993; Thépaut *et al.* 1996). For a single observation, $d = \mathbf{d}$ and $(\sigma^o)^2 = \mathbf{R}$ become scalars, and $\mathbf{h}^T = \mathbf{H}_n$ becomes a vector of the same length as $\mathbf{w}$. The error variance of the background equivalent of the observation is then given by the scalar product $(\sigma_n^b)^2 = \mathbf{h}^T\mathbf{P}^b(t_n)\mathbf{h}$. If we assume further that the observation is of one of the model state variables and that its location coincides with a model grid-point then $\mathbf{h}^T = (0, ..., 0, 1, 0, ...0)$, where the entry equal to one corresponds to that grid-point, and $(\sigma_n^b)^2$ becomes an element of the diagonal of $\mathbf{P}^b(t_n)$. It is straightforward to deduce $(\sigma_n^b)^2$ by applying $\mathbf{h}^T$ to both sides of (33):

$$\mathbf{h}^T\delta\mathbf{w}^a(t_n) = (\sigma_n^b)^2 \left(\frac{d}{(\sigma_n^b)^2 + (\sigma^o)^2}\right) \tag{34}$$

which can be rearranged to give

$$(\sigma_n^b)^2 = \left(\frac{\mathbf{h}^T\delta\mathbf{w}^a(t_n)}{d - \mathbf{h}^T\delta\mathbf{w}^a(t_n)}\right)(\sigma^o)^2. \tag{35}$$

The term $\mathbf{h}^T\delta\mathbf{w}^a(t_n)$ is the value of the analysis increment at the time and grid-point location of the single observation. Equation (35) thus provides the basis of an algorithm for systematically diagnosing the diagonal elements of $\mathbf{P}^b(t_n)$.

Figure 10 shows vertical profiles of the background-error standard deviations ($\sigma_n^b$) for temperature at three different latitudes (equator, 5°N and 15°N) in the central Pacific (140°W). The dashed-dotted curves are the prior

estimates of $\sigma_n^b$ which, as discussed earlier, were computed from a control experiment without data assimilation. In 3D-Var, the prior estimates are effectively used to weight the background state at all times within the assimilation window, while in 4D-Var they are used for weighting the background state at the *beginning* of the assimilation window. The prior estimates display maxima around the depth of the climatological thermocline where variability is greatest (around 170 m at the equator and $5^\circ$N, 150 m at $15^\circ$N). The solid curves show the profile of the effective $\sigma_n^b$ used in 4D-Var at the end of the second 30-day cycle (03 March 1993) of EX4D (see section 5 for a thorough description of this experiment). Panels a–c show that the flow-dependency in the $\sigma_n^b$ estimates is greatest near the equator, which is not surprising since dynamical effects have shorter time-scales there. In 30 days, the ocean state can change significantly at the equator but much less at $15^\circ$N because eddies are not resolved in this low resolution OGCM. Panels a–c also show that the TL dynamics tend to homogenise and reduce the $\sigma_n^b$ in the ocean mixed-layer, particularly in the upper 70m.

The TL dynamics also tend to move the level of maximum background-error variance to the level of the thermocline, as illustrated by comparing panels a–c with corresponding profiles of $|\partial T_b/\partial z|$ computed from the 30-day averaged background temperature state on the second cycle. This tendency is physically sensible since the level of maximum variability of the thermal field, and thus of maximum likely error in the background state, is located at the level of the thermocline. It can also be noted that the TL dynamics can substantially increase the maximum value of the background-error variance near the equator. This is related to the fact that the background trajectory in this experiment has already felt the influence of observations assimilated during the previous cycle through a tightening of the thermocline. This tighter, well-defined thermocline, relative to that of the control, leads to larger thermal signals and thus to an increase in the maximum value of $\sigma_n^b$ by the TL dynamics. In some 3D assimilation systems (e.g., Behringer *et al.* 1998; Alves *et al.* 1998), the background-error variances have been parametrized by making them dependent on the vertical gradient of the background temperature field. Figure 10 suggests that relating $\sigma^b$ to the background temperature gradient is dynamically sensible. Such a weighting could also be useful in 3D- and 4D-Var by introducing a flow-dependence in the variances of **B** at the beginning of the window.

## 4.6    Fit to the observations

Statistics derived from the background-minus-observation vector (BmO $\equiv H_i(\mathbf{w}^b(t_i)) - \mathbf{y}_i^o$) and analysis-minus-observation vector (AmO $\equiv H_i(\mathbf{w}^a(t_i)) - \mathbf{y}_i^o$) can yield useful information about the internal consistency of the data assimilation system (Hollingsworth and Lönnberg 1989). Figures 11b and c show the 1993-98 averaged statistics of the BmO and AmO as a function of depth for all the assimilated TAO data in EX3D and EX4D. For reference, the average statistics of the difference between the control and TAO data are also shown, which for convenience will be referred to as the BmO of EXCL. In panel b the BmO curve of EXCL displays a large warm bias of about $2^\circ$C just below the thermocline (cf. with the average of the TAO data profile shown in panel a). This bias is largely reduced in EX3D, the maximum of the averaged BmO and AmO being about $0.3^\circ$C at 50m. The bias is almost completely absent from EX4D: the average of AmO is very small, except at 250m where the analysis is about $0.1^\circ$C too cold.

In panel c the rms of BmO of EXCL shows large differences both just below the thermocline, where there are large biases, and in the thermocline, where signals associated with the seasonal cycle and interannual variability are largest. These differences are substantially reduced in EX3D and EX4D. The rms of BmO in EX4D is similar to that of EX3D, with a maximum around $1.5^\circ$C at the level of the thermocline. On the other hand, the rms of AmO in EX4D is very much reduced, being less than $0.5^\circ$C over the entire water column, compared to the rms of AmO in EX3D which is hardly smaller than that of BmO. The fit to the TAO data in EX4D is thus within the specified level of observation error ($0.5^\circ$C), which is not the case in EX3D. The larger AmO in EX3D is primarily an artifact of the gradual way the analysis increment is applied to the model. While minimizing nonphysical adjustment processes, this procedure ultimately degrades the fit to the data achieved by the linear analysis $\mathbf{w}^b(t_i) + \delta\mathbf{w}^a(t_i)$.

Figure 11 provided a time-averaged view of the BmO and AmO statistics for the assimilated TAO data. Figure 12 now provides a view of how these statistics change with time during the 1993-98 analysis period. On the first assimilation cycle, the background is provided by the control and as a result the BmO is very large (Fig. 12c). After the first assimilation cycle, however, the properties observed in Fig. 11 begin to emerge: the average of AmO is small in both EX3D and EX4D, and the rms of AmO is equal to about $1^\circ$C in EX3D and $0.5^\circ$C in EX4D. It is worth noting that, in both EX3D and EX4D, the statistics of BmO and AmO are approximately stationary, and in particular do not seem to exhibit any obvious dependence on either the number of assimilated observations (Fig. 12a) or interannual variability (Fig. 12b).

The cycle-average of the temporal evolution of BmO and AmO *within* the assimilation window is shown in Fig. 13. For the background, which is not constrained by observations, the fit to the data degrades with time. After 10 days in EX3D and 30 days in EX4D, the rms of BmO increases by $0.2^\circ$C and $0.5^\circ$C from initial values of $1.0^\circ$C and $0.6^\circ$C, respectively. The rms of BmO at the end of the window is $1.2^\circ$C in both experiments, compared to $1.9^\circ$C in EXCL. In both EX3D and EX4D, the fit of the analysis to the data is uniform over their respective assimilation windows, apart from a very slight increase of the AmO at the window boundaries in EX4D. When model error is important, and not explicitly accounted for in the assimilation method, it often manifests itself as a U-shape in the fit to the data (Ménard and Daley 1996). Any signal of model error, however, is more likely to be visible in the $J_o$ residual ($\mathbf{H}_i \delta \mathbf{w}^a(t_i) - \mathbf{d}_i$) than in the AmO since the residual is the quantity that is minimized objectively. The residual will contain information about linearization errors introduced by the approximation (3) as well as errors in the nonlinear model itself.

Figure 14 shows the cycle-average of the $J_o$ residuals in EX3D and EX4D. For EX3D, the U-shape is evident, though quite weak, with a difference of about $0.2^\circ$C between the highest point at the window boundaries and the lowest point in the middle of the window. If this is indeed a sign of model error then it would be consistent with the results of section 4.2 which illustrated that the persistence model did have some limitations near the equator. In contrast, in EX4D, the residuals are nearly flat over the whole window width and are very similar to the AmO in Fig. 13. This result then suggests that model error is not a significant problem over the length of the 30-day window used in 4D-Var. Furthermore, the similarity between the residuals and AmO in EX4D is consistent with Fig. 8 of section 4.3 which showed that, after several outer loops, the full and incremental cost functions converged to similar values at the end of minimization. That result was demonstrated for a particular cycle (the second); Fig. 14 just confirms that this feature is consistent for all cycles of EX4D. Figure 14 also shows that the average of the residuals over the window width is consistent with the specified standard-error deviation of TAO data ($0.5^\circ$C) and is slightly smaller in EX4D than in EX3D. Therefore, the large AmO of EX3D compared to that of EX4D does not stem from a poorer fit to the data after minimization but rather from the manner in which the analysis increment is then applied in the nonlinear model. This point will be discussed further in section 5.2.
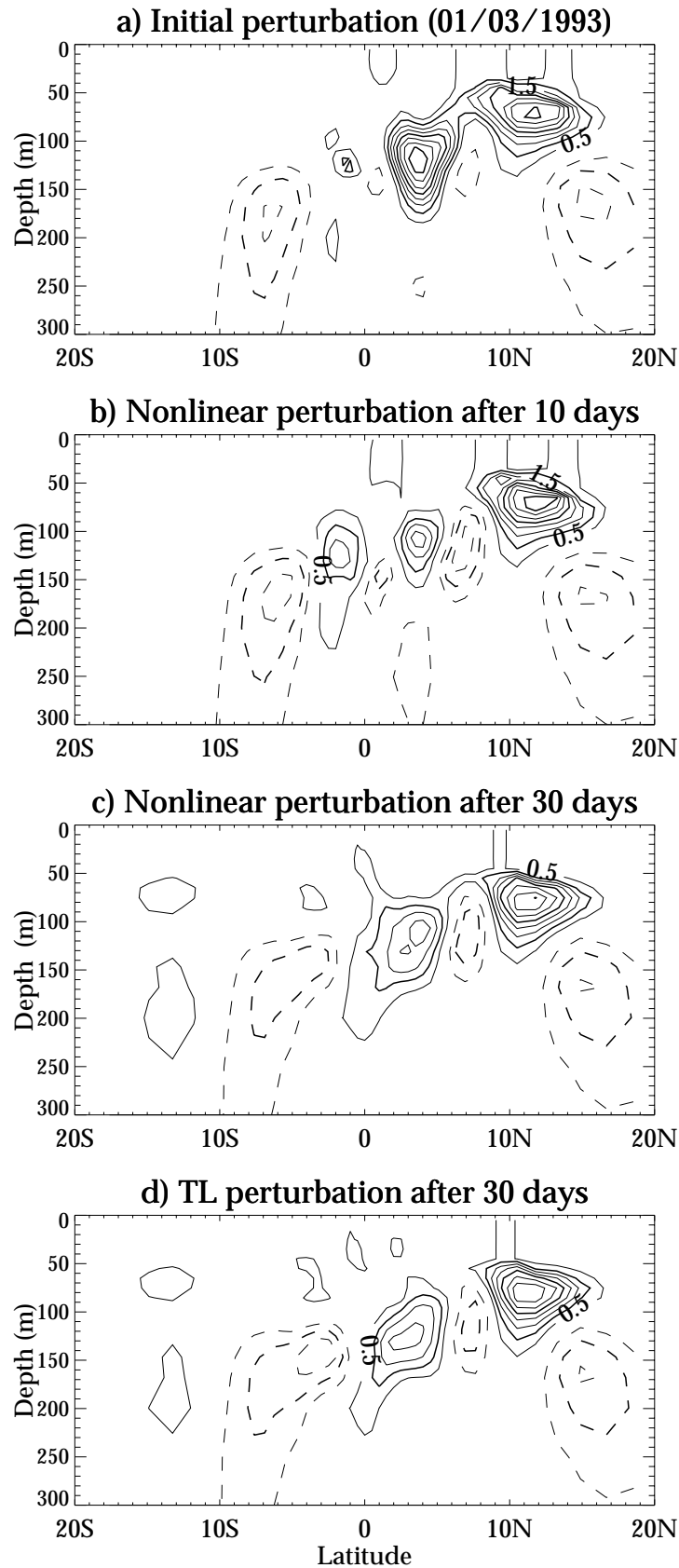
Figure 4: a) Meridional-vertical section at 110°W of a temperature perturbation defined as the difference between a 4D-Var analysis and the background state valid at the same time (01 March 1993). The perturbation after b) 10 days and c) 30 days evolution in the nonlinear model, and after d) 30 days evolution in the TL model. The contour interval is 0.5 °C.

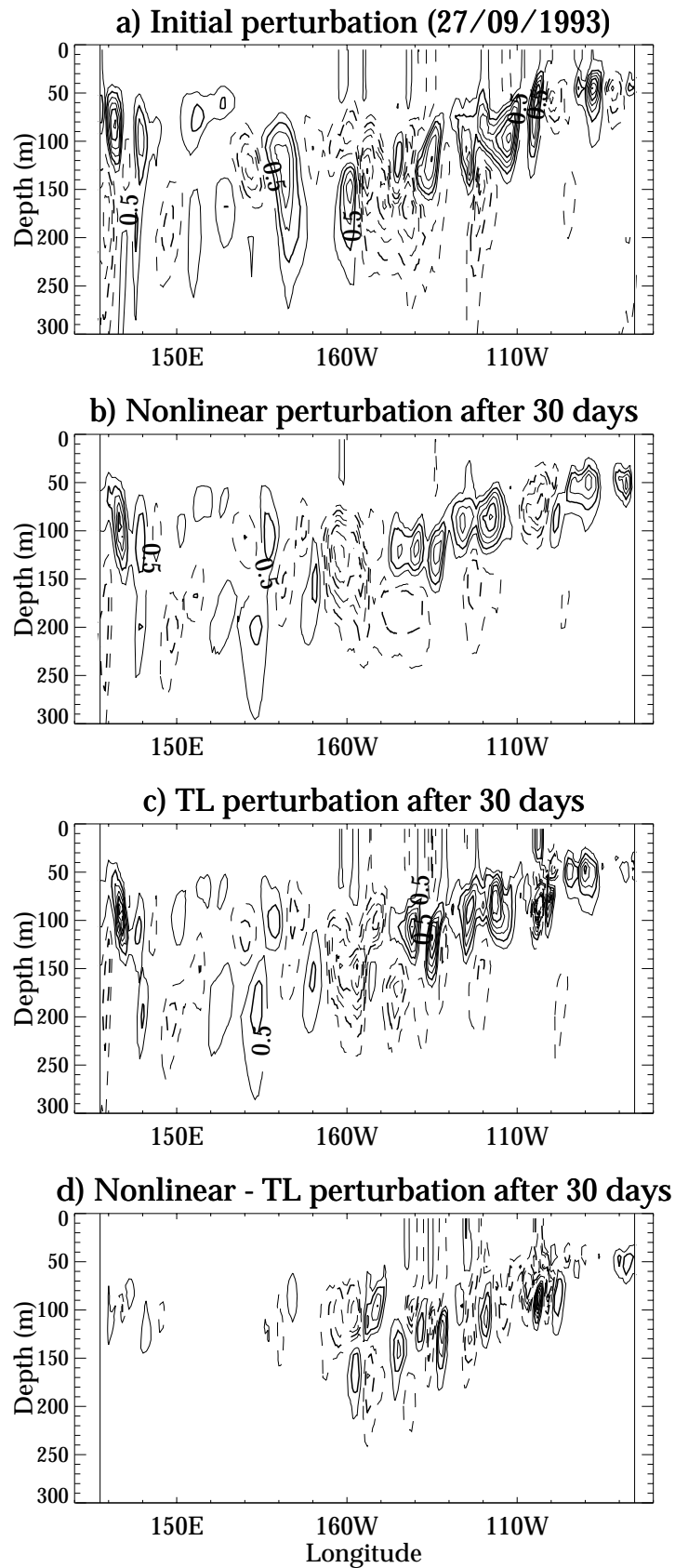## a) Initial perturbation (27/09/1993)

## b) Nonlinear perturbation after 30 days

## c) TL perturbation after 30 days

## d) Nonlinear - TL perturbation after 30 days

*Figure 5: a) Zonal-vertical section at 4°N of a temperature perturbation defined as the difference between the 4D-Var analysis and the corresponding background state on 27 September 1993. The perturbations after 30 days in the nonlinear model (panel b) and in the TL model (panel c). d) The difference between the perturbations in panels b and c. The contour interval is 0.5°C.*
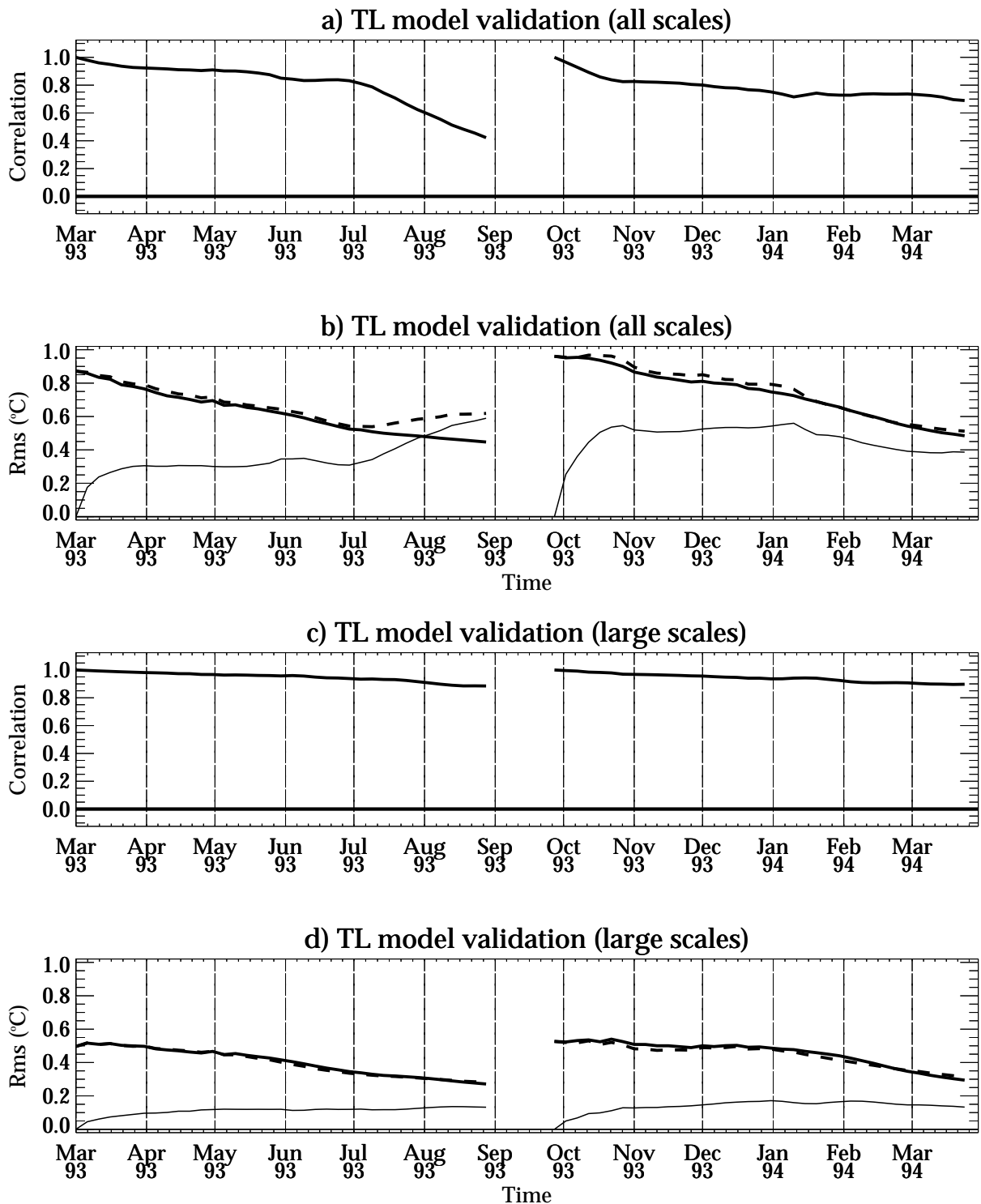
*Figure 6: Validation of the linear approximation for the TL model in the TAO region. a) The spatial correlation between the temperature perturbations in the linear and nonlinear models for two experiments starting in 01 March 1993 and at the end of 27 September 1993. b) The rms difference between the linear and nonlinear perturbations (thin curve) compared to the rms of the nonlinear (thick solid curve) and linear (thick dashed curve) perturbations. Panels c and d are analogous to panels a and b, respectively, but the statistics have been recomputed using a filtered version of the increment which retains only the large spatial scales (zonal scales longer than 400km, meridional scales longer than 200km, and vertical scales larger than 20m).*
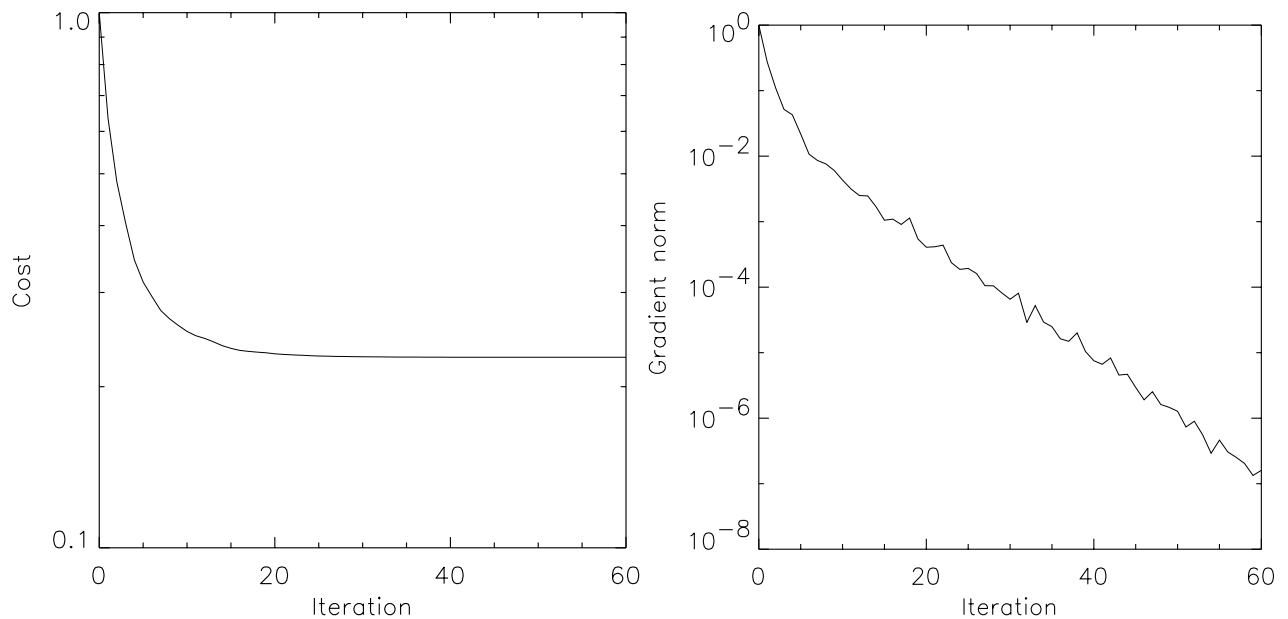
Figure 7: The value of a) the cost function ($J$) and b) the gradient norm $\sqrt{(\nabla_{\mathbf{v}}J)^T\nabla_{\mathbf{v}}J}$ as a function of the minimization iteration on the second cycle of EX3D. Both $J$ and $\sqrt{(\nabla_{\mathbf{v}}J)^T\nabla_{\mathbf{v}}J}$ have been normalized by their respective values at the start of minimization and plotted on a logarithmic vertical axis.
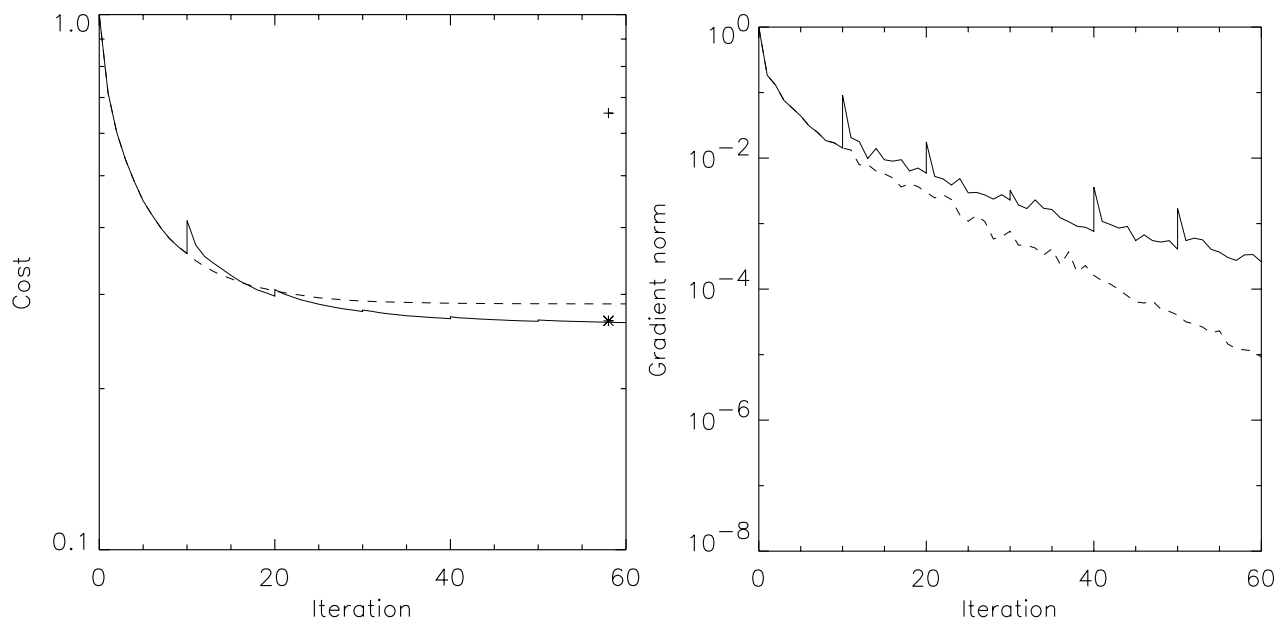


Figure 8: The value of a) the cost function ($J$) and b) the gradient norm $\sqrt{(\nabla_{\mathbf{v}}J)^T\nabla_{\mathbf{v}}J}$ as a function of the minimization iteration on the second cycle of EX4D (solid curve). As a sensitivity test, the second cycle of the 4D-Var experiment has been repeated with only one outer iteration (dashed curve), compared to five outer iterations used in the reference experiment. The plus (asterix) symbol in panel a indicates the final value of the nonapproximated cost function ( 7) for the experiment with one (five) outer iteration(s). Both $J$ and $\sqrt{(\nabla_{\mathbf{v}}J)^T\nabla_{\mathbf{v}}J}$ have been normalized by their respective values at the start of minimization and plotted on a logarithmic vertical axis.
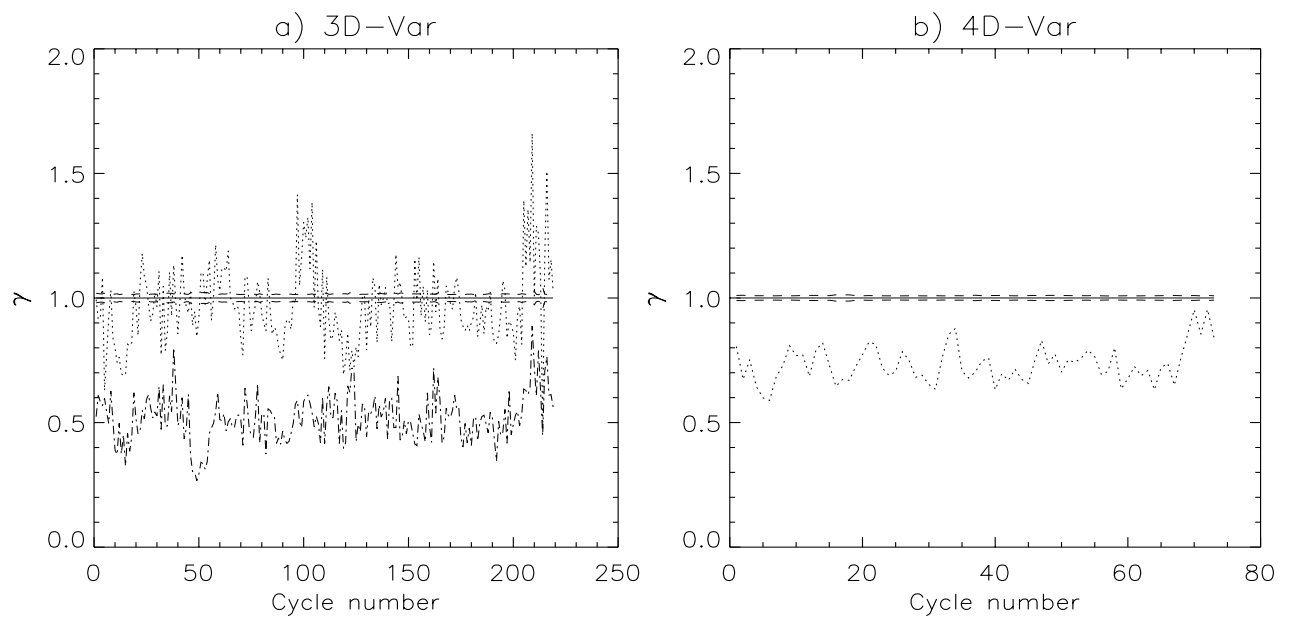
Figure 9: *The value of $\gamma = 2J_{min}/p$ plotted as a function of the assimilation cycle during the period 1993-98 in a) 3D-Var and b) 4D-Var. On each cycle, $J_{min}$ represents the value of the cost function at the end of the minimization and $p$ the total number of observations assimilated through the $J_o$ term. A total of 219 (73) 10-day (30-day) cycles were performed in 3D-Var (4D-Var). The* expected *value of $\gamma = 1$ (solid line) is plotted together with error bars (dashed lines) at $1 \pm \sigma_\gamma$ where $\sigma_\gamma = \sqrt{2/p}$ is the* expected *standard deviation of $\gamma$. The dotted curves in panels a and b correspond to the* actual *values of $\gamma$ computed on each cycle in the reference experiments EX3D and EX4D. The dashed-dotted curve in panel a corresponds to the* actual *values of $\gamma$ from a 3D-Var experiment in which the observation-error variance for TAO data is set to twice the value used in EX3D.*
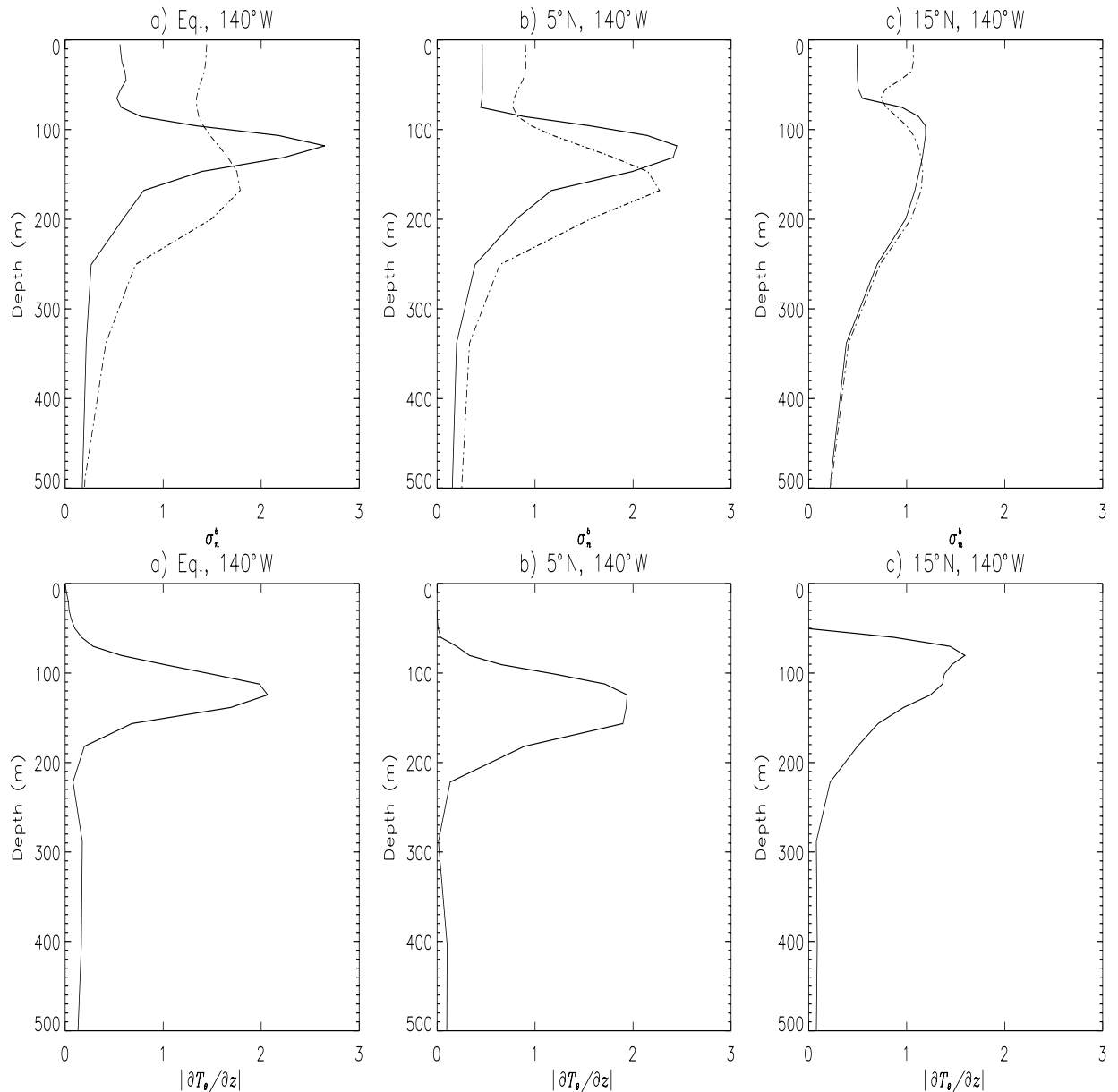
*Figure 10: Vertical profiles of the background-error standard deviations (in °C) used in 3D- and 4D-Var, at three different latitudes (a) equator, b) 5°N and c) 15°N) in the central Pacific (140°W). The dashed-dotted curves correspond to the standard deviations specified at the beginning of the assimilation window. In 3D-Var, these are also the effective standard deviations used at all future times within the window. The solid curves correspond to the effective standard deviations used in 4D-Var at the end of the 30-day window of the second cycle in EX4D Panels d–f show the corresponding profile of $|\partial T_\theta/\partial z|$ at each of these locations, computed from the 30-day mean of the background temperature state on the second cycle. The values of $|\partial T_\theta/\partial z|$ have been multiplied by a factor of ten in order to be plotted with the same horizontal scale as in panels a–c.*
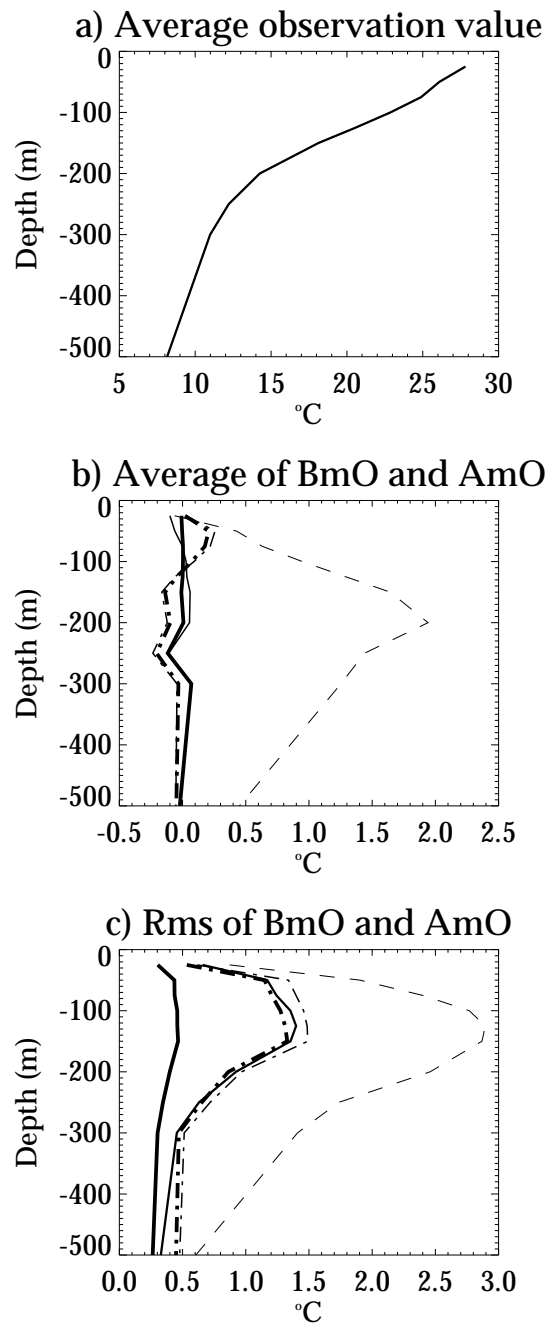
*Figure 11: Time-averaged statistics, plotted as a function of depth, of BmO and AmO for TAO data during the 1993-98 period. a) The average observation value; b) the average of BmO (thin curves) and AmO (thick curves); and c) the rms of BmO (thin curves) and AmO (thick curves). In panels b and c, the dashed curve corresponds to EXCL, the dashed-dotted curves to EX3D, and the solid curves to EX4D.*

## a) Number of observations in TAO region



## b) Average observation value



## c) Average of BmO and AmO
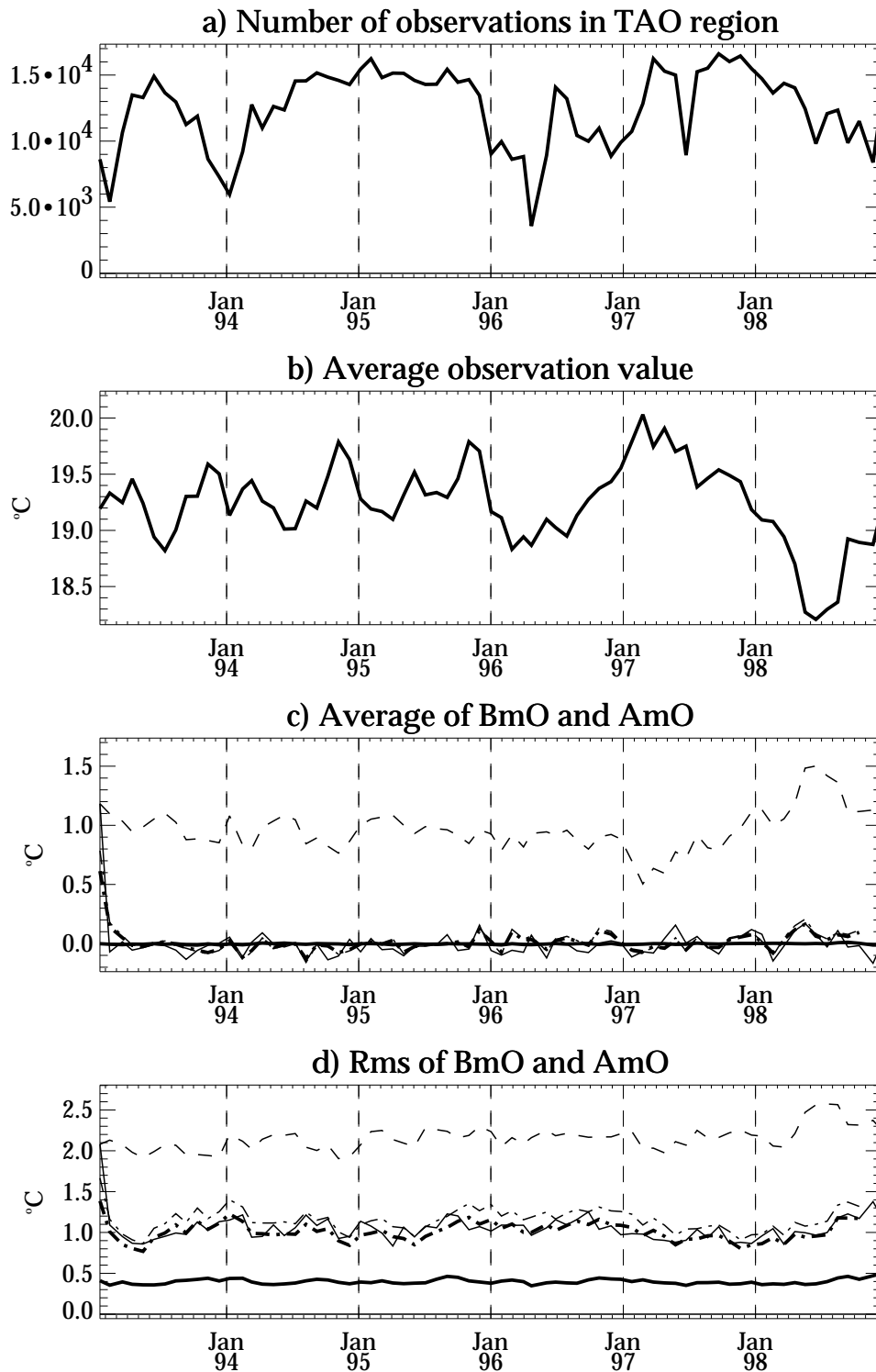


## d) Rms of BmO and AmO



*Figure 12: Spatially-averaged statistics, plotted as a function of the assimilation cycle, of BmO and AmO for TAO data during the 1993-98 period. a) The total number of TAO observations; b) the average observation value; c) the average of BmO (thin curves) and AmO (thick curves); and d) the rms of BmO (thin curves) and AmO (thick curves). In panels c and d, the dashed curve corresponds to EXCL, the dashed-dotted curves to EX3D, and the solid curves to EX4D. The statistics for EX3D are displayed as an average over three cycles (30 days) in order to be compared with those from EX4D.*
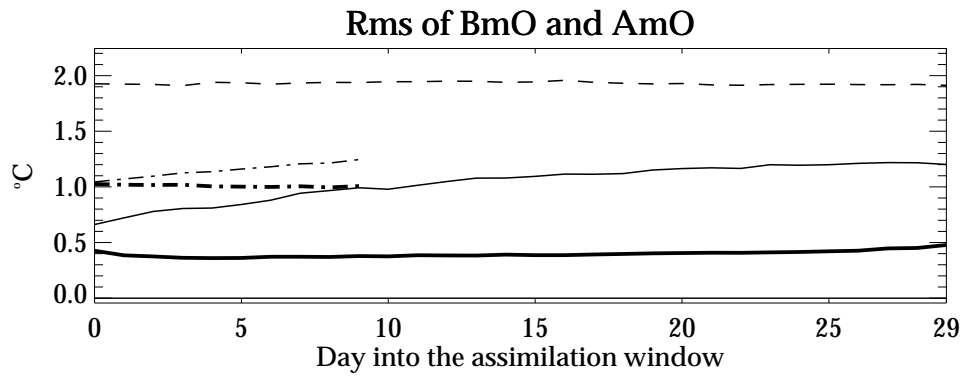
## Rms of BmO and AmO



*Figure 13: Rms of the 1993-98 cycle-average of BmO (thin curves) and AmO (thick curves) for TAO data plotted as a function of the day within the assimilation window. The dashed curve corresponds to EXCL, the dashed-dotted curves to EX3D, and the solid curves to EX4D.*
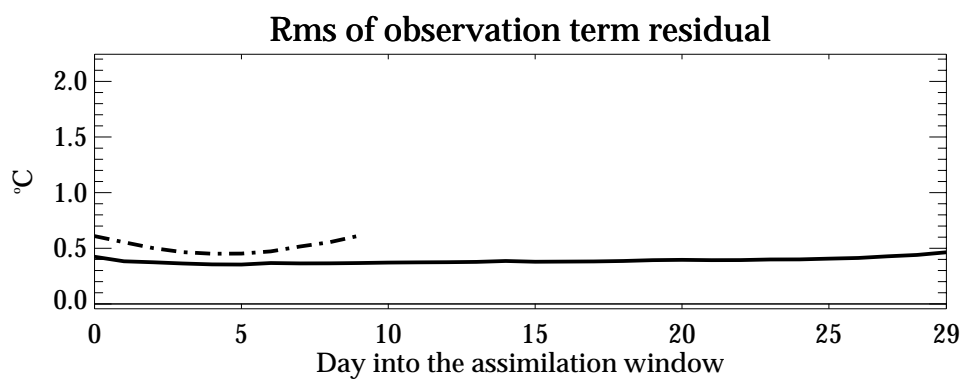
## Rms of observation term residual



*Figure 14: Rms of the 1993-98 cycle-average of the $J_o$ residual in EX3D (dashed-dotted curve) and EX4D (solid curve) for TAO data plotted as a function of the day within the assimilation window.*

# 5 Evaluation of 3D- and 4D-Var: climatological mean and variability of the analyses

In this section, the extended set of analyses (OI, 3D-Var, 4D-Var and control) is examined to assess the impact of the *in situ* data assimilation on the model's mean state (section 5.1) and variability (section 5.2). The different analyses are intercompared and validated against climatology and time-series from independent data sets.

## 5.1 Mean field

*Temperature analysis*

Vertical sections of the 1993-96 average temperature along the equator and at $140^{\circ}$W are shown in Figs. 15 and 16 for EXCL, EX3D and EX4D. In section 4.6 it was shown that the 4D-Var analysis (EX4D) is very close to observations in both an average and rms difference sense. The thermal field climatology from EX4D will thus be considered as our best estimate of the true thermal field climatology. As noted by Vialard *et al.* (2001), the thermocline structure in the control experiment (EXCL) is too diffuse compared to observations. To compensate for this problem, the assimilation of *in situ* temperature data, in both EX3D and EX4D, produces a large mean correction to the thermal field, which results in a colder thermocline with increased stratification. From the meridional section, it can also be seen that the tilt of the isotherms in the North-Equatorial Counter Current (NECC) region between $5^{\circ}$N and $10^{\circ}$N is considerably reinforced in both data assimilation experiments. The thermocline tightness and tilt is stronger in EX4D than in EX3D (cf. Figs. 16a and b near $7^{\circ}$N). This is consistent with the fact that, compared to 3D-Var, 4D-Var produces a closer fit to the assimilated data as seen in section 4.6.

Figure 17 shows the average profile and the standard deviation of the 4D-Var temperature analysis increment in the Nino3 ($150^{\circ}$W–$90^{\circ}$W, $5^{\circ}$S–$5^{\circ}$N) and Nino4 ($160^{\circ}$E–$150^{\circ}$W, $5^{\circ}$S–$5^{\circ}$N) regions. First, it can be noted that, while the mean thermal profiles in EX3D and EX4D are very similar, the assimilation increments used to produce them can be very different. Furthermore, the increments do not have an intuitive effect; e.g., they do not necessarily tend to warm the model in the region where the control experiment is too cold. This is particularly true for EX3D in Nino4, where the increments warm the deep ocean even though the control is too warm, and cool the upper ocean which is too cold in the control. In contrast, in both regions in EX4D, the analysis increment generally acts to systematically heat the upper part of the thermocline and cool its lower part, thus counteracting the tendency of the model to make the thermocline too diffuse. In Nino3, EX3D does not behave counter-intuitively as in Nino4, and cools rather strongly the thermocline in a region where the control had a tendency to be too warm. This point will be considered further later in this section.

Figures 15 and 16 provide a strong indication that the assimilation largely acts to correct for a bias in the model's subsurface temperature structure. One of the assumptions implicit in the present formulation of the assimilation problem is that the increment is unbiased. The long-term average of the temperature increment should be zero and the increment should therefore act to reduce random errors rather than systematic errors. It can be seen in Figs. 17b and d that, in both regions, the absolute value of the increment average is significantly smaller than its standard deviation, suggesting that the assumption that the increment is unbiased holds reasonably well in EX4D. In EX3D, however, this assumption seems to breakdown in Nino3, where the average of the increment reaches $-0.9^{\circ}$C at 75m depth compared to a standard deviation of $1.4^{\circ}$C. This is a large systematic increment, especially so when considering that increments are applied every 10 days in EX3D (thus corresponding to a -0.09$^{\circ}$C day$^{-1}$ systematic correction in EX3D compared to less than $0.01^{\circ}$C day$^{-1}$ in EX4D). As will be seen later, this strong systematic increment probably appears to counteract the effects of the spurious vertical downwelling that develops close to the equator in the eastern Pacific in EX3D. Finally, it can be noted that the standard deviation of the temperature corrections is largely concentrated at the level of the thermocline (around

160m in Nino4 and 80m in Nino3), where the temperature variability is strongest.

Figure 18 shows the 1993-96 average depth of the $20^{\circ}$C isotherm (hereafter D20) for the various experiments. The D20 provides another standard diagnostic for evaluating the impact of the assimilation on the mean thermal field. Once again, EXCL displays an excessively warm thermocline and underestimated meridional gradients between the equator and $8^{\circ}$N, when compared to the other experiments. EX4D displays undulations in the D20 field near $8^{\circ}$N in the eastern Pacific, which are absent from the other analyses. These oscillations are spurious and are the result of a noisy analysis at locations near $5^{\circ}$–$8^{\circ}$N where there are few data in between TAO moorings. This problem also appears in EX3D, but is weaker and is not seen clearly in the mean D20. This problem might be the result of overfitting the data which can result in unrealistic oscillations being generated between observation points (e.g., see Fig. 2.2 in Daley (1991)). Indeed, the rms of the 0–300m vertically-averaged temperature increments along $5^{\circ}$N displays a maximum between the locations of TAO moorings (Fig. 19), with peak-to-trough differences largest in EX4D, which is consistent with Fig. 18. It also appears that the rms is smaller when the TAO moorings have shorter longitudinal separation ($10^{\circ}$ rather than $15^{\circ}$).

The EXOI analysis is included in Fig. 18 to show how similar it is to EX3D. This result may be expected from a theoretical point of view since OI and 3D-Var are just different numerical algorithms for solving the same statistical analysis problem (Lorenc 1986). In the present case, however, there are some important differences between the two systems (e.g., in the way the vertical analysis problem is solved, and in the observation-error statistics) which justify the comparison. Both EX3D and EXOI exhibit a trough of D20 in the eastern Pacific, near $2^{\circ}$S, which is absent from both the EX4D analysis and TAO data. This spurious trough in EX3D and EXOI will be discussed in more detail below.

*Velocity and salinity analysis*

Up to this point, the impact of the data assimilation on the assimilated field (subsurface temperature) has been examined. How the assimilation of this field influences the climatology of other fields will now be investigated. Figure 20 compares the 1993-96 average surface zonal velocity from the various experiments to the Reverdin *et al.* (1994) climatology. This climatology was derived from drifting buoys and TAO current meters over the January 1987 to April 1992 period, so only a qualitative comparison can be made. Figure 21 provides complementary information, showing the vertical structure of the 1993-96 averaged zonal currents in a meridional section at $140^{\circ}$W. As noted by Vialard *et al.* (2001), the control experiment reproduces the main features of the equatorial circulation: the two branches of the westward Southern Equatorial Current (SEC) near $2^{\circ}$N and $3^{\circ}$S and the eastward NECC near $7^{\circ}$N. The NECC and southern branch of the SEC, however, are underestimated in the control experiment (Fig. 20). The intensity of the NECC is clearly improved in both EX3D and EX4D (from $0.1\text{ms}^{-1}$ in EXCL to more than $0.2\text{ms}^{-1}$ in EX3D and EX4D, compared to $0.3\text{ms}^{-1}$ in the Reverdin climatology). This improvement of the NECC intensity can be linked to the steepening of the meridional temperature gradient between $5^{\circ}$N and $10^{\circ}$N noted in Figs. 16b,c, which results in a stronger geostrophic zonal current. Likewise, the southern branch of the SEC is improved in EX3D.

More striking is the large error in EX3D and EXOI in the eastern equatorial Pacific, which is associated with a surfacing of the Equatorial UnderCurrent (EUC) and unrealistic eastward currents of $0.3\text{ms}^{-1}$. This feature is linked through geostrophy to the spurious D20 trough south of the equator in EX3D and EXOI that was discussed earlier (Fig. 18). It also appears in other univariate data assimilation systems. Bell *et al.* (2001) and Burgers *et al.* (2002) argue that this feature is associated with a disruption to the main dynamical balance along the equator between the wind-stress and the pressure gradient, caused when ocean mass field data are assimilated in order to correct for the effects of wind-stress error. In particular, Bell *et al.* (2001) show that this results in a spurious downwelling in the eastern Pacific. This downwelling also appears in EX3D (Fig. 22c) and in EXOI (not shown), but not in EXCL and EX4D (Figs. 22a,b). It tends to warm the upper ocean in the eastern Pacific in EX3D and probably explains the large negative increments needed there to keep the analysis close to the observations (Fig. 17d). Burgers *et al.* (2002) have shown that these unrealistic currents in the

assimilation experiments can be eliminated by applying velocity corrections in geostrophic balance with the mass field corrections (the meridional derivative of the geostrophic relation being applied close to the equator). In 4D-Var, the analysis increment is constrained to satisfy the dynamics of the TL model so that the velocity and temperature corrections generated by 4D-Var will already be balanced to some extent. This possibly explains why EX4D does not display the spurious reversal of surface currents and downwelling in the eastern Pacific.

At the equator, the impact of the assimilation on the climatology of the subsurface currents can be assessed by comparing with current meter data from TAO. Figure 23 shows the 1993-98 average zonal current profiles, at three different locations, from TAO data and from the various experiments. The zonal currents from the control experiment are already quite close to observations in the west but the intensity of the EUC is underestimated in the central and eastern Pacific (Vialard *et al.* 2001). In the western Pacific (Fig.23a), the currents in EX3D, with an eastward bias of up to $0.2 \text{ms}^{-1}$ between 50 and 150m, are further from the observations than the currents in EXCL and EX4D, which themselves are quite similar. In the central and eastern Pacific, close to the surface, the currents in EX4D have a 0.1 to 0.2 $\text{ms}^{-1}$ westward bias, while those in EX3D have a 0.25 to 0.3 $\text{ms}^{-1}$ eastward bias. The intensity of the EUC is much closer to the observed values in EX3D than in either EXCL or EX4D. It is not clear why the EUC intensity is degraded in 4D-Var. The EUC depends on both the zonal pressure gradient and the vertical distribution of zonal wind-stress through vertical mixing processes (McCreary 1981). Since the temperature field fits the observations, the zonal pressure gradient near the equator should be in close agreement with the true gradient. The underestimation of the EUC in EX4D thus possibly stems either from too strong easterlies or from a too deep penetration of the wind momentum in the ocean.

Figure 24 shows the 1993-96 average of the salinity field at $140^\circ$ W from Levitus (1982) climatology and from the various experiments. All the experiments start from Levitus climatology, but drift away from it because of model errors. In 4D-Var, because of the multivariate coupling induced by the TL dynamics, salinity corrections are generated that can change the salinity content. Broadly speaking, the initial structures present in the Levitus initial conditions are not lost. A closer examination, however, reveals that EXCL and EX3D display too fresh water at about $12^\circ$ N, whereas the EX4D salinity does not exhibit this drift. On the other hand, the salty waters from the southern hemisphere gyre near 100m and $2^\circ$ N spread too far north in EX4D compared to Levitus.

Figure 25 shows the logarithm of the average vertical diffusion coefficient in the whole TAO region (defined here as $160^\circ$ E to $80^\circ$ W, $10^\circ$ S to $10^\circ$ N) for EX4D, EX3D, EXCL and EXOI. While EXCL has a physically-sensible structure, with the vertical mixing coefficient decreasing toward very low values below the surface mixed layer and shear zone of the EUC, both EX3D and EX4D display far too strong values of vertical mixing below 100m. Closer inspection reveals that this behaviour is intimately linked to the background-error vertical correlation scales. The vertical scales that were chosen (locally set to twice the thickness of the model level) are sufficient to provide a smooth analysis in the vertical when the TAO profiles are complete, but when data are missing at some levels, the smoothing provided by the vertical covariances is not sufficient to prevent local instabilities which can generate strong spurious mixing over a time-scale of a few days. The missing data are frequent enough to increase significantly the climatological value of the mixing at depth. This is one illustration of the critical importance of the background-error covariances in both 3D- and 4D-Var. In EXOI, the spurious convection is less intense in the TAO region, on average. This is probably linked to the fact that, in the implementation of the OI that we are using, the analysis is done at each model level after vertical interpolation of the observed profile to the model depths. While this is a poor approach when only a few levels are observed, it is however less likely to produce statically unstable profiles than in our current implementations of 3D- and 4D-Var.

In this section, it was shown that the assimilation of *in situ* temperature data impacted significantly the ocean mean state. The thermal structure is improved in the data assimilation experiments (tighter thermocline), with 4D-Var producing the closest fit to the assimilated data. However, the improvement of the climatology of the assimilated variable relative to the control is not necessarily associated with an improvement in all of the model parameters. In both 3D-Var and OI, the surface mean currents are clearly degraded in the western Pacific and at the surface in the eastern Pacific. On the other hand, the structure of the NECC, of the southern branch of the

SEC and of the EUC in the eastern Pacific are improved. In 4D-Var, the NECC is also improved, the currents in the western Pacific are similar to those in the control, and the EUC is underestimated as in the control. Both 3D- and 4D-Var display excessive vertical mixing below the thermocline. This will be further discussed in section 6.

## 5.2 Variability

In the previous section, the climatological mean structure of the analyses from the different experiments was investigated. In this section, the variability of the analyses will be evaluated. Since the results from EXOI are very similar to those from EX3D, they will not be discussed further in this section.

*Interannual variability*

Figure 26a shows the time-evolution of the monthly averaged temperature in the upper 300m (hereafter T300) of the TAO region for the various experiments. It clearly shows that the heat content (which is proportional to T300) in EXCL is too high when compared, for example, to the Levitus climatology. This is consistent with the results of the previous sections which showed that the lower thermocline is too warm in EXCL. The analysis increment acts to cool the upper ocean and restore the T300 to the level of the Levitus climatology. While this takes about four months in EX3D (i.e., 12 assimilation cycles), this is achieved after the first 30-day assimilation cycle in EX4D (in January 1993).

Figure 26b shows the temperature analysis increment from EX4D averaged over the same region, together with its time-accumulated value. The analysis increment at the beginning of the first cycle cools the T300 by about $1.5°$C over the TAO region which is approximately equal to the difference between the Levitus climatology and the control at the beginning of 1993. After this abrupt initial cooling, the increment has a tendency in EX4D to warm the ocean from 1993 to the end of 1996, clearly shown by the time-accumulated increment in Fig. 26b. This means that, while the T300 of the model without assimilation has a tendency to be too warm, the T300 at the end of each 4D-Var assimilation window has a slight tendency to be too cold. To compensate for this tendency, a warm increment is then generated at the beginning of the next cycle. This illustrates how the assimilation can change the basic balances in the model by changing the mean circulation and mixing. For example, the increased vertical mixing in EX4D (Fig. 25) could be responsible for the tendency of EX4D to become too cold, by increasing the exchanges of the upper ocean with the colder deep ocean. In EX3D, the increments act to cool systematically the background, as shown in Fig.26c (note the difference in vertical scale in panels b and c). It is probably largely due to the spurious downwelling in the eastern Pacific (Fig.22b) which tends to warm the thermocline. The assimilation increments compensate for this by systematically removing heat (the assimilation increment has contributed to cool the TAO region by $8°$C by the end of EX3D). The tendencies of the increments in EX4D to warm the model and in EX3D to cool it are interannually dependent, as can be seen during the *El Niño* event in 1997-98.

In EX4D (and in EX3D, after April 1994), the T300 time-series of Fig. 26a looks similar to that of EXCL with a constant offset. This illustrates that, despite the large bias, the model is able to reproduce the phase of the observed heat content variability from the specification of the observed wind. Closer examination, however, shows that the variability has a larger amplitude in EX3D and EX4D than in EXCL (e.g., the T300 change between the peak in November 1997 and the trough in August 1998 is $1°$C in EXCL, compared to $1.6°$C in the assimilation experiments). This shows that the assimilation of *in situ* temperature data not only has an effect on the mean state but also acts to correct the interannual variability of the heat content. This effect is, however, more modest than the correction to the bias (e.g., the change in the variability is less than $0.6°$C, while the change in the T300 bias is about $1.4°$C).

The assimilation thus mainly acts to correct for a bias in the temperature field which develops in the model because of systematic model and/or forcing error. Of particular interest is the characteristic time it takes for this

bias to develop. To determine this, experiments were performed in which the model was integrated freely (i.e., with the assimilation "turned-off") starting from initial conditions given by the 3D- and 4D-Var analyses on 26 December 1993. These will be referred to hereafter as data retention experiments and denoted REX3D and REX4D, respectively. Figure 27 shows the evolution of the mean and rms of the difference between the T300 of REX3D, REX4D and EXCL, with that of EX4D over the TAO region. EX4D is taken as reference here, because we have seen that it is the experiment that fits the observed thermal data best (Fig.12). For the first two months, the mean T300 of REX3D and REX4D stays very close to that of EX4D. However, the rms difference with EX4D shows significant differences in their spatial patterns after the first month. These differences are stronger in REX3D (about $1.3°$C) than in REX4D (about $0.9°$C).

Figure 28a,b shows a monthly average of the difference between the temperature field of the first month of REX3D and REX4D, with that of EX4D. This shows clearly that, in REX4D, the model has not drifted far from the observed equatorial thermal state. On the other hand, REX3D displays much larger errors in its thermal state after one month (differences larger than $4°$C). This is partly due to differences between the initial thermal states of REX3D and REX4D (Fig. 28f), but also to the spurious downwelling in the eastern Pacific which is present in the initial conditions of REX3D and which contributes significantly to warm the upper ocean during the early stages of integration. After six months, REX4D has a mean error in the T300 which is slightly larger than that of REX3D (Fig. 27a) , but an rms error which is smaller (Fig. 27b). This is not noticeable in the equatorial section, which shows a very similar behaviour in REX3D and REX4D after six months (Fig.28c,d), with both displaying some of the bias characteristics of EXCL such as an overly diffuse thermocline. After 1994, the mean error in T300 stabilizes at about $0.5°$C for the period 1995-1997. Associated with the 1998 *La Niña*, there is again a rise of the mean T300 error up to $1°$C. The rms-error displays a steady rise from about $1.3°$C at the beginning of 1995 to about $1.9°$C at the end of 1998, but is always below that of EXCL (between $2.1°$C and $2.7°$C). The model is thus able to retain information about the improved initial thermal state for more than 5 years. This suggests that, after the initial adjustment, the growth of error in the retention experiments is linked to slow processes (e.g., horizontal and vertical mixing). The similarity between panels c, d and e of Fig. 28 shows the tendency of the model to return to its own mean state when the assimilation is stopped.

*Higher frequency variability*

We have seen that the assimilation improves the thermal mean state and interannual variability. We will now investigate how the assimilation affects higher frequency phenomena. TIWs are the largest contributor to variability in the tropical Pacific at intraseasonal time-scales (e.g., see Baturin and Niiler (1997) for a description of TIWs in observations). The impact of TIWs on the thermal field is strongest north of the equator in the central and eastern Pacific. Figure 29a shows the daily D20 at $140°$W, $5°$N from TAO data and from the various experiments, while Fig. 29b shows their difference. The TIWs manifest themselves as large oscillations (up to 60m from peak to trough) at a 30- to 40-day time-scale. There is no TIW activity during the April-to-June period.

EXCL and EX3D do not exhibit clear TIW variability. In EX4D, however, the TIWs are reproduced with the correct phase and amplitude. The only significant misfit between EX4D and the data is observed in early February and lasts only a few days. This implies that 4D-Var is able to fit variability in the data having a time-scale shorter than the 30-day assimilation window. At first, this may seem to contradict the results of section 4.2 which suggested that the TL model did a poor job of describing TIWs. However, it may point again to the important role of the outer iterations in providing a feedback mechanism between the TL and nonlinear models so that the model can eventually achieve a very close fit to the data.

The D20 trajectory of EX4D is smooth in the sense that there are no significant "jumps" at analysis time when the increment is applied. This is also true of EX3D, because of the gradual way in which the increments are applied in 3D-Var. Since this procedure acts as a low-pass time filter (Bloom *et al.* 1996), the smoothness of the 3D-Var analysis is achieved at the expense of resolving TIW activity as illustrated in Fig.29. Whereas the

(static) linear analysis $\mathbf{w}^b(t_i) + \delta\mathbf{w}^a(t_i)$ of EX3D reproduces quite well the D20 variations associated with the TIWs, the resulting nonlinear "analysis" trajectory $\mathbf{w}^a(t_i)$ fits these variations rather poorly.

Figure 30 shows the 15-day high-pass filtered time series of the D20 from the various experiments and TAO at the same location as in Fig. 29. The TAO D20 exhibits clear variability at a time-scale close to 5 days. These are most likely equatorially-trapped internal gravity waves (IGWs), with a peak-to-peak amplitude of about 10m. The amplitude of these waves is very weak in both EXCL and EX3D. On the other hand, EX4D reproduces these waves with both the correct amplitude and phase (the correlation of EX4D with the TAO time-series is 0.76 compared to 0.11 for EX3D and -0.04 for EXCL). With a 30-day assimilation window, 4D-Var is thus able to fit phenomena at an approximately 5-day time-scale. This is an even more impressive demonstration of the ability of the TL and adjoint models to carry information accurately through time. Such a close fit is not necessarily a good feature, however. Indeed, as seen earlier, overfitting to the data in this region causes spurious undulations in the analysed D20. Furthermore, energetic IGWs generally have small spatial scales, and are thus not resolved correctly by the observation network. It may then be desirable to filter them out of the analysis. This point will be discussed further in section 6.

*Comparison with independent observations*

We now turn our attention to a comparison of the analyses with independent observations. Figure 31 shows time-series of monthly-averaged equatorial surface currents from TAO moorings and the different experiments at locations in the western (165°E), central (140°W), and eastern (110°W) Pacific. Because of gaps in the TAO data record, the thick solid curves are not continuous. The systematic eastward bias of EX3D in the central and eastern Pacific is again clearly apparent on these curves. Apart from this, all experiments have an interannual variability which is in broad overall agreement with the observed one. A more quantitative estimate of this agreement is provided in Table 1 which shows the correlation and rms-difference between the analysed currents and TAO. The statistics show that all three experiments behave similarly in the western Pacific and are in good agreement with TAO, with correlation and rms differences of about 0.9 and 0.13ms$^{-1}$, respectively. In the central Pacific, the strong eastward bias in EX3D shows up in the large rms difference (0.35ms$^{-1}$). On the other hand, the currents in EX4D are improved with respect to EXCL, with a correlation of 0.85 compared to 0.71. In the eastern Pacific, the currents in EX3D seem to have a good phase agreement with the observations (correlation of 0.79), despite a strong bias that results in a large rms difference (0.4ms$^{-1}$). EX4D and EXCL behave similarly in the eastern Pacific.

Altimeter data provide another independent verification data-set for assessing the variability in the different experiments. They give a measure not only of heat content but also of salinity content and thus will provide complementary information to that in Fig. 26a. Figure 32 and Table 2 show a comparison of TOPEX/Poseidon (T/P) sea-level data with the surface dynamic height field (relative to 2000m) computed from the different analyses. The comparison is made on the interannual anomalies (with respect to the 1993-96 seasonal cycle) averaged over the Nino3 and Nino4 regions. The statistics in Table 2 show that, in both regions, EX4D compares best with T/P, followed by EX3D and then EXCL as shown by decreasing correlations and increasing rms differences in the two regions. In Nino3, in particular, EX4D is in very good agreement with the observed sea-level for the whole period, while EX3D overestimates the sea-level rise during the 1997 *El Niño* and EXCL underestimates the sea-level fall during the 1998 *La Niña*. In Nino4, EX3D and EXCL underestimate the sea-level anomaly in 1993 and overestimate it in 1996. All three experiments tend to produce an overestimated sea-level anomaly in Nino4 in 1997–98. Since Fig. 32 displays anomalies with respect to the 1993–98 period, these discrepancies might be associated with a drift of the analysed dynamic height over the 1993–98 period. In EXCL, these discrepancies are not surprising since Fig. 26b already showed that the heat content variability in EXCL was not fully consistent with one constrained by *in situ* temperature observations. For EX3D and EX4D, whose heat content is well constrained by the observations in the TAO region, the inconsistency between the dynamic height and T/P sea-level anomalies is largely due to inaccuracies in the salinity.

Figure 33a shows the evolution of the average salinity in the top 300 metres (hereafter S300) of the TAO region in the three experiments. All start from a value close to the Levitus climatology in January 1993. EXCL drifts slowly towards fresher values (about 0.1 psu freshening after 6 years), probably due to a combination of model and forcing error. This freshening is strongly accentuated in EX3D. In a separate study, using a different OGCM, Troccoli *et al.* (2002) observed a similar freshening of the upper ocean in analyses produced with a univariate OI scheme (the same one used as a reference in this study). They attributed this feature to spurious vertical mixing and convection which was generated in regions where the density profile was destabilized by making corrections for temperature while leaving the salinity field unchanged. The fact that the 3D-Var system in this study is also univariate might suggest that the aforementioned problem is also responsible for the excessive freshening seen in Fig. 33a. In the 4D-Var system, on the other hand, salinity corrections are induced via the TL model constraint. The time-accumulated salinity increment in EX4D, averaged over the top 300 metres of the TAO region, is shown in Fig. 33b. During 1995, the 4D-Var increment adds an average of 0.2 psu in the top 300 metres of the TAO region, which is partially reflected in the average salinity time-series in Fig. 33a. The tendency of the model to drift in EXCL seems to be partially corrected for in EX4D, except after mid-1997 when EX4D exhibits a dramatic drop in the average salinity. This drop (0.2 psu of the S300 in one year which corresponds to 5 mm day$^{-1}$ of precipitation) is too large to be realistic, and is largely associated with the 4D-Var salinity increments. This suggests that the constraints introduced by the TL dynamics are probably not sufficient to constrain the salinity field fully, and that additional information may be necessary (e.g., direct observations of salinity and/or T-S relationships).

In this section, we have shown that 3D- and 4D-Var improve the variability of the heat content; e.g., the amplitude of the differences between the 1997 *El Niño* and 1998 *La Niña* are better reproduced in EX4D and EX3D than in EXCL. 4D-Var is able to fit phenomena, such as TIWs and IGWs, which have characteristic time-scales comparable to or much shorter than the width of the assimilation window. The sea-level variability is also improved since it is very closely linked to the heat content variability. This improvement is most noticeable in EX4D. The improvement of the variability of other variables (surface currents, salinity) is less spectacular, however. The surface current variability is improved in EX4D in the central Pacific but very little in the eastern and western Pacific. A salinity drift is introduced in both 3D- and 4D-Var, suggesting that additional constraints on non-assimilated variables (such as salinity) are necessary in both 3D- and 4D-Var.

|  | Equatorial surface currents vs TAO | | |
|---|---|---|---|
| *Longitude* | *Experiment* | *Correlation* | *Rms difference* |
| 165°E | EX4D | 0.91 | 0.14 |
| 165°E | EX3D | 0.90 | 0.13 |
| 165°E | EXCL | 0.92 | 0.12 |
| 140°W | EX4D | 0.85 | 0.16 |
| 140°W | EX3D | 0.71 | 0.35 |
| 140°W | EXCL | 0.71 | 0.18 |
| 110°W | EX4D | 0.68 | 0.25 |
| 110°W | EX3D | 0.79 | 0.40 |
| 110°W | EXCL | 0.69 | 0.20 |

*Table 1: Correlation and rms difference (in ms$^{-1}$) between the 1993-98 monthly-averaged equatorial surface currents from TAO and the different analyses.*

|  | Dynamic height vs T/P | | |
|---|---|---|---|
| *Region* | *Experiment* | *Correlation* | *Rms difference* |
| Nino4 | EX4D | 0.87 | 2.49 |
| Nino4 | EX3D | 0.83 | 3.55 |
| Nino4 | EXCL | 0.54 | 4.80 |
| Nino3 | EX4D | 0.98 | 1.30 |
| Nino3 | EX3D | 0.97 | 2.01 |
| Nino3 | EXCL | 0.94 | 2.57 |

*Table 2: Correlation and rms difference (in cm) between the 1993-98 monthly-averaged sea level from TOPEX/Poseidon and the model dynamic height from the different analyses.*

## a) 4D-Var



## b) 3D-Var



## c) Control
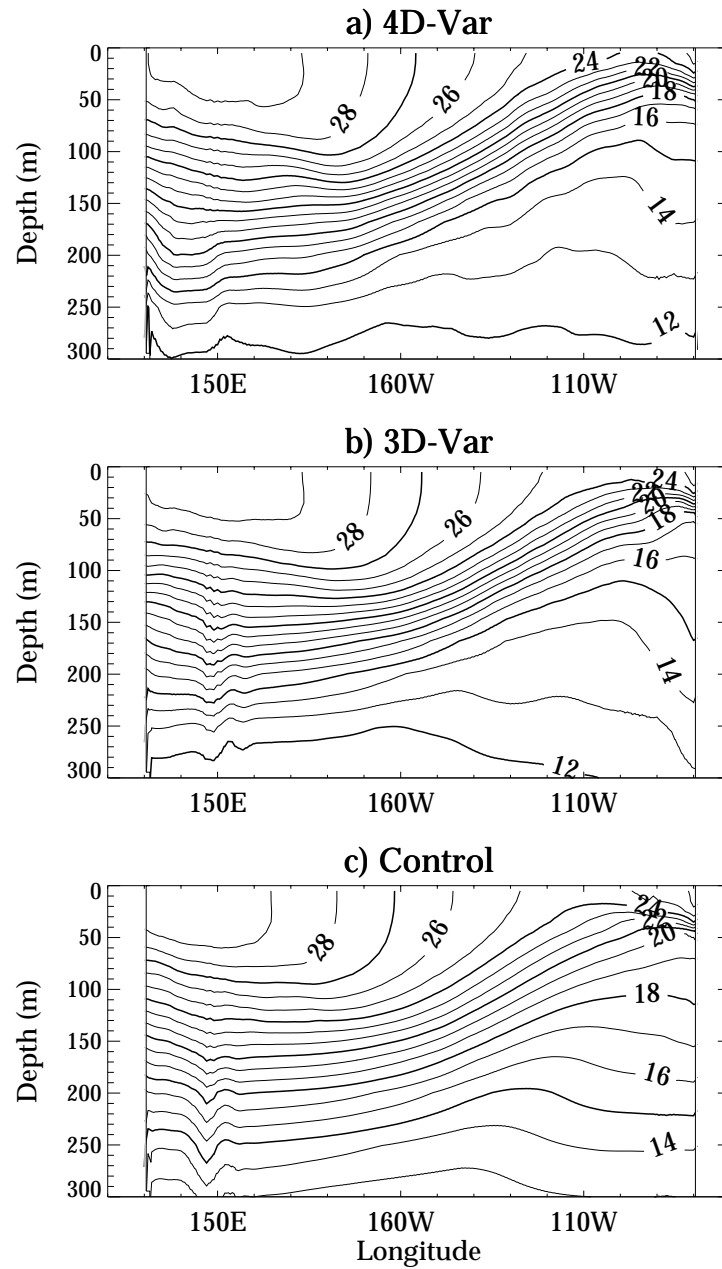


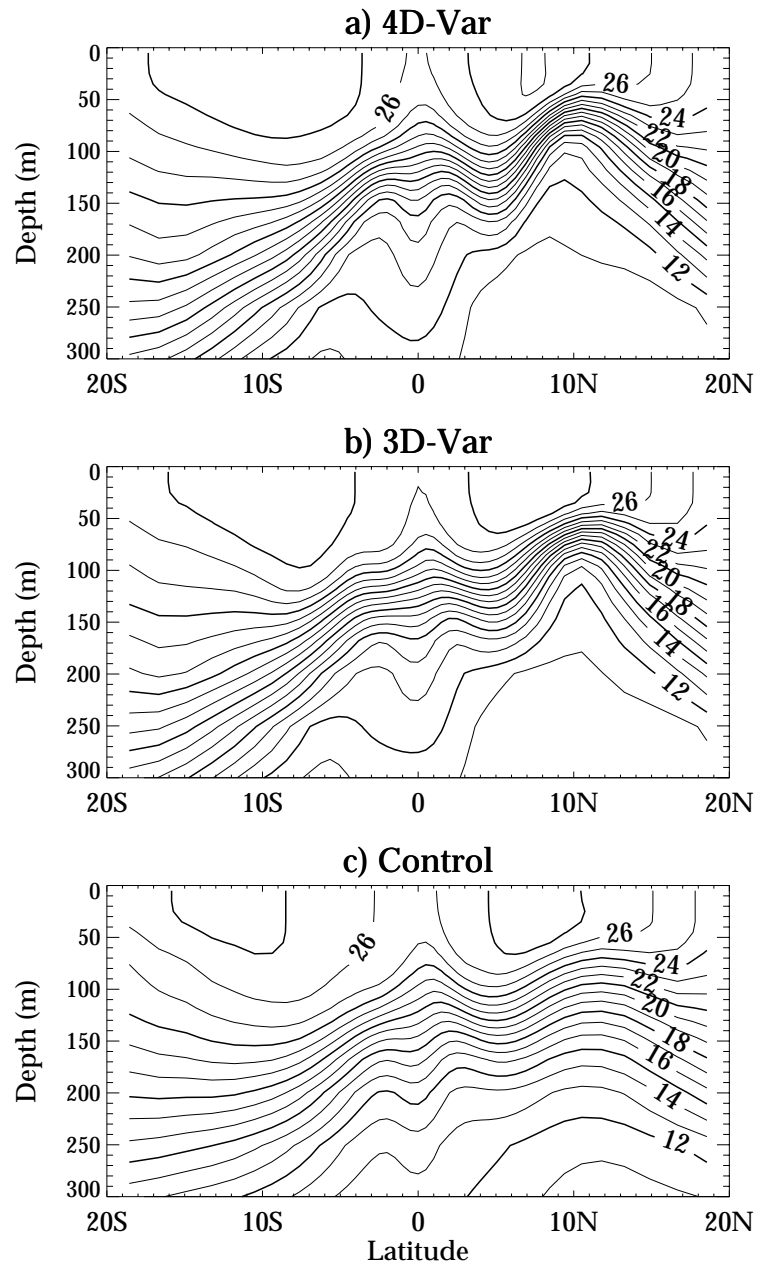*Figure 15: Zonal section along the equator of the 1993-96 average temperature in a) EX4D, b) EX3D, and c) EXCL. The contour interval is 1°C.*

*Figure 16: Meridional section along 140°W of the 1993-96 average temperature in a) EX4D, b) EX3D, and c) EXCL. The contour interval is 1°C.*
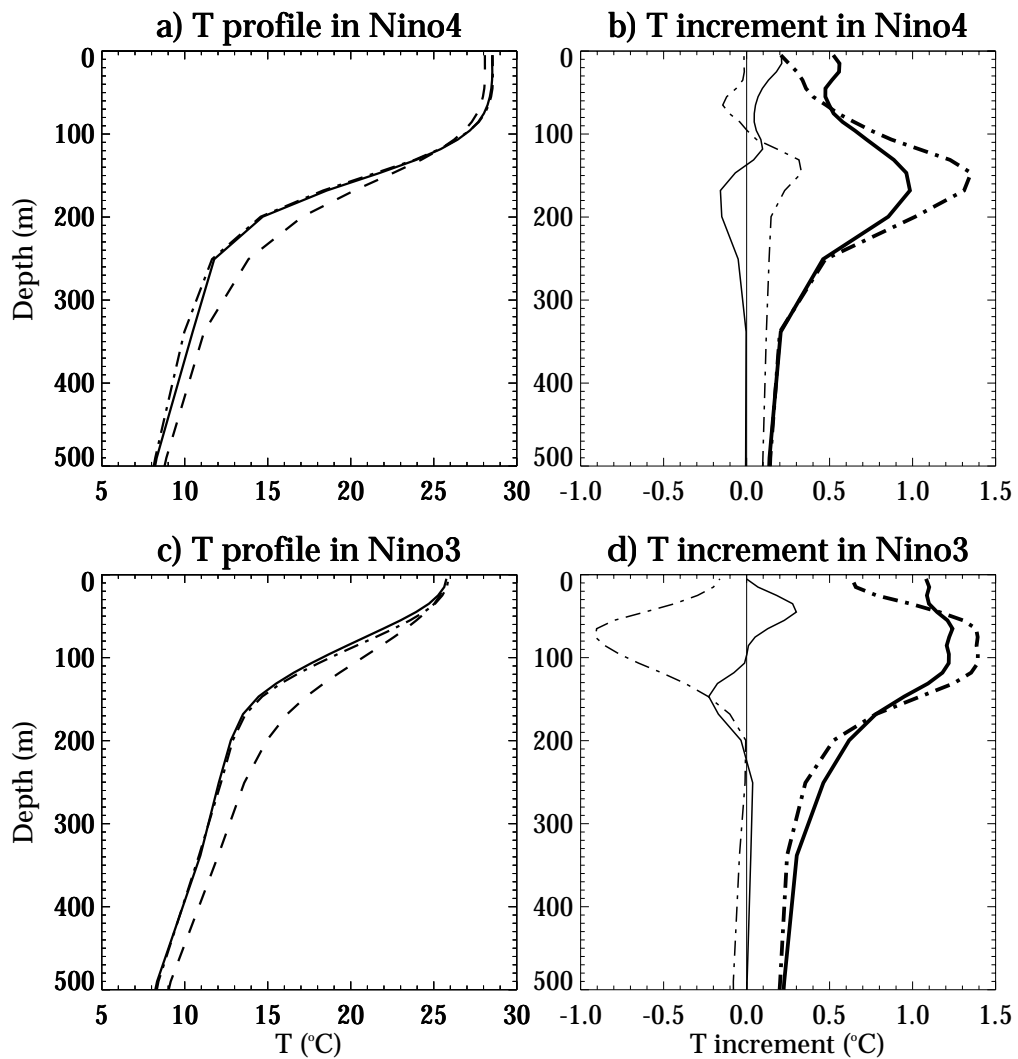
## a) T profile in Nino4

## b) T increment in Nino4

## c) T profile in Nino3

## d) T increment in Nino3

*Figure 17: 1993-96 average temperature profile in a) Nino4 and c) Nino3. Panels b and d show the average (thin curve) and standard deviation (thick curve) of the increments in EX4D and EX3D. EX4D is displayed with a solid curve, EX3D with a dashed-dotted curve and EXCL with a dashed curve.*
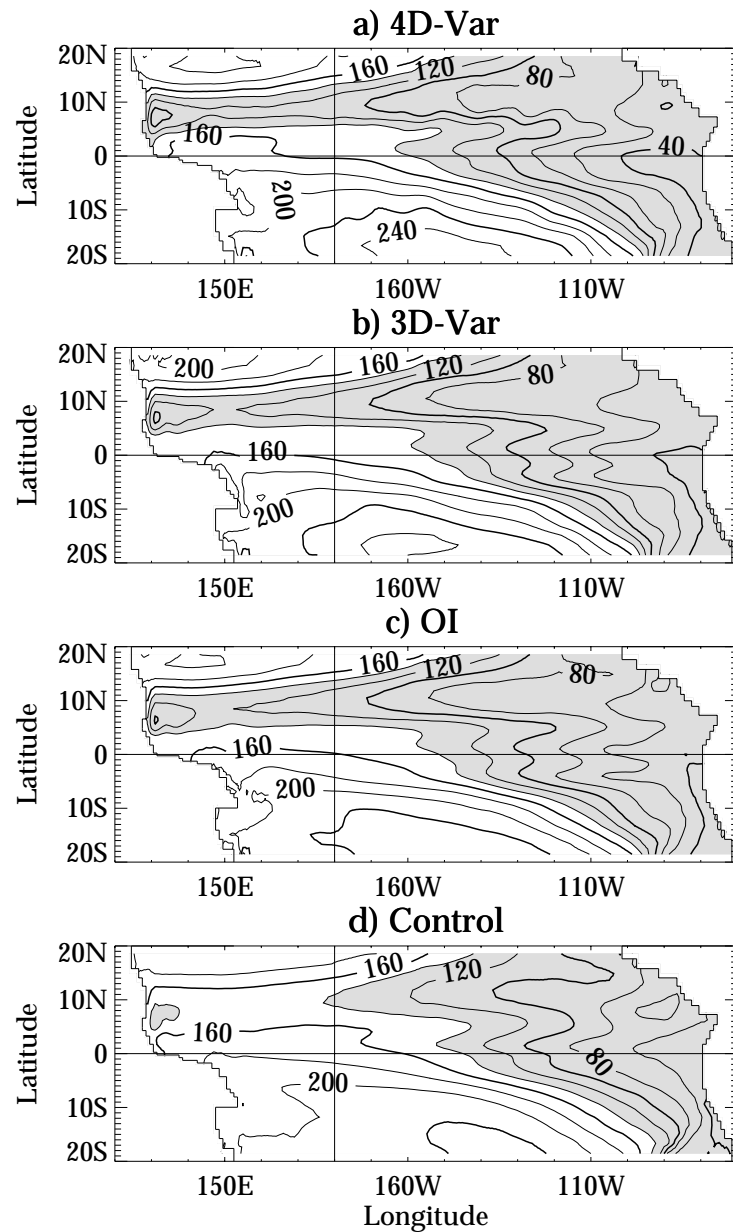
*Figure 18: The 1993-96 average of the depth of the 20°C isotherm from a) EX4D, b) EX3D, c) EXOI, and d) EXCL. The contour interval is 20m, and the shaded regions indicate values shallower than 140m.*

## Rms of 0-300m T increments along 5°N
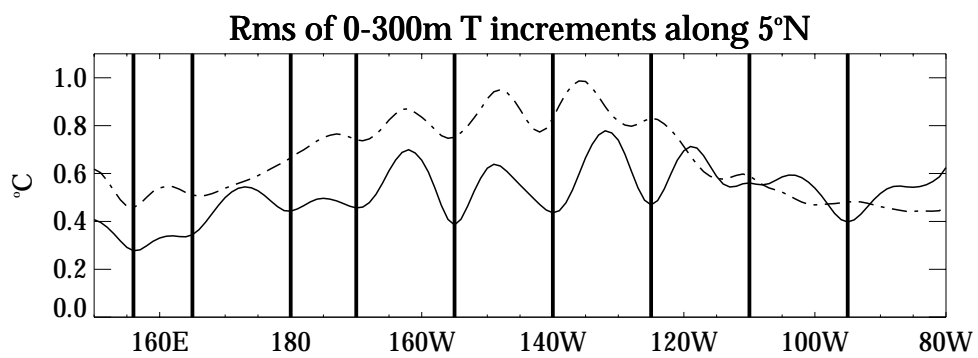


*Figure 19: Root-mean-square value of the vertically-averaged temperature increments along 5°N for EX4D (solid curve) and EX3D (dashed-dotted curve). The thick vertical lines indicate the positions of the TAO moorings.*
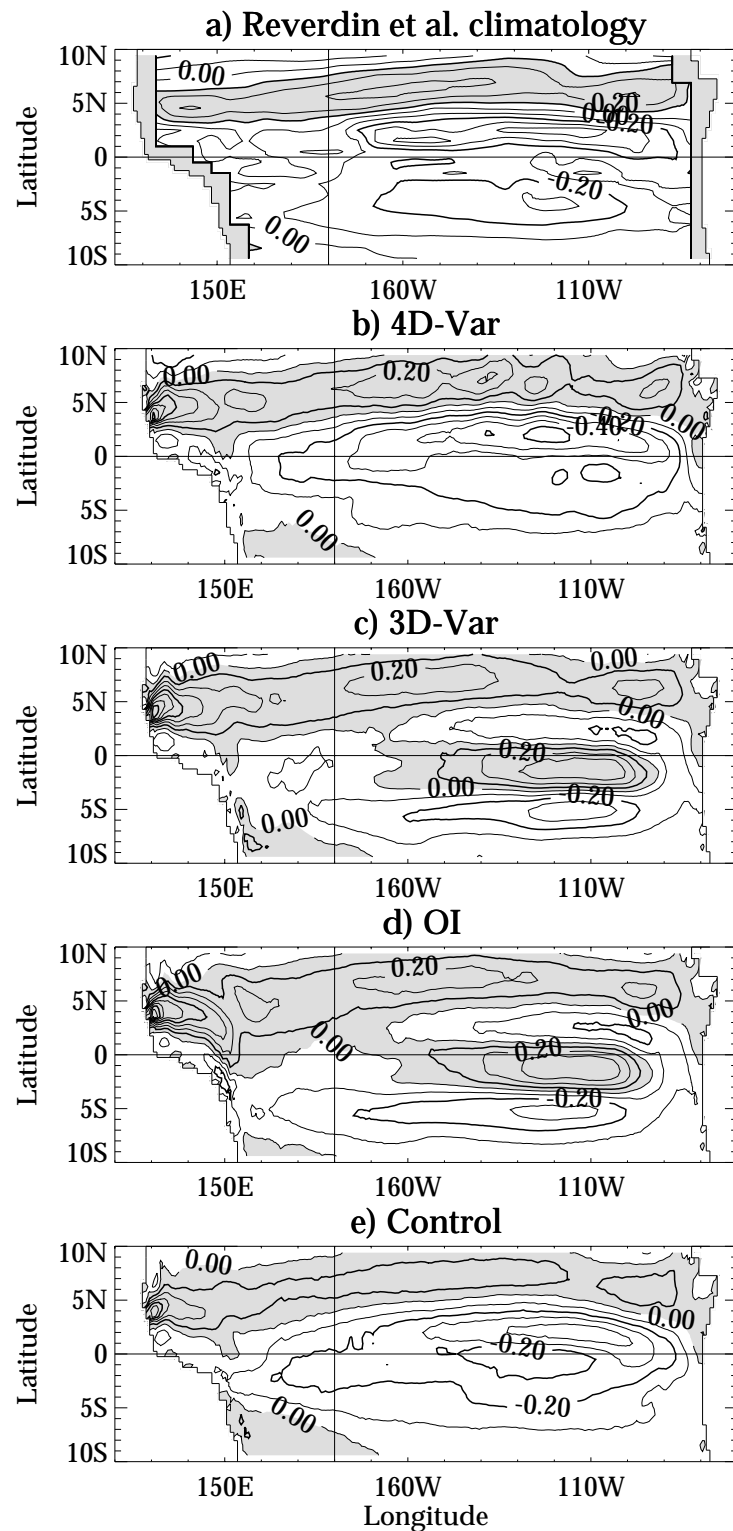
### a) Reverdin et al. climatology

### b) 4D-Var

### c) 3D-Var

### d) OI

### e) Control

*Figure 20: Surface zonal current climatologies. a) The Reverdin* et al. *(1994) climatology is representative of the January 1987 to April 1992 period. The climatologies from b) EX4D, c) EX3D, d) EXOI, and e) EXCL are averaged over the 1993-96 period. The contour interval is 0.1 ms$^{-1}$, and the shaded regions indicate eastward currents.*
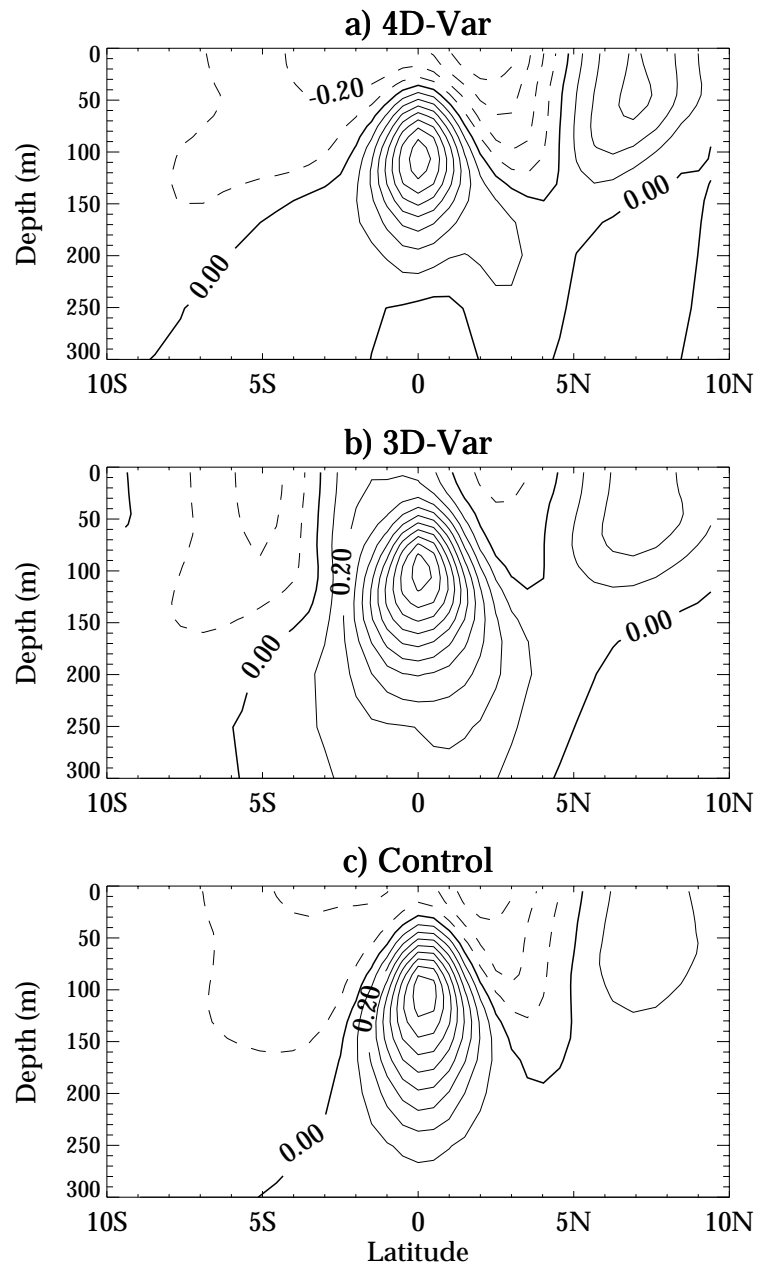
*Figure 21: Meridional section of the 1993-96 average zonal current field at 140°W from a) EX4D, b) EX3D, and c) EXCL. The contour interval is 0.1 ms$^{-1}$. Dashed contours indicate westward currents.*

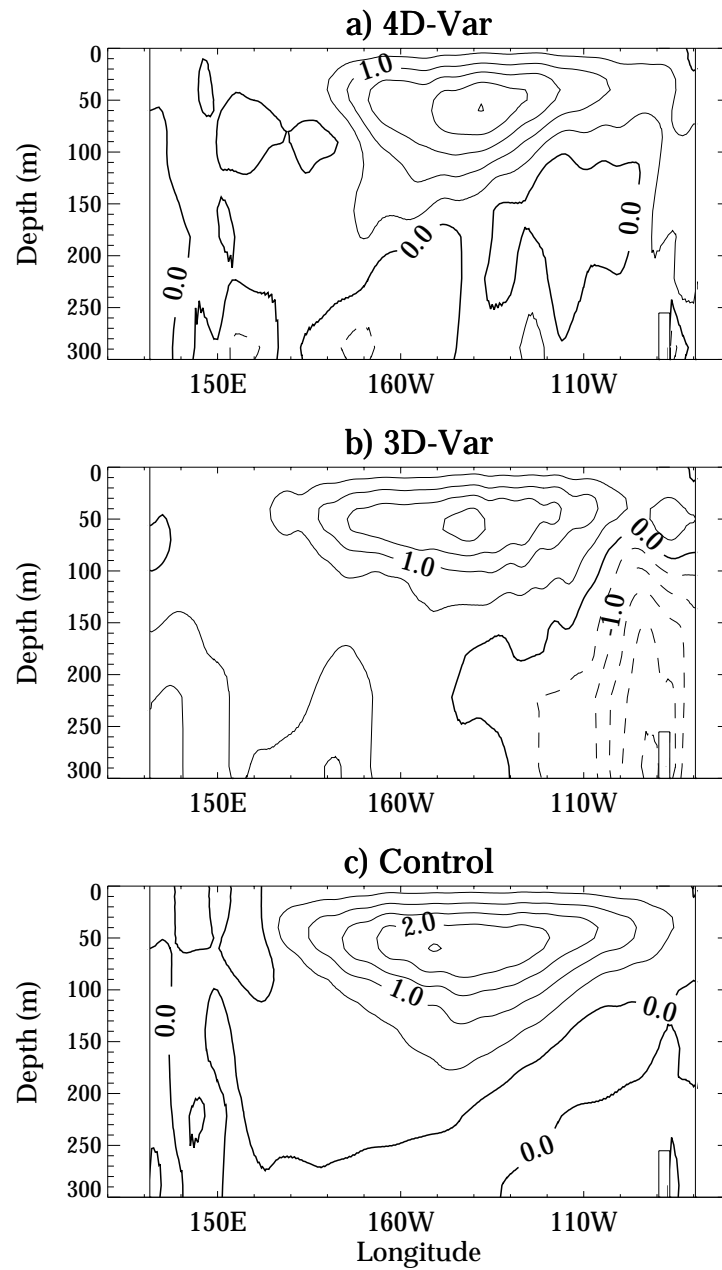*Figure 22: The 1993-96 average vertical currents along the equator from a) EX4D, b) EX3D and c) EXCL. The contour interval is 0.5 m day$^{-1}$. Dashed contours indicate downwelling.*
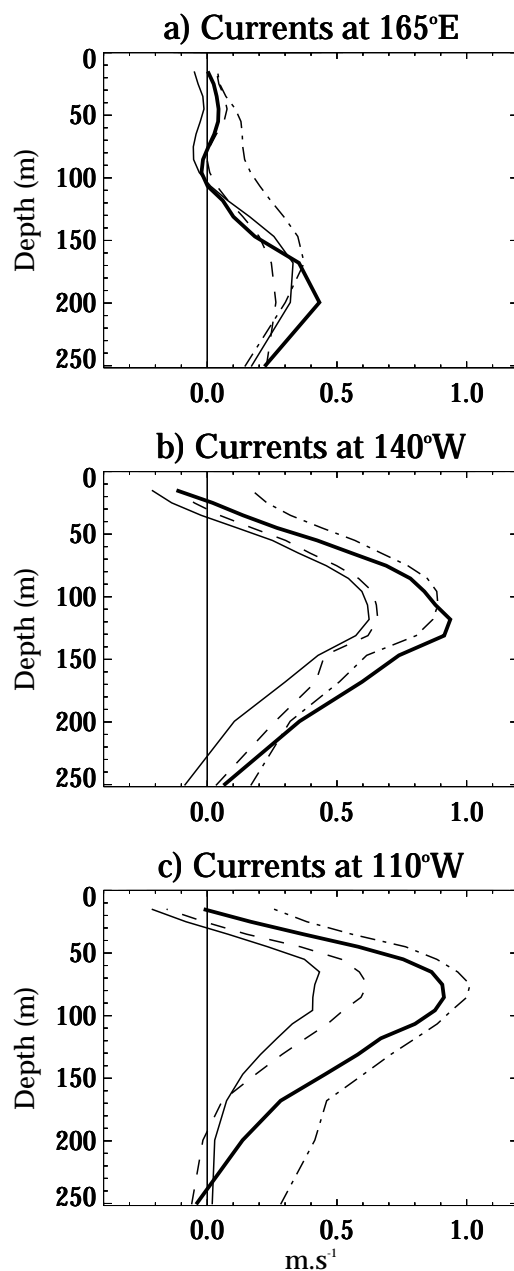
*Figure 23: Vertical profiles of 1993-98 monthly-averaged zonal currents at the equator from TAO (thick solid curve), EX4D (thin solid curve), EX3D (dashed-dotted curve) and EXCL (dashed curve). The model values have been sampled in the same way as the data (i.e., when there are gaps in the data, no model values are used).*

## a) Levitus



## b) 4D-Var
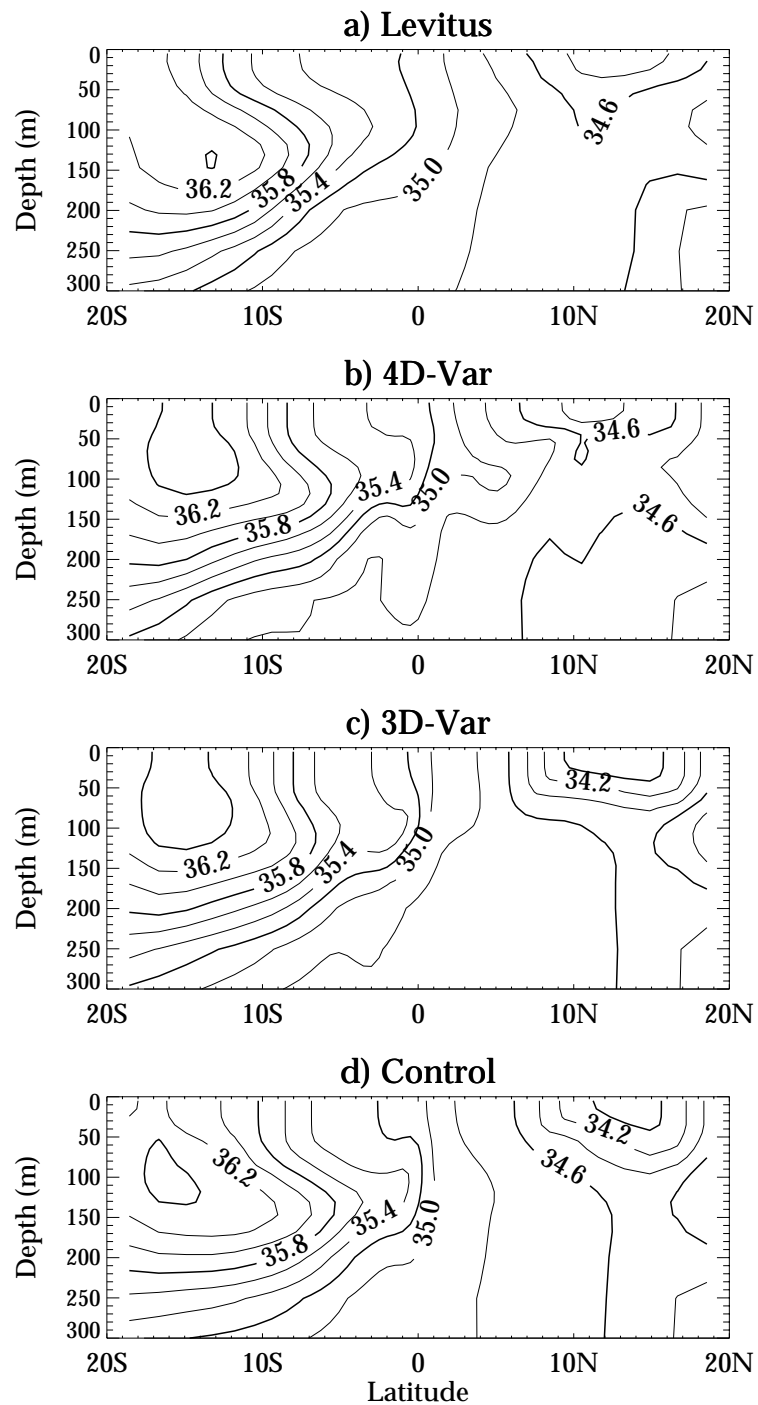


## c) 3D-Var



## d) Control



*Figure 24: Meridional section at 140°W of the salinity climatologies from a) Levitus (1982), and the 1993-96 average from b) EX4D, c) EX3D, and d) EXCL. The contour interval is 0.2 psu.*
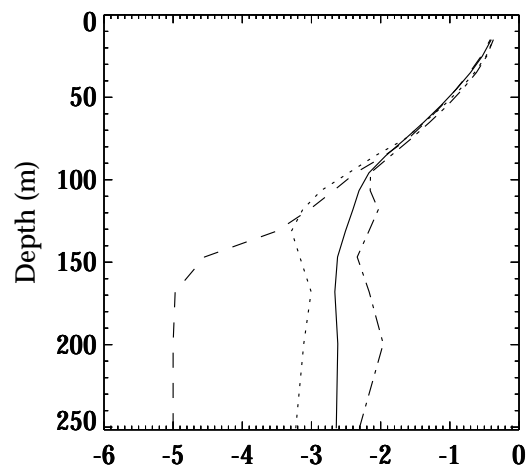
*Figure 25: Vertical profile of the logarithm of the average vertical mixing coefficient in Nino3. The solid curve corresponds to EX4D, the dashed-dotted curve to EX3D, the dotted curve to EXOI, and the dashed curve to EXCL.*

## a) T300



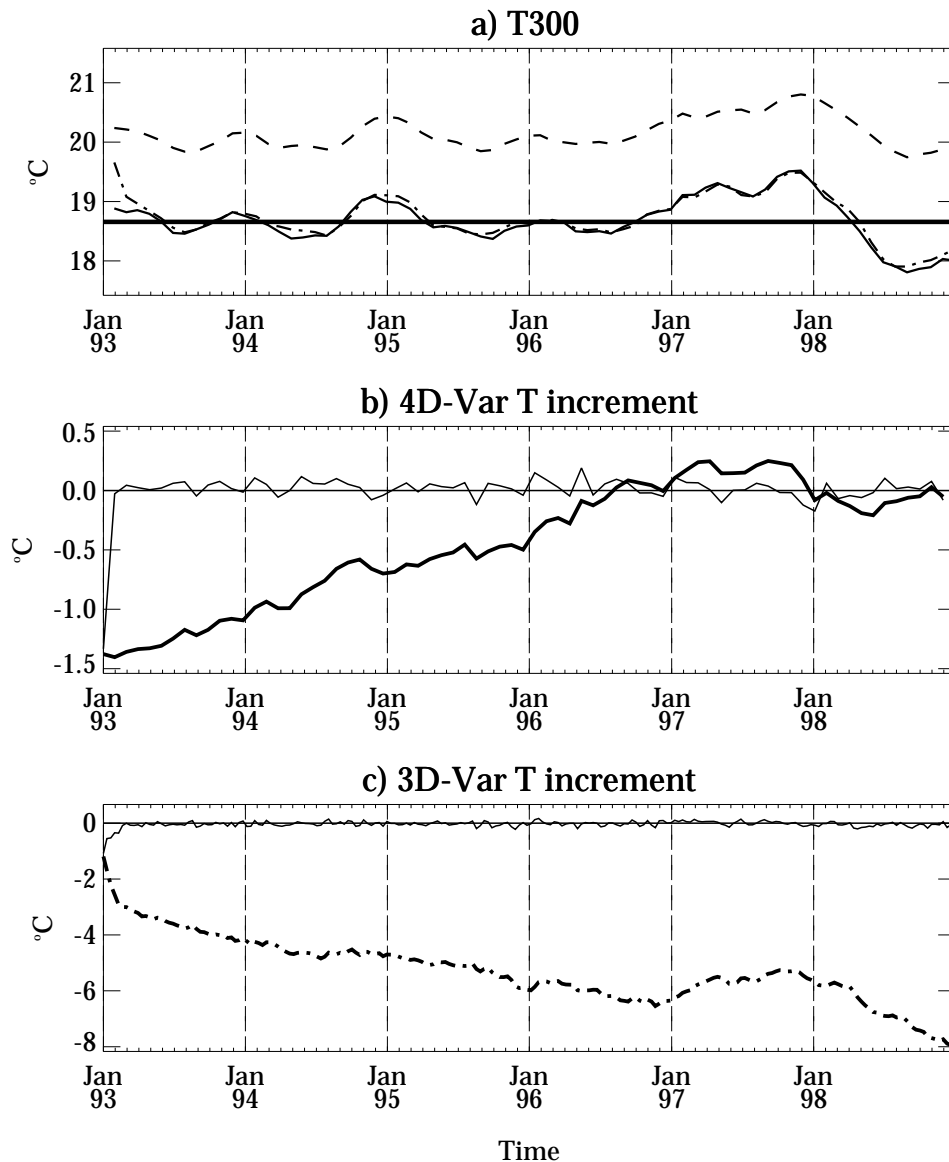## b) 4D-Var T increment



## c) 3D-Var T increment



*Figure 26: a) The averaged temperature analysis for EX4D (solid curve), EX3D (dashed-dotted curve) and EXCL (dashed curve). The average is taken over the first 300m in the TAO region. The thick horizontal line indicates the Levitus climatological value. b) The instantaneous (thin curve) and time-accumulated (thick curve) temperature analysis increment from EX4D, averaged as in panel a. c) As in panel b but for EX3D. Note the difference in vertical scale between panels b and c.*
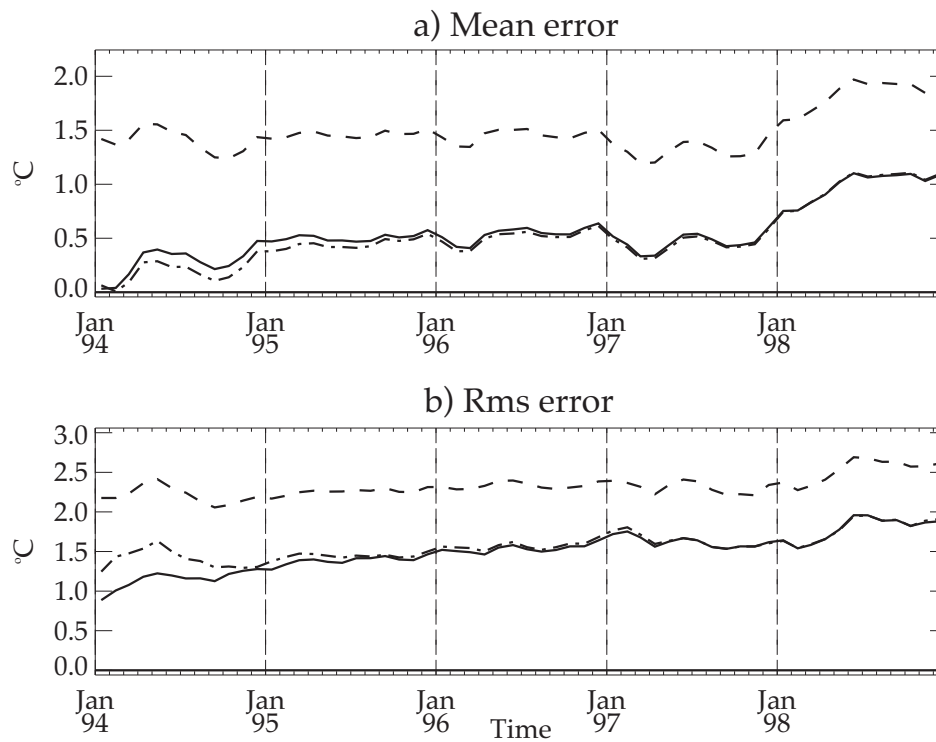
## a) Mean error



## b) Rms error



*Figure 27: a) Mean and b) rms of the difference between the average temperature of three experiments without data assimilation with that of EX4D. EX4D is considered here as our best estimate of the true thermal state of the ocean. The average is taken over the first 300m of the TAO region. The experiments without data assimilation are EXCL (dashed curve) and two data retention experiments, REX3D (dashed-dotted curve) and REX4D (solid curve), initiated from the EX3D and EX4D analyses on 26 December 1993.*
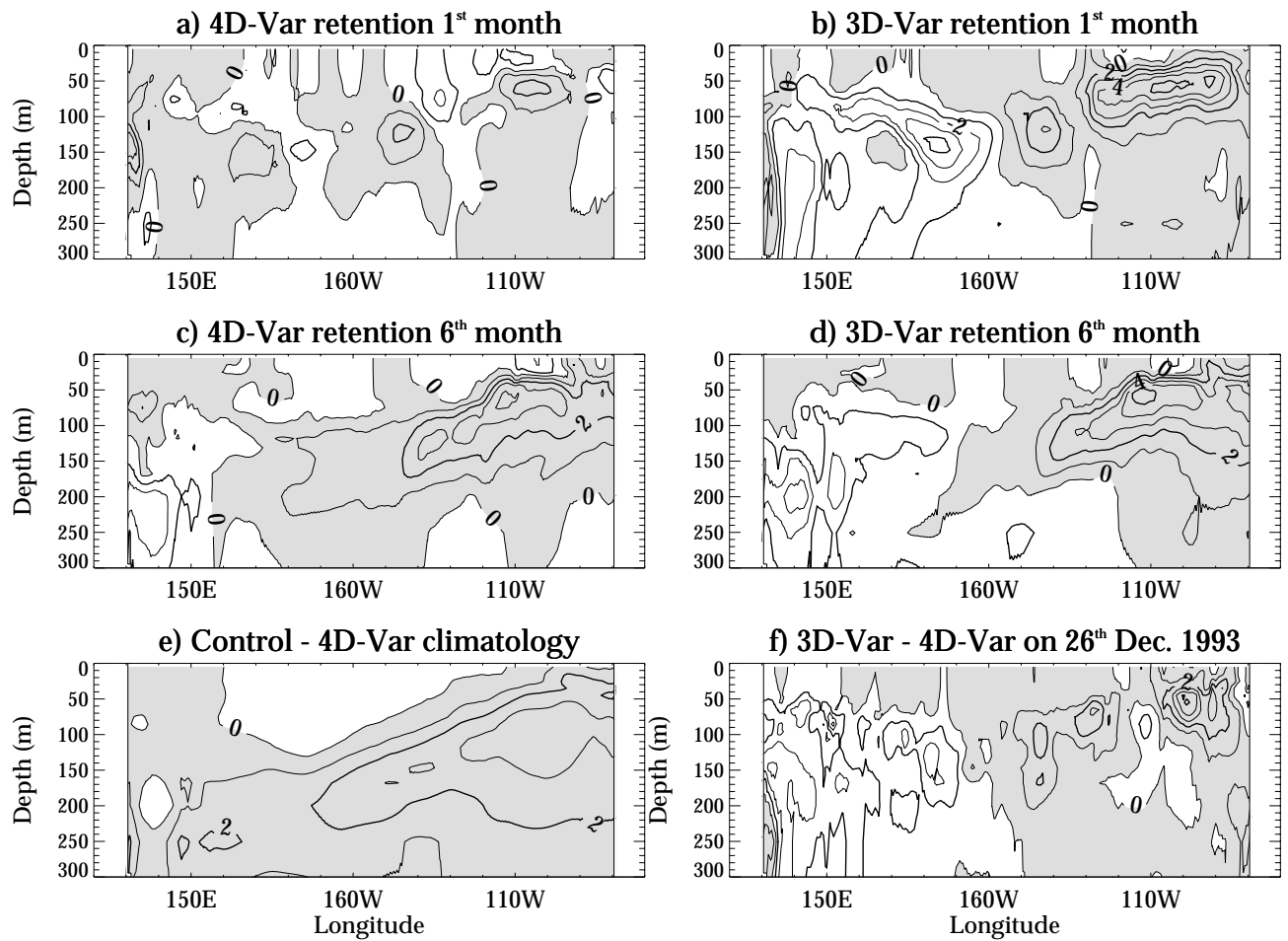
Figure 28: *Vertical section along the equator of the difference between the temperature in the data retention experiment REX4D (a free integration of the model starting from the EX4D analysis on 26 December 1993) and that of EX4D after a) one month and c) 6 months. Panels b and d show the same quantities for REX3D (a free integration initiated from the EX3D analysis on 26 December 1993). Panel e shows the difference between the 1993-96 averaged temperature of EX4D and EXCL. Panel f shows the difference between the initial conditions of REX3D and REX4D. Note the tendency of the models to return toward the mean state of the control experiment when the assimilation is stopped. The contour interval is 1°C.*

## a) D20 for TAO mooring at 140°W, 5°N
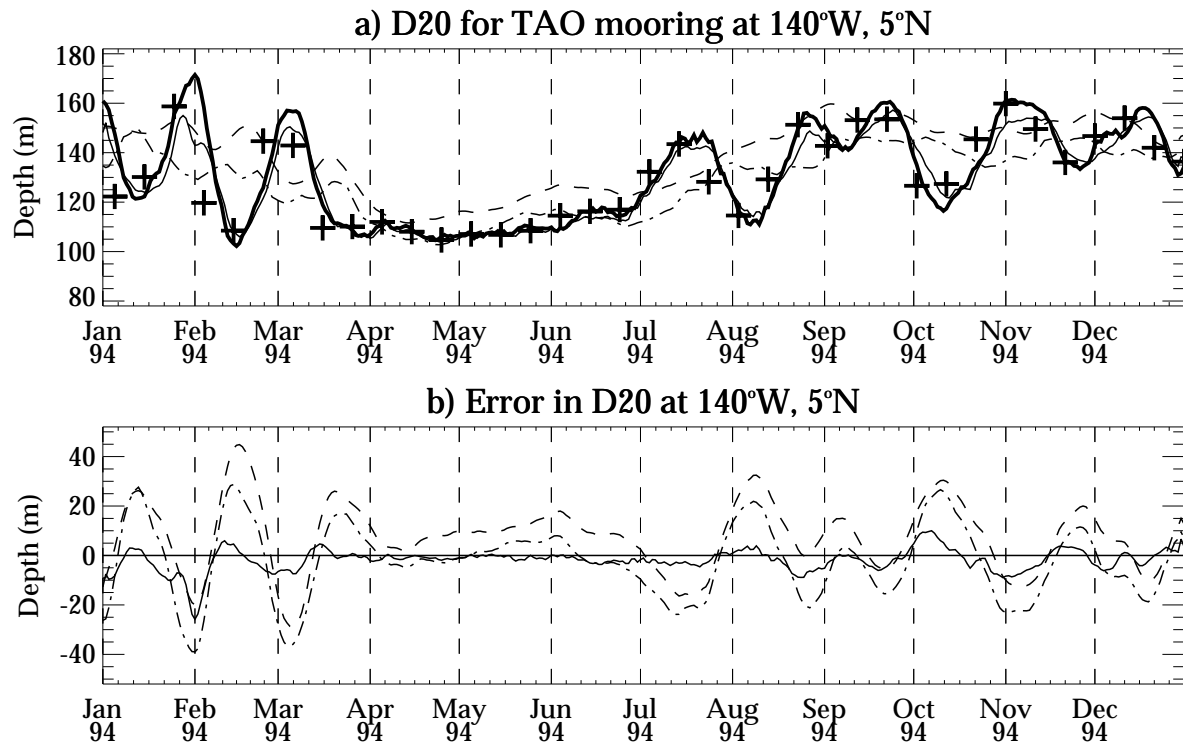


## b) Error in D20 at 140°W, 5°N



*Figure 29: a) Time-series of the daily averaged D20 during 1994 at 140°W, 5°N. b) Time-series of the daily-averaged D20 error (difference from TAO) at each location. The thick curve in panel a is the (assimilated) TAO in situ data. In panels a and b, the solid curves corresponds to EX4D, the dashed-dotted curves to EX3D, and the dashed curves to EXCL. All time-series have been smoothed using a 5-day sliding average. The crosses in panel a indicate the D20 of EX3D computed at the observation points from the linear (static) analysis $\mathbf{w}^b(t_i) + \delta\mathbf{w}^a(t_i)$. The dashed-dotted curve corresponds to the nonlinear analysis trajectory $\mathbf{w}^a(t_i)$ obtained by applying the analysis increment gradually over a 10-day assimilation window.*

## High-passed filtered D20 at 140°W, 5°N
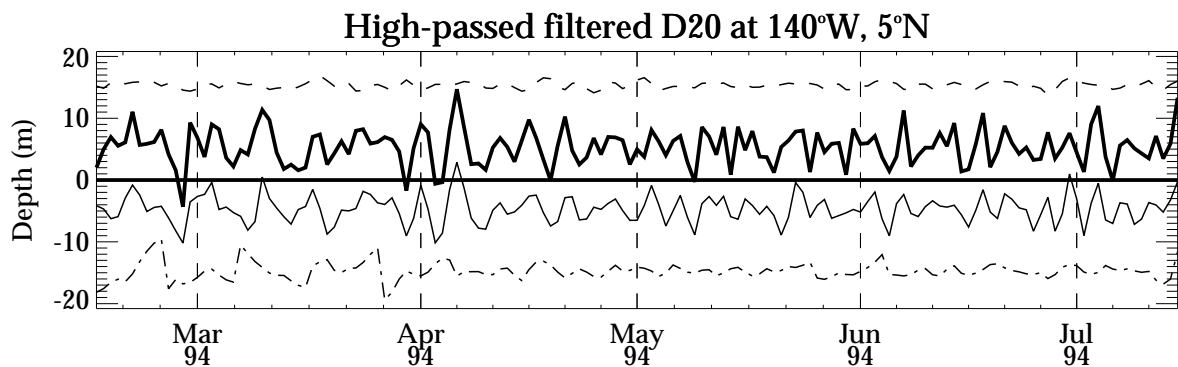


*Figure 30: a) Time-series of the high-pass filtered daily-averaged D20 during 1994 at 140°W, 5°N. The high-pass filter retains all the time scales shorter than 15 days and thus isolates equatorially-trapped internal gravity waves. The thick solid curve corresponds to TAO, the thin solid curve to EX4D, the dashed-dotted curve to EX3D, and the dashed curve to EXCL. For clarity, the curves for EX3D, EX4D, TAO and EXCL have been shifted by -15m, -5m, 5m and 15m, respectively.*
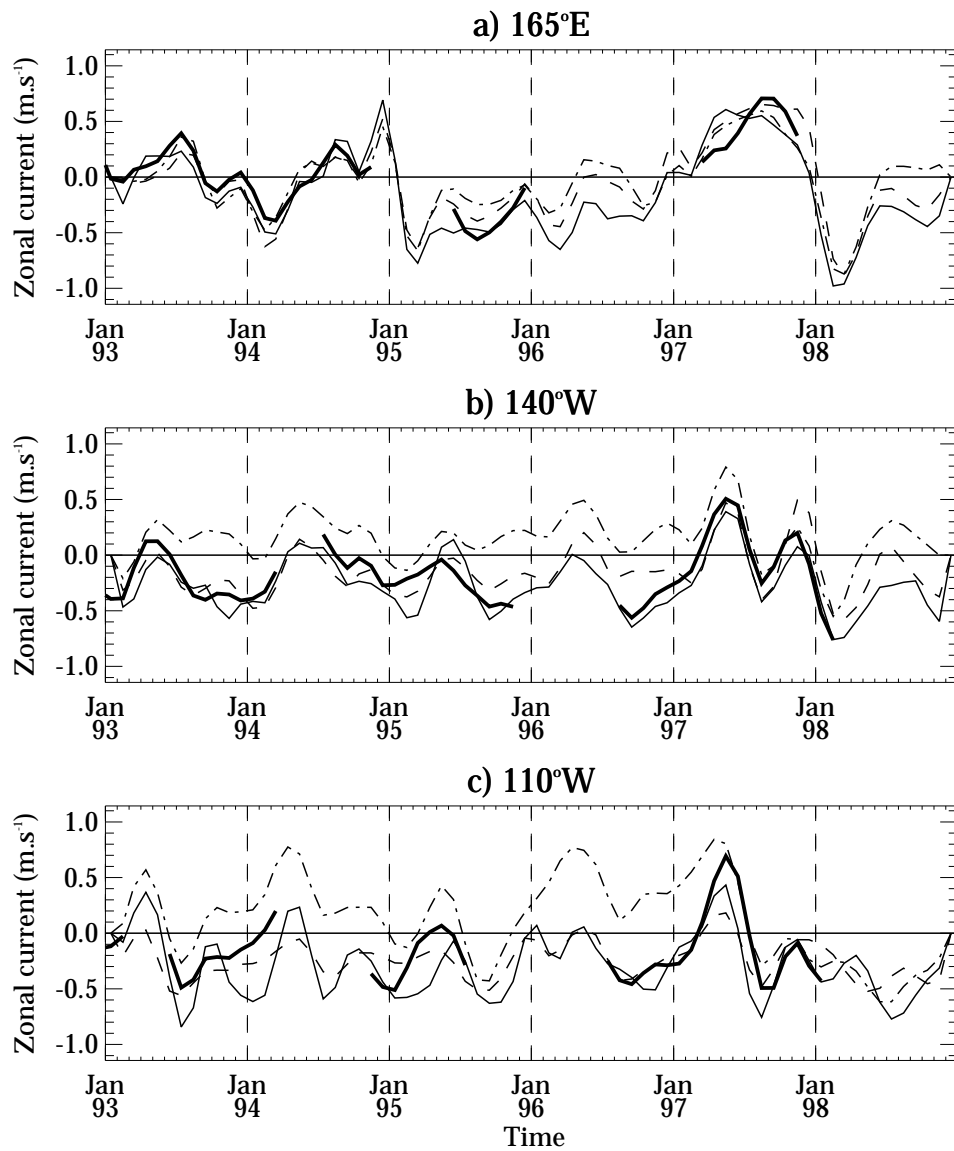
## a) 165°E



## b) 140°W

## c) 110°W

*Figure 31: Time-series of monthly-averaged surface zonal currents along the equator at a) 165°E; b) 140°W; and c) 110°W from TAO (thick curve), EX4D (solid curve), EX3D (dashed-dotted curve), and EXCL (dashed curve). A (0.25,0.5,0.25)-filter was applied to each curve.*
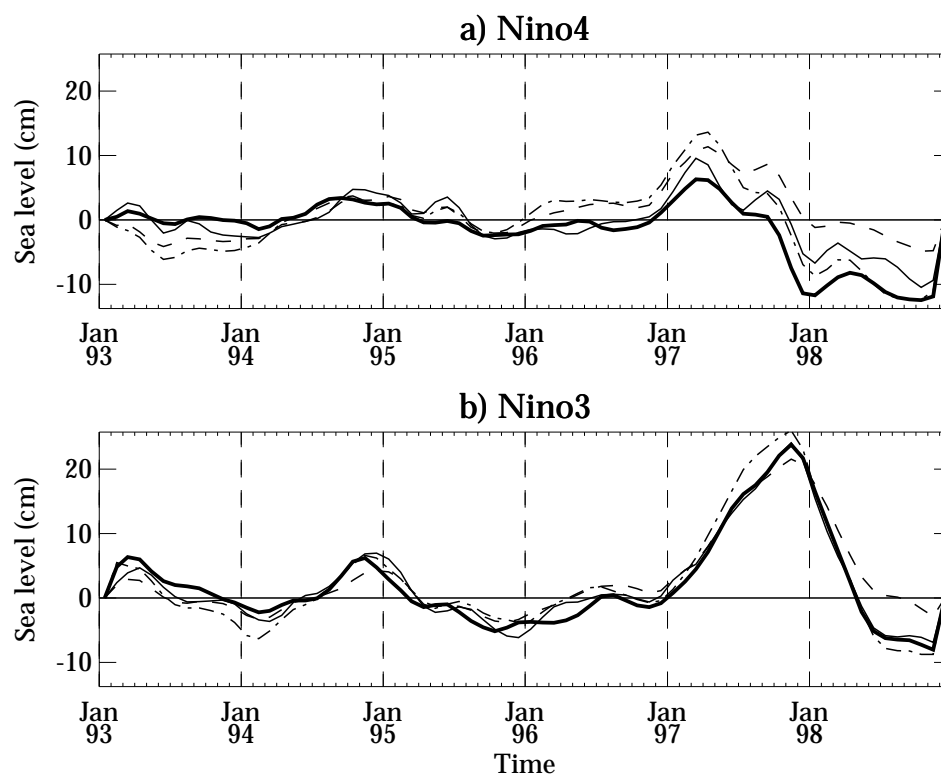
## a) Nino4



## b) Nino3



*Figure 32: Time-series of the monthly-averaged sea-level interannual anomaly from TOPEX/Poseidon data (thick curve), and dynamic height from the model referenced to 2000m in a) Nino4 and b) Nino3. EX4D is the solid curve, EX3D the dashed-dotted curve, and EXCL the dashed curve. A (0.25,0.5,0.25)-filter was applied to each curve.*

Figure 33: a) The averaged salinity analysis for EX4D (solid curve), EX3D (dashed-dotted curve) and EXCL (dashed curve). The average is taken over the first 300m in the TAO region (defined as 1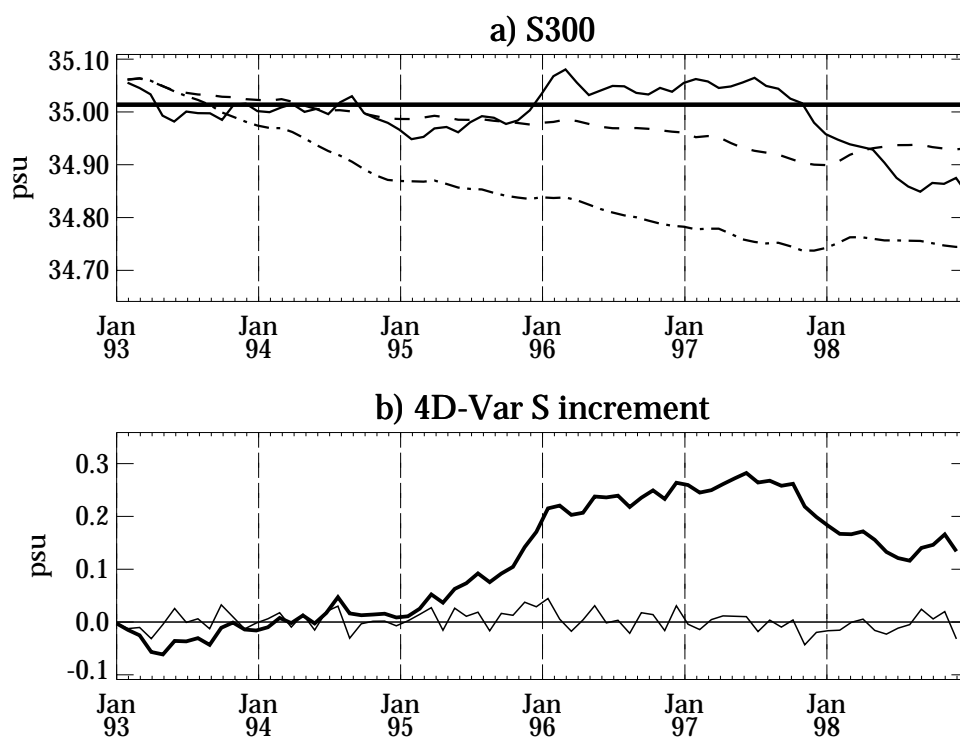60°E to 80°W, 10°S to 10°N). The thick horizontal line indicates the Levitus climatological value. b) The instantaneous (solid curve) and time-accumulated (thick curve) salinity analysis increment from EX4D (averaged as in panel a).

# 6  Summary and discussion

## 6.1  Summary

Three- and four-dimensional variational assimilation systems have been developed for the rigid-lid version of the OPA OGCM (Madec *et al.* 1998). The assimilation problem is defined by a cost function that penalizes departures from the data and from a background estimate which is the result of a previous assimilation. The control variable of the cost function is the initial condition at the start of each assimilation window. The cost function is minimized using an incremental approach by which the full minimization problem, involving the nonlinear OGCM as a constraint, is approximated by a sequence of quadratic minimization problems involving linear constraints. The control variable of each quadratic cost function is an increment to the initial conditions. In the incremental 3D-Var, the increment is transported forward in time by a persistence model. In the incremental 4D-Var, a linearised version of the full OGCM is used to propagate the increment. The adjoint of the linear model propagator is used to compute the gradient of the cost function with respect to the initial condition increment so allowing the solution to be found iteratively using a gradient descent method. Once the analysis increment is found, it is applied at the beginning of the assimilation window to derive the 4D-Var analysis trajectory. In the case of 3D-Var, it is applied as a constant 3D forcing to the model equations over the assimilation window as a way of minimizing spurious adjustments.

The systems have been applied to assimilate *in situ* temperature data in the tropical Pacific Ocean. The version of OPA used in this study is described in Vialard *et al.* (2001). The model has a horizontal resolution of $1^\circ$ (zonal) by $0.5^\circ$ (meridional) near the equator, and a vertical resolution of approximately 10m in the upper 150m. It has realistic coastlines and bathymetry, and uses an elaborate vertical mixing scheme (Blanke and Delecluse 1993). Tangent-linear and adjoint models have been developed for all relevant dynamics and physics. Only changes in vertical mixing *coefficients* associated with perturbations of the ocean temperature, salinity and currents are neglected. The present formulation of the background-error covariance matrix is univariate (there are no cross correlations between temperature and salinity, or between the density field and currents). Horizontal and vertical correlations are modelled using a diffusion equation. The resulting horizontal correlations are approximately Gaussian and have been made anisotropic to take into account well-known differences between zonal and meridional length scales in the equatorial waveguide. At the equator, a zonal scale of $8^\circ$ and meridional scale of $2^\circ$ were chosen for the temperature field. The vertical correlations are also Gaussian and anisotropic, with a depth scale taken to be a function of the vertical grid-spacing in the model. In the upper 150m, the depth scale is approximately 20m. The variances of the background-error covariance matrix are derived from the model climatology. The observations consist of *in situ* temperature data (primarily TAO and XBTs) from the GTSPP data-set, manually quality-controlled at ECMWF. The observation operator is a linear interpolation in space and also includes a daily averaging for TAO data. The observation errors are assumed to be uncorrelated in time and space and to have a standard deviation of $0.5^\circ$C for TAO and $1^\circ$C for all other data.

Four experiments were performed for the 1993-98 period: a control experiment without data assimilation; an experiment using the ECMWF version of the Smith *et al.* (1991) OI scheme, cycled with a 10-day window; an experiment using 3D-Var, also cycled with a 10-day window; and an experiment using 4D-Var cycled with a 30-day window. The validity of the persistence model (3D-Var) and of the TL model (4D-Var) was investigated. It was shown that persistence was a reasonable assumption over 10 days, and that the TL model provides a good description of the large-scale oceanic state over several months. However, because of the nonlinear nature of convective and vertical mixing processes, the validity of the TL model could be degraded at small vertical scales. Tropical instability waves (TIWs) are nonlinear oscillations with a time-scale of about one month. At their horizontal scale, the TL model is also less accurate. Nevertheless, in 4D-Var a very good fit to the observed TIWs was achieved. This result points to the important role of the outer iterations in providing a feedback mechanism between the TL and nonlinear models so that the model can eventually achieve a very close fit to the data.

The convergence properties of the 3D- and 4D-Var have been examined. 3D-Var converges more quickly than 4D-Var. In the latter, trajectory updates with the nonlinear model contribute significantly to reduce the final value of the full (nonincremental) cost function, which illustrates the importance of the outer loops in the incremental 4D-Var algorithm. Furthermore, the final values of the incremental and nonincremental cost functions are shown to be very close, which provides a good measure of the consistency and efficiency of the incremental approach.

Single observations experiments have been performed to illustrate the effect of the TL dynamics in modifying the prior estimates of the background-error variances. The TL dynamics were shown to modify the variances in a physically sensible way. The variances were homogenised and diminished in the mixed layer, and the maximum value of the variance in the profile could be increased and displaced to the level of the background thermocline, where thermal variability (and background error) is greatest.

A detailed examination of the fit of the different analyses to the assimilated data has been examined. The control experiment displays a large bias below the thermocline, which is strongly reduced in the 3D-Var analyses and almost entirely absent from the 4D-Var analyses. The rms difference between the analyses and observations is also very much reduced in the thermocline region. Whereas it is about $2.8^\circ$C in the control, it falls to $1.4^\circ$C in 3D-Var and to below $0.5^\circ$C in 4D-Var, which is less than the specified standard deviation of observation error. Over the TAO region, the spatially-averaged rms difference between the observations and the 3D- and 4D-Var analyses is stationary in time (equal to $1^\circ$C in 3D-Var and $0.4^\circ$ in 4D-Var), and in particular does not exhibit any dependence on the number of observations or interannual variability.

The 1993-98 climatologies of *in situ* temperature show that the overall effect of assimilation is to greatly reduce a model bias. The lower thermocline is colder in the assimilation experiments, and the thermocline is tighter. Experiments initiated with 3D- and 4D-Var analyses were performed to determine how long improvements in the heat content could be preserved when the assimilation stops. After one month, the experiment starting from the 4D-Var analysis was still close to the observed thermal state, whereas the one starting from the 3D-Var analysis degraded more quickly especially in the eastern Pacific. At longer lead times, the two experiments displayed similar behaviour, with a significant bias developing in the thermocline in both after about 6 months. Even so, improvement of the heat content is retained for more than 5 years. This is in marked contrast to the earlier studies of Moore and Anderson (1989) and Derber and Rosati (1989) where information obtained by assimilation was lost quickly through the action of internal Kelvin waves.

The assimilation improved the mean analysed thermal state which in turn resulted in an improvement in the intensity of the NECC. However, the assimilation did not result in a global improvement of the current field. In 4D-Var, as in the control, the EUC was underestimated by $0.4\text{ms}^{-1}$. The EUC was better reproduced in 3D-Var and OI but, in those experiments, the surface currents exhibited a large eastward bias in the eastern Pacific, as well as spurious downwelling.

Not only was the mean thermal state improved by the assimilation, but also the variability, with the 3D- and 4D-Var analyses showing a larger, more realistic interannual variability in heat content and sea level than the control analyses. The fit of the 4D-Var analyses to the assimilated thermal data was also very close at time-scales of the same order or shorter than the width of the assimilation window. The 4D-Var (nonlinear) analysis trajectory closely followed changes in the thermal state associated with TIWs (30-40 day time-scale) and internal gravity waves (IGWs) (5-7 day time-scale). The 3D-Var static (linear) analysis also captured variability associated with TIWs. The 3D-Var (nonlinear) analysis trajectory, however, did not reproduce this variability because of the temporal filtering properties of the procedure used to merge the analysis increment into the model. The variability of the surface currents was also investigated. The current-field variability in 4D-Var was better than the control in the central Pacific and as good in other regions. The salinity field displayed a strong drift toward fresher values during the whole 1993-98 period in the 3D-Var analyses, and at the end of the experiment in the 4D-Var analyses.

## 6.2 Discussion

In this paper, we have assessed the potential of incremental 3D- and 4D-Var in generating ocean analyses by comparing them to more classical methods; e.g., a run without assimilation and OI. The strong points and limitations of the assimilation systems are discussed below.

4D-Var, which has a 30-day window in our experiments, is able to fit the data at equivalent or shorter time-scales: IGWs with periods near 5 days and TIWs with periods near 30 days are both well represented. While fitting observations at the time-scale of IGWs is not necessarily a good feature, as will be discussed later, this is nonetheless an impressive illustration of the ability of 4D-Var to fit data over an entire 30-day window. The 3D-Var analysis trajectory does not achieve such a close fit, mainly due to the gradual way in which the analysis increment is fed into the model, which was done out of necessity to avoid spurious adjustment. The overall effect is that 4D-Var fits the data within the specified standard error whereas 3D-Var does not. In this respect, the introduction of dynamical constraints is very positive.

As recently pointed out by Fisher and Andersson (2001), it is not obvious if the better performance of 4D-Var over 3D-Var can be attributed exclusively to the implicit flow-dependency of the background-error covariances in 4D-Var. The close fit to the data obtained in 4D-Var can partly be explained by Fig. 10 which suggests that, in all regions, the TL dynamics acts to decrease the weight given to the background state near the thermocline where the error variance is increased. However, this close fit is possibly also the result of another desirable property of 4D-Var. Referring to the expression for the analysis increment in (12), we note that the model dynamics can influence the 4D-Var analysis in two separate ways. First, through the adjoint model in $\mathbf{G}^T$ which is used to propagate the weighted innovation $\mathbf{R}^{-1}\mathbf{d}$ back to the analysis time at $t_0$, and second, in the weighting factor $\mathbf{P}^a = \left(\mathbf{B}^{-1} + \mathbf{G}^T \mathbf{R}^{-1} \mathbf{G}\right)^{-1}$ which corresponds to the analysis-error covariance matrix. In 4D-Var, the action of the TL and adjoint models is to introduce a flow dependency in the term $\mathbf{G}^T \mathbf{R}^{-1} \mathbf{G}$ of $\mathbf{P}^a$. Fisher and Andersson (2001) present a simple example in which 4D-Var produces superior results to 3D-Var even when the background-, analysis- and forecast-error covariance matrices are all stationary. This superiority is attributed to the interpolation properties of the adjoint model which is used to propagate the weighted innovations as mentioned above. They provide further experimental evidence from the ECMWF meteorological 4D-Var system to suggest that covariance evolution is not the dominating effect. In our study, the ability of 4D-Var to propagate information in time is demonstrated by the close fit to phenomena at the 5-day time-scale (IGWs) over a 30-day window, which might suggest that it is also an important feature here. To what extent these effects are responsible for the main differences observed between our ocean 3D- and 4D-Var experiments is a matter for further research.

Whereas the assimilation methods improve the fit to the assimilated data, they can have a negative effect on the other fields. This is particularly true for 3D-Var (and OI) which display spurious mean eastward currents at the surface, downwelling in the eastern Pacific, and a salinity drift towards lower values. These problems can be traced back to the absence of multivariate balance constraints, for example, in the background-error covariance matrix (**B**). Since only the thermal field is corrected in 3D-Var and OI, and not salinity and currents, this can lead to adjustment problems. These problems are reduced in 4D-Var. Despite a univariate **B**, the dynamical constraint in 4D-Var results in salinity and current-field corrections that are partially in balance with the thermal increments, leading to better surface currents and reduced salinity drift. However, there are still some areas where 4D-Var is not as good as the control. In particular, the EUC is underestimated in 4D-Var and the salinity content displays some unrealistic variations. This probably illustrates that, in 4D-Var, dynamical constraints alone are not sufficient to transfer information across model variables. A multivariate **B** could improve the analysis of the unobserved variables. In 3D-Var, this could alleviate problems associated with the surfacing of the EUC in the eastern Pacific and salinity drift (Burgers *et al.* 2002; Troccoli *et al.* 2002)

It has been shown that overfitting might be a problem in our 3D- and 4D-Var experiments. Overfitting can result in unrealistic oscillations being generated between observation points (e.g., see Daley 1991) and this feature typically appears between TAO moorings at about 5-8°N in both assimilation experiments. The 4D-

Var analyses reproduce, at the observation points, the variability in the thermal field associated with IGWs. However, the TAO array is not dense enough to resolve these waves properly so it may be wiser to filter them out altogether. For example, this could be done by treating them as representativeness error and modifying the observation-error covariance matrix (**R**) accordingly. Furthermore, a better representation of **R** would allow more information to be extracted from the background-minus-observation and analysis-minus-observation residuals for ultimately improving the estimate of **B** (Hollingsworth and Lönnberg 1989; Daley 1992). A precise tuning of **B** and **R** is essential to avoid overfitting. The introduction of additional (weak) constraints in the assimilation method could also help to reduce the amount of "noise" in the analysis. Possibilities include the use of a normal mode initialization scheme to restrict the analysis to the slow manifold of the system (Moore 1990), or the inclusion of an additional term in the cost function to penalise short time-scales (Polavarapu *et al.* 2000).

The assimilation window that has been used in the 4D-Var experiments in the present study is 30 days. In principle, we would like to use a longer assimilation window to allow greater dynamical propagation of information (e.g., it takes a first baroclinic mode Kelvin wave two months to cross the Pacific Ocean basin). However, the length of the assimilation window is limited by the validity of the TL model, and by the hypotheses that the model and forcing are perfect. We have seen that the TL approximation was accurate at the large scales, but somewhat limited in the small scales because of nonlinear processes associated with TIWs, convection and vertical mixing. However, there is scope for improving the physics in the TL model. The assumption that the model and the forcing are perfect is obviously not true, as illustrated by the bias that develops in the model when data assimilation is "turned-off". Diagnostics on the analysis increments and analysis-minus-observation residuals suggest, however, that model and forcing error are not a major problem with a 30-day assimilation window.

The background- and observation-error covariance matrices used in this study were derived somewhat heuristically, with computational efficiency and simplicity being an important consideration. The structures are reasonable for a first estimate but the statistical parameters have not been tuned objectively. We are currently in the process of developing a more comprehensive background-error covariance matrix, including, for example, multivariate constraints between temperature and salinity, and between density and currents. The correlation model is also being extended to include non-Gaussian functions and flow-dependent coordinate surfaces (Weaver and Courtier 2001). Furthermore, we are currently using TAO data to develop an improved estimate of the observation-error covariance matrix which, in particular, accounts for IGWs as a source of representativeness error. The importance of model and forcing error should also be assessed. For example, in an equatorial oceanographic context, where large spatial scales are deterministically related to the wind forcing, it might be desirable to control forcing or model error as well as initial conditions. Some preliminary studies on these two aspects are currently being undertaken with the present system.

The present 3D- and 4D-Var systems have been applied to the tropical Pacific basin. Global versions for a free-surface version of OPA are being developed. This version will include some important new parametrisations to the physics such as isopycnal and eddy-induced diffusion. The use of improved physics might extend the period for which improvements brought by assimilation, such as a tightening of the thermocline, are retained. Sources of information other than *in situ* temperature data are available (salinity, current meter data, altimetry,...). As a first step towards assimilating more observation types, we will be introducing sea-level data from altimetry in the global systems. Finally, one of the ultimate goals behind the development of the assimilation systems is to provide improved ocean analyses for seasonal forecasting. The quality of the present analyses will thus have to be assessed in terms of forecast skill using a coupled ocean-atmosphere model.

## Acknowledgements

## Appendix A: Inner-outer loop configuration

We define a sequence, $k = 1, ..., K$, of quadratic minimization problems where $K$ is the total number of state-trajectory updates (or outer) iterations to be performed. The sequence of minimization or inner iterations is denoted by $m = 1, ..., M_k$ where $M_k$ defines the total number of inner iterations performed on the $k$-th outer iteration.

Let $\mathbf{w}^k = \mathbf{w}^k(t_0)$ denote the initial state vector on the $k$-th outer loop. The increment $\delta \mathbf{w}^k = \delta \mathbf{w}^k(t_0)$ on the $k$-th outer loop is defined here as the difference between $\mathbf{w}^k$ and the background: i.e., define $\mathbf{w}^k = \mathbf{w}^b + \delta \mathbf{w}^k$ where $\mathbf{w}^0 = \mathbf{w}^b$ and $\delta \mathbf{w}^0 = 0$. The state $\mathbf{w}^k(t_i)$ is evolved according to the nonlinear model (2). A first-order expansion of (2) about the previous estimate, $\mathbf{w}^{k-1}(t_{i-1})$, gives

$$\mathbf{w}^k(t_i) \approx M(t_i, t_{i-1})(\mathbf{w}^{k-1}(t_{i-1})) + \mathbf{M}^{k-1}(t_i, t_{i-1})[\mathbf{w}^k(t_{i-1}) - \mathbf{w}^{k-1}(t_{i-1})], \tag{36}$$

which can be written as a function of $\delta \mathbf{w}^k(t_{i-1})$ by adding and subtracting a factor $\mathbf{M}^{k-1}(t_i, t_{i-1})(\mathbf{w}^b(t_{i-1}))$ on the right hand side of (36):

$$\mathbf{w}^k(t_i) \approx M(t_i, t_{i-1})(\mathbf{w}^{k-1}(t_{i-1})) - \mathbf{M}^{k-1}(t_i, t_{i-1})\delta \mathbf{w}^{k-1}(t_{i-1}) + \mathbf{M}^{k-1}(t_i, t_{i-1})\delta \mathbf{w}^k(t_{i-1}). \tag{37}$$

Note that the first two quantities on the right hand side of (37), being defined with respect to the previous outer iteration $k - 1$, are known and hence fixed on the $k$-th outer iteration. Both the known increment $\delta \mathbf{w}^{k-1}(t_i) = \mathbf{M}^{k-1}(t_i, t_{i-1})\delta \mathbf{w}^{k-1}(t_{i-1})$, and the unknown increment $\delta \mathbf{w}^k(t_i) = \mathbf{M}^{k-1}(t_i, t_{i-1})\delta \mathbf{w}^k(t_{i-1})$ which is to be estimated on the current outer iteration, are propagated by the linear model operator, $\mathbf{M}^{k-1}$, defined with respect to the reference state $\mathbf{w}^{k-1}(t_i)$. In a similar way, we can allow for a progressively updated linear observation operator $\mathbf{H}_i^{k-1}$. In this study, $H_i$ is a linear interpolator so is equivalent to $\mathbf{H}_i^{k-1}$.

On the $k$-th outer iteration, the preconditioned cost function (14) can be written as

$$J(\mathbf{v}^k) = \frac{1}{2}(\mathbf{v}^k)^T \mathbf{v}^k + \frac{1}{2}\left[\mathbf{G}^{k-1}\delta \mathbf{w}^k - \mathbf{d}^{k-1}\right]^T \mathbf{R}^{-1}\left[\mathbf{G}^{k-1}\delta \mathbf{w}^k - \mathbf{d}^{k-1}\right] \tag{38}$$

where

$$\delta \mathbf{w}^k = \mathbf{U}\mathbf{v}^k, \tag{39}$$

and $\mathbf{d}^{k-1} = (..., (\mathbf{d}_i^{k-1})^T, ...)^T$ with

$$\mathbf{d}_i^{k-1} = \mathbf{y}_i^o - H_i(\mathbf{w}^{k-1}(t_i)) + \mathbf{H}_i^{k-1}\delta \mathbf{w}^{k-1}(t_i). \tag{40}$$

Equation (38) has the same basic form as (14). The effective observation vector (40) now contains an additional term $\mathbf{H}_i^{k-1}\delta \mathbf{w}^{k-1}(t_i)$ which is nonzero when $k > 1$. At the beginning of each inner loop ($m = 1$), the first-guess of $\delta \mathbf{w}^k$ is taken to be the value of the increment obtained on the last inner iteration of the preceding outer loop ($k - 1$). Thus, when $m = 1$, $\delta \mathbf{w}^k$ and $\delta \mathbf{w}^{k-1}$ are identical and the extra term $\mathbf{H}_i^{k-1}\delta \mathbf{w}^{k-1}(t_i)$ in (40) simply cancels with the $i$-th element of $\mathbf{G}^{k-1}\delta \mathbf{w}^k$ in (38) (i.e., $\mathbf{G}_i^{k-1}\delta \mathbf{w}^k = \mathbf{H}_i^{k-1}\delta \mathbf{w}^k(t_i)$). These terms differ only after the first inner iteration ($m > 1$).

Rather than defining the increment to be the difference from the background state, we could have defined, following Rabier *et al.* (2000) and Lorenc *et al.* (2000), the increment to be the difference from the previous reference state as suggested by (36): i.e., define $\mathbf{w}^k = \mathbf{w}^{k-1} + \delta \widetilde{\mathbf{w}}^k$ where $\delta \widetilde{\mathbf{w}}^0 = 0$. In terms of $\delta \widetilde{\mathbf{w}}$, the cost function on the $k$-th outer iteration reads

$$J(\mathbf{v}^k) = \frac{1}{2}(\mathbf{v}^k)^T \mathbf{v}^k + \frac{1}{2}\left[\mathbf{G}^{k-1}\delta \widetilde{\mathbf{w}}^k - \widetilde{\mathbf{d}}^{k-1}\right]^T \mathbf{R}^{-1}\left[\mathbf{G}^{k-1}\delta \widetilde{\mathbf{w}}^k - \widetilde{\mathbf{d}}^{k-1}\right] \tag{41}$$

where

$$\delta \widetilde{\mathbf{w}}^k = \mathbf{U}\mathbf{v}^k - \mathbf{w}^{k-1} + \mathbf{w}^b, \tag{42}$$

and $\widetilde{\mathbf{d}}^{k-1} = (..., (\widetilde{\mathbf{d}}_i^{k-1})^T, ...)^T$ with

$$\widetilde{\mathbf{d}}_i^{k-1} = \mathbf{y}_i^o - H_i(\mathbf{w}^{k-1}(t_i)). \tag{43}$$

The two formulations are formally equivalent. The alternative definition of the increment simply leads to differences in the expressions for the effective observation vector (43) and preconditioning transformation (42). The second of the two formulations is slightly less costly, however, as it requires one less linear model integration per outer iteration when $k > 1$. The extra linear model integration is needed in the first formulation to compute the term $\mathbf{H}_i^{k-1} \delta\mathbf{w}^{k-1}(t_i)$ in (40) at the beginning of each inner loop, except the first when $\delta\mathbf{w}^0 = 0$. In the second formulation, $\delta\mathbf{w}^k$ is always equal to zero at the beginning of each inner loop so the initial residual in (40) can be computed immediately. Despite this slight computational advantage, for historical reasons, we have employed the first of the two formulations.

# Appendix B: Treatment of the velocity control variables in 4D-Var

## B.1: The independent velocity variables in a rigid-lid, volume-conserving ocean model

In a rigid-lid, volume-conserving model, the number of degrees of freedom in the horizontal velocity field $\mathbf{u} = (u, v)$ is limited by the nondivergence constraint on the vertical integral of $\mathbf{u}$. Let $(u, v) = (u_l, v_l; l = 1, ..., L)$ where $L$ denotes the number of model levels. In each level $l$, $(u_l, v_l)$ can be expressed as the sum of the vertically averaged (barotropic) velocity $(\overline{u}, \overline{v})$ and the deviation from the vertically averaged (baroclinic) velocity $(\widehat{u}_l, \widehat{v}_l)$. Since the vertically integrated velocity field is nondivergent, the barotropic velocity vector can be uniquely determined from a two-dimensional (2D) streamfunction $\psi$. Furthermore, since the vertical integral of the baroclinic components vanishes, the baroclinic velocity in one level, which for convenience is taken to be the surface level ($l = 1$), can be determined from those in the remaining $L - 1$ levels ($l = 2, ..., L$); the independent baroclinic components are then $(\widehat{u}, \widehat{v}) = (\widehat{u}_l, \widehat{v}_l; l = 2, ..., L)$. Formally, this results in the following system of equations for computing the $2L$ components of $(u, v)$ from the $2L - 1$ components of $(\psi, \widehat{u}, \widehat{v})$;

$$(\overline{u}, \overline{v}) = \left[ \frac{1}{D} \widehat{\mathbf{k}} \times \nabla \psi \right]_h \tag{44}$$

$$(\widehat{u}_1, \widehat{v}_1) = \left( -\frac{1}{\Delta s_1} \sum_{l=2}^{L} \widehat{u}_l \Delta s_l, -\frac{1}{\Delta s_1} \sum_{l=2}^{L} \widehat{v}_l \Delta s_l \right) \tag{45}$$

$$(u_l, v_l) = (\overline{u}, \overline{v}) + (\widehat{u}_l, \widehat{v}_l); \quad l = 1, ..., L \tag{46}$$

where $\nabla$ is the 3D gradient operator, $\widehat{\mathbf{k}} = (0, 0, 1)$, $[\ ]_h$ denotes the horizontal component, $D$ is the depth of the ocean floor referenced to the surface $z = 0$, and $\Delta s_l$ is the local depth element at the $l$-th model level. The discretized version of (44)–(46) may be represented symbolically by

$$(\psi, \widehat{u}, \widehat{v}) \xrightarrow{\mathbf{S_u}^{-I}} (u, v) \tag{47}$$

where $\mathbf{S_u}^{-I}$ is a rectangular matrix-operator, the superscript $-I$ denoting generalized *right* inverse. (The reason for introducing the generalized inverse will become clear shortly.)

Now, let $\mathbf{S_u}$ denote a generalized *left*-inverse operator that maps $(u, v)$ into $(\psi, \widehat{u}, \widehat{v})$;

$$(u, v) \xrightarrow{\mathbf{S_u}} (\psi, \widehat{u}, \widehat{v}) \tag{48}$$

$\mathbf{S_u}$ may be interpreted as a *simplification* operator (Ide *et al.* 1997) since it acts to reduce the number of degrees of freedom in the state vector, in this case by transforming to a subspace in which the vertically integrated velocities are nondivergent. The baroclinic components can be obtained immediately from (46), while the streamfunction can be computed by taking the curl of (44) and solving the resulting 2D elliptic equation (Bryan 1969):

$$\left[ \nabla \times \left( \frac{1}{D} \widehat{\mathbf{k}} \times \nabla \psi \right) \right]_z = [\nabla \times (\overline{u}, \overline{v}, 0)]_z \tag{49}$$

$$(\widehat{u}_l, \widehat{v}_l) = (u_l, v_l) - (\overline{u}, \overline{v}); \quad l = 2, ..., L \tag{50}$$

where $[\nabla \times]_z$ denotes the vertical component of the 3D curl operator.

By construction, $\mathbf{S_u}$ and $\mathbf{S_u}^{-I}$ verify the following properties (Strang 1986);

$$\mathbf{S_u} \mathbf{S_u}^{-I} = \mathbf{I_u} \tag{51}$$

$$\mathbf{S_u}^{-I} \mathbf{S_u} = \mathbf{\Pi_u} \quad \text{with} \quad \mathbf{\Pi_u}^2 = \mathbf{\Pi_u}, \tag{52}$$

where $\mathbf{I_u}$ is the identity matrix on the space of vectors $(\psi, \widehat{u}, \widehat{v})$, and $\mathbf{\Pi_u}$ is a projection matrix on the space of vectors $(u, v)$. The general expression for $\mathbf{S_u}$ satisfying both (51) and (52) is

$$\mathbf{S_u} = \left( \mathbf{S_u}^{-I^T} \mathbf{W_u} \mathbf{S_u}^{-I} \right)^{-1} \mathbf{S_u}^{-I^T} \mathbf{W_u} \tag{53}$$

where $\mathbf{W_u}$ is an appropriate metric on $(u, v)$-space. Taking $\mathbf{W_u}$ to be a diagonal matrix of volume elements at $(u, v)$-points and using the expression for $\mathbf{S_u}^{-I}$ in (44)–(46), it is straightforward to verify that $\mathbf{S_u}$ defined by (49)–(50) is consistent with the properties (52) and (53). The explicit expression for the projection operator in (52) is

$$(u, v) \overset{\mathbf{\Pi_u}}{\longmapsto} (u, v) - \left( (\overline{u}, \overline{v}) - \left[ \frac{1}{D} \widehat{\mathbf{k}} \times \nabla \psi \right]_h \right), \tag{54}$$

with $\psi$ being computed from the elliptic equation (49). The action of the operator (54) is first to compute the divergent part of the vertically integrated flow (the term between large parentheses) and then to remove it from the total velocity field in each level.

## B.2: Role of the velocity projection operator

The operators $\mathbf{S_u}$ and $\mathbf{S_u}^{-I}$ are embedded within the model operator that acts each time step on the state vector $\mathbf{w}$. At the beginning of each time step, the right inverse $\mathbf{S_u}^{-I}$ maps $(\widehat{u}, \widehat{v}, \psi)$ into $(u, v)$ which is the *physical* field on which the sequence of model operations is performed. The final operation on each time step then consists of computing the nondivergent part of the vertical integral of $(u, v)$ by mapping $(u, v)$ back into $(\widehat{u}, \widehat{v}, \psi)$ with the left inverse $\mathbf{S_u}$. On repeated time steps, this is equivalent to applying the projection operator at the end of each time step. This allows us to express the ocean model (2) more conveniently in terms of the physical state vector $\mathbf{x} = (u, v, \theta, S)^T$ since

$$\mathbf{x}(t_i) = \mathbf{\Pi} M_{(\mathbf{x})}(t_i, t_{i-1})(\mathbf{x}(t_{i-1})) \tag{55}$$

where $M_{(\mathbf{x})}$ denotes the model operator acting on $\mathbf{x} = \mathbf{S}^{-I} \mathbf{w}$, which is related to the model operator acting on the independent state vector $\mathbf{w} = (\psi, \widehat{u}, \widehat{v}, \theta, S)^T$ by $M = \mathbf{S} M_{(\mathbf{x})} \mathbf{S}^{-I}$. The upper diagonal of the block-diagonal operators $\mathbf{\Pi}$, $\mathbf{S}$ and $\mathbf{S}^{-I}$ contains $\mathbf{\Pi_u}$, $\mathbf{S_u}$ and $\mathbf{S_u}^{-I}$ respectively, while the lower diagonal is the identity matrix. Similarly, the TL model (4) can be expressed as

$$\delta \mathbf{x}(t_i) = \mathbf{\Pi} \mathbf{M}_{(\mathbf{x})}(t_i, t_{i-1}) \delta \mathbf{x}(t_{i-1}) \tag{56}$$

where $\mathbf{M} = \mathbf{S} \mathbf{M}_{(\mathbf{x})} \mathbf{S}^{-I}$ and $\delta \mathbf{x} = \mathbf{S}^{-I} \delta \mathbf{w}$.

Using the projection operator, the preconditioned form of the minimization problem (14)–(15) can be recast entirely in terms of the more practical variables $\delta \mathbf{x}$. Introducing the operators $\mathbf{G}_{(\mathbf{x})} = \mathbf{H}_{i(\mathbf{x})} \widetilde{\mathbf{M}}_{(\mathbf{x})}(t_i, t_0)$ and $\mathbf{G}_{(\mathbf{x})} = (..., \mathbf{G}_{i(\mathbf{x})}^T, ...)^T$, where $\mathbf{H}_{i(\mathbf{x})} = \mathbf{H}_i \mathbf{S}$ and $\widetilde{\mathbf{M}}_{(\mathbf{x})}(t_i, t_0) = \mathbf{\Pi} \mathbf{M}_{(\mathbf{x})}(t_i, t_{i-1}) \cdots \mathbf{\Pi} \mathbf{M}_{(\mathbf{x})}(t_1, t_0)$, and noting from (22) that the preconditioning transformation can be written as $\mathbf{U} = \mathbf{S} \mathbf{B}_{(\mathbf{x})}^{1/2}$ where $\mathbf{B}_{(\mathbf{x})}^{1/2} = \mathbf{\Sigma} \mathbf{\Lambda} \mathbf{L}^{1/2} \mathbf{W}^{-1/2}$, then (14)–(15) become

$$J(\mathbf{v}) = \frac{1}{2} \mathbf{v}^T \mathbf{v} + \frac{1}{2} \left[ \mathbf{G}_{(\mathbf{x})} \delta \mathbf{x} - \mathbf{d} \right]^T \mathbf{R}^{-1} \left[ \mathbf{G}_{(\mathbf{x})} \delta \mathbf{x} - \mathbf{d} \right] \tag{57}$$

where

$$\delta \mathbf{x} = \mathbf{S}^{-I} \mathbf{U} \mathbf{v} = \mathbf{\Pi} \mathbf{B}_{(\mathbf{x})}^{1/2} \mathbf{v}. \tag{58}$$

Since $\mathbf{v} = 0$ initially, the action of $\mathbf{\Pi}$ in (58) is obviously redundant on the first iteration since $\delta \mathbf{x} = 0$ is a trivial member of the allowed subspace of vertically-integrated nondivergent velocities. The action of $\mathbf{\Pi}^T$ in the adjoint counterpart of (58), however, must be retained to ensure that the gradient is projected onto the dual

of the allowed subspace (Eq. (17)). Since the gradient descent routine adjusts $\mathbf{v}$ as a linear combination of its first-guess and the gradient, the new estimate will also be in the allowed subspace, so that the action of $\mathbf{\Pi}$ in (58) will actually be redundant on *all* iterations providing the gradient is always projected using $\mathbf{\Pi}^T$.

Thacker and Raghunath (1994) argue that choosing $(u, v)$ as control variables, and restricting the minimization to the allowed subspace as discussed above, results in a much better conditioned minimization problem than one in which $(\psi, \widehat{u}, \widehat{v})$ are optimized directly. In their examples, however, there was no background term and a projection operator was designed explicitly for the gradient of the observation term. In our system, the projection operator appears naturally as a result of the preconditioning transformation (58) and by using the simplification operator $\mathbf{S}$ to formulate the background-error covariances of $(\psi, \widehat{u}, \widehat{v})$ indirectly in terms of those for $(u, v)$ (i.e., $\mathbf{B} = \mathbf{S}\,\mathbf{B}_{(\mathbf{x})}\mathbf{S}^T$).

## B.3: The elliptic solver in the tangent-linear and adjoint models

In OPA, the elliptic equation in (49) is solved iteratively using a preconditioned conjugate gradient method (PCG). Each iteration of PCG involves the computation of scalar products of variables that depend on the state vector. These computations render the numerical algorithm *nonlinear* even though the underlying elliptic equation is *linear*. A brute-force derivation of the TL and adjoint of the PCG solver would be both complicated and undesirable.

Two alternative procedures have been tested here. The first is to apply a *linear* elliptic solver, successive over-relaxation (SOR), in the TL and adjoint, while retaining the more efficient PCG solver in the nonlinear model. The *exact* adjoint of SOR is straightforward to derive and no extra memory (from nonlinear terms) is required. The second procedure is to apply the PCG in the TL model and to exploit the self-adjointness property of $\mathbf{\Pi_u}$, the operator in which PCG is employed, to deduce the adjoint. The self-adjointness property follows from (52) and (53);

$$\mathbf{\Pi_u}^T = \mathbf{W_u}\,\mathbf{\Pi_u}\,\mathbf{W_u}^{-1}. \tag{59}$$

Therefore, defining $\mathbf{\Pi_u}^T$ in the adjoint model to be the right hand side of (59) allows us to employ the same projection operator $(\mathbf{\Pi_u})$ in the adjoint model as in the nonlinear and TL models. In practice, the adjoint will only be *approximate* because of the iterative nature of the algorithm. The adjoint can be made as accurate as desired by adjusting the convergence threshold of the solver. In the 4D-Var experiments described in this paper, a convergence threshold was chosen such that the adjoint had a relative error of $\varepsilon = |1 - \delta\mathbf{u}^T\,\mathbf{\Pi_u}^T\,\mathbf{W_u}\,\delta\mathbf{u}\,/\,(\mathbf{\Pi_u}\delta\mathbf{u})^T\,\mathbf{W_u}\,\delta\mathbf{u}| \approx 10^{-5}$ for arbitrary horizontal velocity perturbations $\delta\mathbf{u}$. Requiring higher accuracy resulted in negligible differences in our experiments.

Of the two adjoint solvers, the second was preferred because of its better efficiency and vectorization properties. In general, the 4D-Var experiments on the Fujitsu VPP700 required 40% less CPU time with PCG than with SOR.

# References

Alves, J. O., Anderson, D. L. T., Stockdale, T. N., Balmaseda, M. A. and Segschneider, J., 1998: Sensitivity of ENSO forecasts to ocean initial conditions. *Proceedings of the Triangle'98 Symposium*, Sept. 1998, Kyoto, Japan.

Balmaseda, M., Anderson, D. L. T. and Davey, M., 1994: ENSO prediction using a dynamical ocean model coupled to statistical atmospheres. *Tellus*, **46A**, 497–511.

Barnett, T. P., Latif, M., Graham, N., Flugel, M., Pazan, S. and White, W., 1993: ENSO and ENSO-related predictability. I. Prediction of equatorial Pacific sea surface temperature with a hybrid coupled ocean-atmosphere model *J. Climate*, **6**, 1545–1566.

Baturin, N. G. and P. P. Niiler, 1997: Effect of instability waves in the mixed layer of the equatorial Pacific, *J. Geophys. Res.* **102**, 27,771–27,793.

Behringer, D., Ji, M. and Leetma, A., 1998: An improved coupled model for ENSO prediction and implications for ocean initialization. Part I: The ocean data assimilation system. *Mon. Wea. Rev.*, **126**, 1013–1021.

Bell, M. J., Martin, M. J. and Nichols, N. K., 2001: *Assimilation of data into an ocean model with systematic errors near the equator.* Ocean Applications Tech. Note No. 27, Hadley Centre for Climate Prediction and Research, Met. Office, Bracknell, UK, 27 pp.

Bennett, A. F., Chua, B. S., Harrison, D. E. and McPhaden, M. J., 2000: Generalized inversion of Tropical Atmosphere-Ocean (TAO) data using a coupled model of the tropical Pacific. *J. Climate*, **13**, 2770–2785.

Blanke, B. and Delecluse, P., 1993: Variability of the tropical Atlantic Ocean simulated by a general circulation model with two different mixed-layer physics. *J. Phys. Oceanogr.*, **23**, 1363–1388.

Bloom, S. C., Takacs, L. L., Da Silva, A. M. and Ledvina, D., 1996: Data assimilation using incremental analysis updates. *Mon. Wea. Rev.*, **124**, 1256–1271.

Bonekamp, H., van Oldenborgh, G. J. and Burgers, G., 2001: Variational assimilation of TAO and XBT data in the HOPE OGCM, adjusting the surface fluxes in the tropical ocean. *J. Geophys. Res.*, **106**, 16,693–16,709.

Bryan, K., 1969: A numerical method for the study of the circulation of the world ocean. *J. Comp. Phys.*, **4**, 347–376.

Bryden, H. L., 1973: New polynomials for thermal expansion, adiabatic temperature gradient and potential temperature gradient of sea water. *Deep-Sea Res.*, **20**, 401–408.

Burgers, G., Balmaseda, M. A., Vossepoel, F. C., van Oldenborgh, G. J. and van Leeuwen, P. J., 2002: Balanced ocean-data assimilation near the equator. *J. Phys. Oceanogr.*, in press.

Cane, M. A., Zebiak, S. E. and Dolan, S. C., 1986: Experimental forecasts of *El Niño. Nature*, **321**, 827–832.

Cooper, M. and Haines, K., 1996: Altimetric assimilation with water property conservation. *J. Geophys. Res.*, **101**, 1059–1077.

Courtier, P., Thépaut, J.-N. and Hollingsworth, A., 1994: A strategy for operational implementation of 4D-Var, using an incremental approach. *Q. J. R. Meteorol. Soc.*, **120**, 1367–1388.

Courtier, P., 1997: Dual formulation of four dimensional variational assimilation. *Q. J. R. Meteorol. Soc.*, **123**, 2449–2462.

Courtier, P., Andersson, E., Heckley, W., Pailleux, J., Vasiljević, D, Hamrud, M., Hollingsworth, A., Rabier, F. and Fisher, M., 1998: The ECMWF implementation of three dimensional variational assimilation (3D-Var). Part I: Formulation. *Q. J. R. Meteorol. Soc.*, **124**, 1783–1808.

Daley, R., 1991: *Atmospheric data analysis*. Cambridge atmospheric and space sciences series, Cambridge University Press, 457 pp.

Daley, R., 1992: Estimating model-error covariances for application to atmospheric data assimilation. *Mon. Wea. Rev.*, **120**, 1735–1746.

Derber, J. C. and Rosati, A., 1989: A global oceanic data assimilation system. *J. Phys. Oceanogr.*, **19**, 1333–1347.

Derber, J. C. and Bouttier, F., 1999: A reformulation of the background error covariance in the ECMWF global data assimilation system. *Tellus*, **51A**, 195–221.

Desroziers, G. and Ivanov, S., 2001: Diagnosis and adaptive tuning of observation error parameters in a variational assimilation. *Q. J. R. Meteorol. Soc.*, **127**, 1433–1452.

Egbert, G. D., Bennett, A. F. and Foreman, M. G. G., 1994: Topex/Poseidon tides estimated using a global inverse model. *J. Geophys. Res.*, **99**, 24,821–24,852.

Fisher, M. and Andersson, E., 2001: Developments in 4D-Var and Kalman Filtering, ECMWF Tech. Memo. No. 347.

Gauthier, P., Charette, C., Fillion, L., Koclas, P. and Laroche, S., 1999: Implementation of a 3D variational data assimilation system at the Canadian Meteorological Centre. Part I: the global analysis. *Atmosphere-Ocean*, **37**, 103–156.

Gibson, J., Hernandez, A., Kåallberg, P., Nomura, A., Serrano, E. and Uppala, S., 1996: The ECMWF Re-Analysis Project (ERA) - Plans and current status. In *Preprints - Tenth Conference on Numerical Weather Prediction, Portland, Or.*, pp. 288–291, Amer. Meteor. Soc.

Giering, R. and Kaminski, T., 1998: Recipes for adjoint code construction. *ACM TOMS*, **24**, 437–474.

Gill, A. E., 1982: *Atmosphere-Ocean Dynamics*. Academic Press, London, 662 pp.

Gilbert, J.-C. and Lemaréchal, C., 1989: Some numerical experiments with variable-storage quasi-Newton algorithms. *Math. Programming*, **45**, 407–435.

Greiner, E., Arnault, S. and Morlière, A., 1998: Twelve monthly experiments of 4D-variational assimilation in the tropical Atlantic during 1987: Part I: Method and statistical results. *Prog. Oceanogr.*, **41**, 141—202.

Greiner, E., Arnault, S. and Morlière, A., 1998: Twelve monthly experiments of 4D-variational assimilation in the tropical Atlantic during 1987: Part II: Oceanographic interpretation. *Prog. Oceanogr.*, **41**, 203—247.

Greiner, E. and Arnault, S., 2000: Comparing the results of a 4D-variational assimilation of satellite and in situ data with WOCE CITHER hydrographic measurements in the tropical Atlantic. *Prog. Oceanogr.*, **47**, 1–68.

Grima, N., Bentamy, A., Katsaros, K., Quilfen, Y., Delecluse, P. and Lévy, C., 1999: Sensitivity study of an oceanic general circulation model forced by satellite wind-stress fields. *J. Geophys. Res.*, **104**, 7967–7989.

Hollingsworth, A. and Lönnberg, P., 1989: The verification of objective analyses: diagnostics of analysis system performance. *Meteorol. Atmos.*, **40**, 3–27.

Ide, K., Courtier, P., Ghil, M. and Lorenc, A. C., 1997: Unified notation for data assimilation: operational, sequential and variational. *J. Met. Soc. Japan*, **75**, 181–189.

Jackett, D. R. and McDougall, T. J., 1995: Minimal adjustment of hydrographic data to acheive static stability. *J. Atmos. Ocean. Tech.*, **12**, 381–389.

Janiskova, M., Thépaut, J.-N. and Geleyn, J.-F., 1999: Simplified and regular physical parametrizations for incremental four-dimensional variational assimilation. *Mon. Wea. Rev.*, **51A**, 147–166.

Ji, M. and Leetma, A., 1997: Impact of data assimilation on ocean initialization and *El Nño* prediction. *Mon. Wea. Rev.*, **125**, 742–753.

Kessler, W. S., Spillane, M. C., McPhaden, M. J. and Harrison, D. E., 1996: Scales of variability in the equatorial Pacific inferred from the Tropical Atmosphere-Ocean buoy array. *J. Climate*, **9**, 2999–3024.

Laroche, S. and Gauthier, P., 1998: A validation of the incremental formulation of 4D variational data assimilation in a nonlinear barotropic flow. *Tellus*, **50A**, 557–572.

Latif, M. and Flügel, M., 1991: An investigation of short-range climate predictability in the tropical Pacific. *J. Geophys. Res.*, **96**, 2661–2673.

Le Dimet, F. X. and Talagrand, O., 1986: Variational algorithms for analysis and assimilation of meteorological observations: Theoretical aspects. *Tellus*, **38A**, 97–110.

Lee, T. and Marotzke, J., 1997: Inferring meridional mass and heat transports of the Indian Ocean by fitting a general circulation model to climatological data. *J. Geophys. Res.*, **99**, 10,585–10,602.

Lee, T. and Marotzke, J., 1998: Seasonal cycles of meridional overturning and heat transport of the Indian Ocean. *J. Phys. Oceanogr.*, **28**, 923–943.

Legeckis, R., 1977: Long waves in the eastern equatorial Pacific; a view from a geostationary satellite. *Science*, **197**, 1177–1181.

Levitus, S., 1982: *Climatological Atlas of the World Ocean.* NOAA Prof. Paper No. 13, U. S. Govt. Printing Office, 173 pp.

Lewis, J. M. and Derber, J. C., 1985: The use of adjoint equations to solve a variational adjustment problem with advective constraints. *Tellus*, **37**, 309–322.

Lorenc, A. C., 1981: A global three-dimensional multivariate statistical interpolation scheme. *Mon. Wea. Rev.*, **109**, 701–721.

Lorenc, A. C., 1986: Analysis methods for numerical weather prediction. *Q. J. R. Meteorol. Soc.*, **112**, 1177–1194.

Lorenc, A. C., Ballard, S. P., Bell, R. S., Ingleby, N. B., Andrews, P. L. F., Barker, D. M., Bray, J. R., Clayton, A. M., Dalby, T., Li, D., Payne, T. J. and Saunders, F. W., 2000: The Met. Office global three-dimensional variational data assimilation scheme. *Q. J. R. Meteorol. Soc.*, **126**, 2991–3012.

Madec, G., Delecluse, P., Imbard, M. and Lévy, C., 1998: OPA 8.1 Ocean General Circulation Model Reference Manual. Technical note no. 11, LODYC/IPSL, Paris, France.

Mahfouf, J.-F., 1999: Influence of physical processes on the tangent-linear approximation. *Tellus*, **51A**, 147–166.

Marotzke, J. and Wunsch, C., 1993: Finding a steady state of a general circulation model through data assimilation: Application to the North Atlantic Ocean. *J. Geophys. Res.*, **98**, 20,149–20,167.

McCarty, M. E., Mangum, L. J. and McPhaden, M. J., 1997: Temperature errors in TAO data induced by mooring motion. NOAA Tech. Memo. ERL PMEL-108, 14 pp.

McCreary, J. P., 1981: A linear stratified ocean model of the Equatorial Undercurrent. *Phil. Trans. Roy. Soc. Lond.*, **298A**, 603–635.

McPhaden, M. J., 1993: TOGA-TAO and the 1991-93 *El Niño*-Southern Oscillation event. *Oceanography*, **6**, 36–44.

Ménard, R. and Daley, R., 1996: The application of Kalman smoother theory to the estimation of 4DVAR error statistics. *Tellus*, **48A**, 221–237.

Meyers, G., Phillips, H., Smith, N. and Sprintall, J., 1991: Space and time scales for optimal interpolation of temperature- tropical Pacific Ocean. *Prog. Oceanogr.*, **28**, 189–218.

Moore, A. M. and Anderson, D. L. T., 1989: The assimilation of XBT data into a layer model of the tropical Pacific Ocean. *Dyn. Atmos. Oceans*, **13**, 441–464.

Moore, A. M., 1990: Linear equatorial wave mode initialization in a model of the tropical Pacific Ocean: an initialization scheme for tropical ocean models. *J. Phys. Oceanogr.*, **20**, 423–445.

Palmer, T. N. and Anderson, D. L. T., 1994: Prospects for seasonal forecasting. *Q. J. R. Meteorol. Soc.*, **120**, 755–794.

Parrish, D. F. and Derber, J. C., 1992: The National Meteorological Center's spectral statistical interpolation analysis system. *Mon. Wea. Rev.*, **120**, 1747–1763.

Philander, S. G, 1989: *El Niño, La Niña, and the Southern Oscillation.* Academic Press, Harcourt Brace Jovanovich Publishers. 293 pp.

Polavarapu, S., Tanguay, M. and Fillion, L., 2000: Four-dimensional variational data assimilation with digital filter initialization. *Mon. Wea. Rev.*, **128**, 2491–2510.

Rabier, F., McNally, A., Andersson, E., Courtier, P., Undén, P., Eyre, J., Hollingsworth, A. and Bouttier, F., 1998: The ECMWF implementation of three dimensional variational assimilation (3D-Var). Part II: Structure functions. *Q. J. R. Meteorol. Soc.*, **124**, 1809–1829.

Rabier, F., Järvinen, H., Klinker, E., Mahfouf, J.-F. and Simmons, A., 2000: The ECMWF operational implementation of four dimensional variational assimilation. Part I: Experimental results with simplified physics. *Q. J. R. Meteorol. Soc.*, **126**, 1143–1170.

Reverdin, G., Frankignoul, E., Kestenare, E. and McPhaden, M. J., 1994: Seasonal variability in the surface currents of the equatorial Pacific *J. Geophys. Res.*, **99**, 20323–20344.

Reynolds, R. W. and Smith, T. M., 1994: Improved global sea surface temperature analyses using optimal interpolation. *J. Climate*, **7**, 929–948.

Rosati, A., Miyakoda, K. and Gudgel, R., 1997: The impact of ocean initial conditions on ENSO forecasting with a coupled model. *Mon. Wea. Rev.*, **125**, 754–772.

Roullet, G. and Madec, G., 2000: Salt conservation, free surface, and varying levels: a new formulation for ocean general circulation models. *J. Geophys. Res.*, **105**, 23927–23942.

Segschneider, J., Anderson, D. L. T. and Stockdale, T. N., 2000: Towards the use of altimetry for operational seasonal forecasting. *J. Climate*, **13**, 3116–3138.

Segschneider, J., Balmaseda, M. and Anderson, D. L. T., 2000: Anomalous hydrographic variations in the tropical Atlantic: possible causes and implications for the use of altimeter data. *Geophys. Res. Let*, **27**, 2281–2284.

Segschneider, J., Anderson, D. L. T., Vialard, J., Balmaseda, M. and Stockdale, T. N., 2002: Initialization of seasonal forecasts assimilating sea level and temperature observations. *J. Climate*, **14**, 4292–4307.

Smith, N. R., Blomley, J. E. and Meyers, G., 1991: A univariate statistical interpolation scheme for subsurface thermal analyses in the tropical oceans. *Prog. Oceanogr.*, **28**, 219–256.

Strang, G., 1976: *Linear Algebra and Its Applications*, Harcourt Brace Jovanovich Publishers. 505 pp.

Talagrand, O. and Courtier, P., 1987: Variational assimilation of meteorological observations with the adjoint vorticity equation. I: Theory. *Q. J. R. Meteorol. Soc.*, **113**, 1311–1328.

Talagrand, O., 1991: The use of adjoint equations in numerical modeling of the atmospheric circulation. In *Automatic Differentiation of Algorithms: Theory, Implementation, and Application*, A. Griewank and G. F. Corliss (eds), SIAM Publishers, Philadelphia, PA. pp. 169–180.

Talagrand, O., 1999: *A posteriori* verification of analysis and assimilation algorithms. In *Proceedings of the ECMWF Workship on Diagnosis of Data Assimilation Systems*, pp. 17–28, Reading, England, 1999 2–4 November.

Tarantola, A., 1987: *Inverse Problem Theory: Methods for Data Fitting and Model Parameter Estimation.* Elsevier. 613 pp.

Thacker, W. C. and Long, R. B., 1988: Fitting dynamics to data. *J. Geophys. Res.*, **93**, 1227-1240.

Thacker, W. C. and Raghunath, R., 1994: The rigid lid's contribution to the ill-conditioning of oceanic inverse problems. *J. Geophys. Res.*, **99**, 10131-10141.

Thépaut, J.-N. and Courtier, 1991: Four-dimensional variational data assimilation using the adjoint of a multilevel primitive equation model. *Q. J. R. Meteorol. Soc.*, **117**, 1225–1254.

Thépaut, J.-N., Hoffman, R. N. and Courtier, P., 1993: Interactions of dynamics and observations in four-dimensional variational assimilation. *Mon. Wea. Rev.*, **121**, 3393–3414.

Thépaut, J.-N., Courtier, P., Belaud, G. and LeMaître, G., 1996: Dynamical structure functions in a four-dimensional variational assimilation: a case study. *Q. J. R. Meteorol. Soc.*, **122**, 535–561.

Troccoli, A., Alonso Balmaseda, M., Segschneider, J., Vialard, J., Anderson, D. L. T., Stockdale, T., Haines, K. and Fox, A. D., 2002: Salinity adjustments in the presence of temperature data assimilation. *in Mon. Wea. Rev.*, **130**, 89–102.

Tzipermann, E., Thacker, W. C., Long, R. B. and Hwang, S.-M., 1992: Oceanic data analysis using a general circulation model. Part I: Simulations. *J. Phys. Oceanogr.*, **22**, 1434–1457.

Tzipermann, E., Thacker, W. C., Long, R. B. and Hwang, S.-M., Rintoul, S. R., 1992: Oceanic data analysis using a general circulation model. Part II: A North Atlantic model. *J. Phys. Oceanogr.*, **22**, 1458–1485.

Tzipermann, E. and Sirkes, Z., 1997: Using the adjoint method with the ocean component of coupled ocean-atmosphere models. *J. Met. Soc. Japan*, **75**, 463–470.

Vialard, J., Menkes, C., Boulanger, J.-P., Delecluse, P., Guilyardi, E., McPhaden, M. J. and Madec, G., 2001: A model study of oceanic mechanisms affecting equatorial Pacific sea surface temperature during the 1997-98 El Niño. *J. Phys. Oceanogr.*, **31**, 1649–1675.

Wahba, G., Johnson, D. R., Gao, F. and Gong, J., 1995: Adaptive tuning of numerical weather prediction models: randomized GCV in three- and four-dimensional data assimilation. *Mon. Wea. Rev.*, **123**, 3358–3369.

Weaver, A. T. and Courtier, P., 2001: Correlation modelling on the sphere using a generalized diffusion equation. *Q. J. R. Meteorol. Soc.*, **127**, 1815–1846.

Xu, Q., 1996: Generalized adjoint for physical processes with parametrized discontinuities. Part I: basic issues and heuristic examples. *J. Atmos. Sci.*, **53**, 1123–1142.

Yu, L. and Malanotte-Rizzoli, P., 1998. Inverse modelling of seasonal variations in the North Atlantic Ocean. *J. Phys. Oceanogr.*, **28**, 902–922.

Zhu, J. and Kamachi, M., 2000: The role of time step size in numerical stability of tangent linear models. *Mon. Wea. Rev.*, **128**, 1562–1572.

Zou, X., 1997: Tangent-linear and adjoint of 'on-off' processes and their feasibility for use in 4-dimensional variational data assimilation. *Tellus*, **49A**, 3–31.